

**A study of heavy flavor quarks produced in association
with top quark pair events at a center-of-mass energy
of 7 TeV using the ATLAS detector**

A Dissertation

Presented to the Faculty of the Graduate School

of

Yale University

in Candidacy for the Degree of

Doctor of Philosophy

by

Richard Wall

Dissertation Director: Professor Paul Louis Tipton

May 2013

CERN-THESIS-2013-292
05/03/2013



©2013 by Richard Wall.

All rights reserved.

Acknowledgements

In general, I would like to thank the Yale ATLAS group for a wonderful six years. In particular, Jahred for helping guide me through my early analysis work and my first attempts at maximum likelihood fitting, and Andrey for his friendship, for showing me what it means to be Russian, and fir his invaluable help with my thesis project itself. Of course, my experience at Yale begins and ends with my advisor Paul, whose guidance and advice has given me a wonderful blue print for a successful and happy scientist which I hope to follow in the coming years.

For the $t\bar{t} + \text{HF}$ analysis work presented in this thesis, I would like to thank CERN, the LHC, and the whole of ATLAS. My work is built on top of the work of many thousands of others, and it has been a pleasure to work in such a collaborative environment. In particular, I would like to thank Ford Garberson, Francesco Spano, and the rest of the Top group for their careful over-sight and guidance of the analysis.

Finally, I would like to thank my family for their support throughout this process. To my parents, for their continued words of encouragement, and generally for their excitement at what I do. To my office-mate Dexter, for reminding me to talk a walk every once and awhile, and not be bothered by the unimportant things. And most importantly to my wife Hannah, the love of my life, for her patience, perspective, and generally for keeping me sane: I don't know how she managed to keep my head on (mostly) straight, but somehow she did. Without you all, I would long ago have lost the grounding which allowed to accomplish all that I have.

Abstract

A study of heavy flavor quarks produced in association with top quark pair events at a center-of-mass energy of 7 TeV using the ATLAS detector

Richard Wall

2013

In this thesis, we show evidence for the production of $t\bar{t} + b + X$ and $t\bar{t} + c + X$, together referred to as $t\bar{t} + \text{HF}$, at the Large Hadron Collider. A sample of dilepton $t\bar{t}$ candidate events with three or more b -tagged jets is used to isolate a $t\bar{t}$ sample rich in extra heavy flavor jets. A fit to the vertex mass distribution for the b -tagged jets in this region is performed to extract the flavor composition of the additional b -tags. This measurement is converted to a cross-section for $t\bar{t} + \text{HF}$ production ($\sigma_{\text{fid}}(t\bar{t} + \text{HF})$) using a correction factor from Monte Carlo simulation. The cross-section for $t\bar{t}$ events with at least one additional jet is also measured ($\sigma_{\text{fid}}(t\bar{t} + \text{j})$). The final result is quoted as a ratio of cross-sections within the visible ATLAS acceptance to reduce the overall systematic uncertainty. Using 4.7 fb^{-1} of data collected during the 2011 run, we find the ratio of $\sigma_{\text{fid}}(t\bar{t} + \text{HF})$ to $\sigma_{\text{fid}}(t\bar{t} + \text{j})$ to be 7.9 ± 1.4 (stat.) $^{+5.5}_{-2.1}$ (syst.)%, compared to the leading-order Standard Model expectation of $4.1 \pm 1.3\%$.

Contents

1	Introduction	1
2	Theory	6
2.1	The Standard Model	7
2.1.1	Historical development	7
2.1.2	Quarks and leptons	10
2.1.3	Symmetry and gauge forces	14
2.2	Phenomenology at the LHC	18
2.3	Electroweak symmetry breaking	21
2.4	Implications for future measurements	23
3	The LHC and ATLAS detector	25
3.1	CERN, and the LHC	27
3.2	The inner tracker	29
3.2.1	The Pixel Tracker	31
3.2.2	The Semiconductor Tracker	32
3.2.3	The Transition Radiation Tracker	33
3.3	The calorimeters	34
3.3.1	Liquid argon calorimeters	35
3.3.2	Tile calorimeter	36
3.4	The muon system	38
3.4.1	Monitored Drift Tube chambers	38

3.4.2	Cathode-Strip chambers	39
3.4.3	Resistive plate chambers	40
3.4.4	Thin gap chambers	41
3.5	The trigger and data acquisitions system	41
3.6	Data quality and GRL's	44
4	Monte Carlo and data samples	47
4.1	Monte Carlo Samples	47
4.2	Data samples	49
4.3	Data-driven corrections to the Monte Carlo	51
5	Object and event selection	57
5.1	Kinematic requirements	57
5.1.1	Electrons	57
5.1.2	Muons	59
5.1.3	Jets	61
5.1.4	E_T^{miss} calculation	63
5.2	$t\bar{t}$ candidate event selection cuts	63
5.3	Definition of the fiducial volume	66
6	Analysis method	69
6.1	Signal & background estimate	69
6.2	Fake lepton estimate	71
6.3	Fitting method	75

6.4	Cross-section calculation	81
7	Systematics	84
7.1	Lepton identification	85
7.2	Jet properties	86
7.3	Jet tagging efficiency	88
7.4	Missing E_T calculation	90
7.5	Top quark event generation and showering	90
7.6	RSS method	92
7.7	Fit template uncertainties	94
7.8	Fit template cross-checks	96
7.9	Acceptance calculation	98
8	Expected background and signal yields	100
8.1	Control regions with loose leptons	101
8.2	OS control regions	108
8.3	Systemtics in OS control regions	118
8.4	SS control regions	119
8.5	Signal region	129
8.6	Fit results	135
9	Results	138
9.1	Signal region fit	138
9.2	Acceptance calculation	145

9.3	Fiducial cross-sections	147
9.4	Conclusions	150
	Bibliography	152
	Appendix	159
A	Data and Monte Carlo samples	159
A.1	Data	159
A.2	Monte Carlo	160

List of Tables

1	Details of how events are classified when combining Monte Carlo samples where extra HF is generated at the matrix element level. Hard scatter HF is defined by requiring the HF partons to be well-separated ($\Delta R > 0.4$). Events in the inclusive sample without HF are designated ‘isLF.’	48
2	Expected event yields, and the final reconstruction efficiency for the two fiducial regions ($t\bar{t} + \text{HF}$ and $t\bar{t} + j$). The yields are calculated assuming 4.7 fb^{-1} of integrated luminosity. The efficiency is defined as the ratio of reconstructed, fiducial events to generated, fiducial events for the two processes: $t\bar{t} + \text{HF}$, and $t\bar{t} + j$. We require three reconstructed b -tags for $t\bar{t} + \text{HF}$ and two reconstructed b -tags for $t\bar{t} + j$. Only statistical uncertainties are included. . .	68
3	Comparison of the OS/SS ratio for events with a fake lepton coming from a light flavor jet (predominantly mis-identified hadrons). We separately examine events where the fake lepton matches to a W boson and events where the fake lepton does not match to a W	73

4	<p>OS/SS ratio for fake events using loose leptons, for three dilepton channels and tag multiplicity bins. Errors quoted are statistical. To understand potential systematic variations in R, we show R for different kinds of fakes: heavy and light flavor jets, and conversions. The nominal OS/SS ratio used is 1.32 ± 0.10 (stat.) ± 1.82 (sys.) for ee, 1.15 ± 0.07 (stat.) ± 0.68 (sys.) for $\mu\mu$, and 1.16 ± 0.03 (stat.) ± 0.54 (sys.) for $e\mu$. The systematic uncertainty is computed by comparing the nominal OS/SS ratio with that obtained using only LF fakes.</p>	74
5	<p>OS/SS ratio for fake events using tight, for three dilepton channels and tag multiplicity bins. Errors quoted are statistical. Within statistical uncertainties, there is no observed bias in the OS/SS ratio caused by the tighter selection.</p>	74
6	<p>Fit result, acceptance factor, $\sigma_{\text{fid}}(t\bar{t} + j)$, and R_{HF} compared across a number of generators. ALPGEN + HERWIG is the baseline sample used in the rest of the analysis. ALPGEN + PYTHIA and ACERMC samples are used to evaluate showering and initial / final state radiation systematics. POWHEG + HERWIG is used to quote a systematic on the event generator (ALPGEN). MC@NLO, POWHEG + PYTHIA, and ALPGEN + PYTHIA with varied k_t factors are quoted only as a reference.</p>	92

7	Event yield expected in 4.7 fb^{-1} in opposite-sign dilepton events with loose lepton selection. Uncertainties on individual components are statistical only. For the final estimate, systematics are included (listed second). To assess the validity of the RSS estimate, we compare the observed yield in data with the expected signal yield from Monte Carlo subtracted to the RSS estimate. These two numbers are in agreement, indicating the RSS method accurately predicts the background from events with fake leptons.	102
8	Event yield expected in 4.7 fb^{-1} in the oppositely-charged dilepton sample with zero b -tagged jets. Uncertainties on individual components are statistical only. For the final estimate, systematics are included (listed second).	108
9	Event yield expected in 4.7 fb^{-1} in the oppositely-charged dilepton sample with one b -tagged jet. Uncertainties on individual components are statistical only. For the final estimate, systematics are included (listed second).	108
10	Event yield expected in 4.7 fb^{-1} in the oppositely-charged dilepton sample with two b -tagged jets. Uncertainties on individual components are statistical only. For the final estimate, systematics are included (listed second).	117
11	Breakdown of systematic uncertainties in $t\bar{t}$ control regions	118
12	Event yield expected in 4.7 fb^{-1} in the same-sign dilepton sample with zero b -tagged jets. Uncertainties on individual components are statistical only. For the final estimate, systematics are included (listed second).	119
13	Event yield expected in 4.7 fb^{-1} in the same-sign dilepton sample with one b -tagged jet. Uncertainties on individual components are statistical only. For the final estimate, systematics are included (listed second).	119

14	Event yield expected in 4.7 fb^{-1} in the same-sign dilepton sample with two b -tagged jets. Uncertainties on individual components are statistical only. For the final estimate, systematics are included (listed second).	120
15	Event yield expected in 4.7 fb^{-1} in same-sign dilepton events with three or more b -tagged jets. Uncertainties on individual components are statistical only. For the final estimate, systematics are included (listed second).	129
16	Event yield expected in 4.7 fb^{-1} in opposite-sign dilepton events with three or more b -tagged jets. Uncertainties on individual components are statistical only. For the final estimate, systematics are included (listed second).	134
17	The expected fit results for the fraction of b_e and light-flavor jets. Using Monte Carlo, 500 pseudo-experiments are performed, each assuming an integrated luminosity of 4.7 fb^{-1}	135
18	Summary of fit results using 4.7 fb^{-1} of data	144
19	Summary of calculation of the fiducial cross-sections for $t\bar{t} + \text{HF}$ and $t\bar{t}$	148
20	Systematic uncertainty on the measured value of R_{HF}	149
21	Final measurement of R_{HF} , compared to Monte Carlo prediction	149
22	Details of each data-taking period from the 2011 run. The start and end dates for each period, the total integrated luminosity recorded by ATLAS during the period, and the peak number of interactions per bunch-crossing are given. The total recorded luminosity does not take into the GRL used in this analysis, so the amount of data used from each period will be slightly different.	160
23	$t\bar{t}$ MC samples used in the analysis.	161

24	$t\bar{t}$ Monte Carlo samples used to evaluate generator & showering systematics.	161
25	$t\bar{t}$ Monte Carlo samples used to evaluate ISR / FSR systematics.	162
26	W +jets MC samples used in the analysis.	162
27	Z +jets MC samples used in the analysis.	163
28	$Z+b\bar{b}$ MC samples used in the analysis.	163
29	Low mass Z +jets MC samples used in the analysis.	164
30	Single top & diboson MC samples used in the analysis.	164

List of Figures

1	Feynman diagrams depicting production of $t\bar{t}$ events with associated heavy flavor, either c -quarks or b -quarks.	2
2	Event display showing $t\bar{t}$ candidate event in the ee decay mode	26
3	The LHC accelerator complex	28
4	The ATLAS inner tracker	30
5	Relative momentum resolution for muons as a function of η in the inner tracker	31
6	Fraction of high-threshold hits in the TRT for electrons and pions	34
7	Computer graphic showing the ATLAS calorimeter systems	37
8	Graphic of the ATLAS muon systems	39
9	CSC layout	40
10	Trigger efficiency for electrons and muons	43
11	DQ efficiency for the 2011 run	46
12	Total luminosity recorded by ATLAS during the 2011 run period.	49

13	Peak average number of interactions per bunch crossing during the 2011 run.	50
14	Electron Tight++ scale factors as a function of η (integrated over $E_T > 20$ GeV) (left) and E_T -corrections (right).	52
15	Muon scale factors as a function of the number of reconstructed vertices in the event. Different isolation cuts are compared. Subsequent optimization studies showed that the best option was to require E_T (cone 20) < 2 GeV and p_T (cone 30) < 4 GeV (red squares).	53
16	The b -jet tagging efficiency estimated from data compared with the efficiency estimated from Monte Carlo simulations (left) and the resulting scaling factors (right) together with statistical and systematic uncertainties for the tagger MV1 as a function of p_T at the working point corresponding to 70% efficiency.	54
17	Hard-scatter (a) efficiency and (b) inefficiency scale factors as a function of the p_T of the jet.	56
18	Pile-up (a) efficiency and (b) inefficiency scale factors as a function of the p_T of the jet.	56
19	The rejection factors as a function of the tagging efficiency for different b -jet taggers available at ATLAS. As can be seen, the MV1 tagger shows the best rejection power for light jets and is therefore highly recommended to be used.	62
20	OS/SS ratio as a function of tag jet multiplicity	75
21	Vertex mass templates	77
22	Data / MC comparison in dilepton events with one b -tag	97
23	Vertex mass shape modeling scale factors	98
24	Acceptance factor for the measurement of $t\bar{t}$ + HF as a function of $f_{b/HF}$. .	99

25	Lepton p_T distributions in the loose $t\bar{t}$ control region	104
26	Jet p_T distributions in the loose $t\bar{t}$ control region	105
27	E_T^{miss} and H_T distributions in the loose $t\bar{t}$ control region	106
28	Lepton-lepton invariant mass and jet multiplicity distributions in the loose $t\bar{t}$ control region	107
29	Leading lepton p_T distributions in the $t\bar{t}$ control region	109
30	Sub-leading lepton p_T distributions in the $t\bar{t}$ control region	110
31	Leading jet p_T distributions in the $t\bar{t}$ control region	111
32	Sub-leading jet p_T distributions in the $t\bar{t}$ control region	112
33	E_T^{miss} distributions in the $t\bar{t}$ control region	113
34	H_T distributions in the $t\bar{t}$ control region	114
35	Lepton-lepton invariant mass distributions in the $t\bar{t}$ control region	115
36	Selected jet multiplicity distributions in the $t\bar{t}$ control region	116
37	Leading lepton p_T distributions in the same-sign $t\bar{t}$ control region	121
38	Sub-leading lepton p_T distributions in the same-sign $t\bar{t}$ control region	122
39	Leading jet p_T distributions in the same-sign $t\bar{t}$ control region	123
40	Sub-leading jet p_T distributions in the same-sign $t\bar{t}$ control region	124
41	E_T^{miss} distributions in the same-sign $t\bar{t}$ control region	125
42	H_T distributions in the same-sign $t\bar{t}$ control region	126
43	Lepton-lepton invariant mass distributions in the same-sign $t\bar{t}$ control region	127
44	Selected jet multiplicity distributions in the same-sign $t\bar{t}$ control region	128
45	Lepton p_T distributions in the signal region	130
46	Jet p_T distributions in the signal region	131

47	E_T^{miss} and H_T distributions in the signal region	132
48	Lepton-lepton invariant mass and jet multiplicity distributions in the signal region	133
49	Distribution of the expected fit values on the fitted fraction b_e and light jets in the signal region	136
50	Distribution of the expected error on the fitted fraction b_e and light jets in the signal region	137
51	Jet p_T of the four leading jets in the signal region	140
52	Vertex mass for tagged jets in the signal region	141
53	Fit template using 4.7 fb^{-1} of data	142
54	Fit templates comparing three distinct measurements of the b_e and light fraction	143
55	Variation of R_{HF} as a function of the $b:c$ ratio in the fiducial region	146

1 Introduction

The dream of modern particle physics is to understand the Universe by studying its most fundamental components. At some level, humans have been trying to accomplish this feat since ancient Greek philosophers wondered about the classical elements of earth, water, fire, air, and aether. In the past hundred years, a truly staggering amount of progress has been made, and the Universe has proven to be a far richer and more interesting place than anyone could imagine a few short decades prior. As we now understand it, all of the matter we see in the world today is composed principally of particles called the up quark, the down quark, and the electron. There are, however, a whole host of more massive particles too unstable to exist in today's Universe, and so-called anti-matter, the 'opposite' of regular matter which will eradicate regular matter on contact. These particles interact through three forces: the familiar electromagnetic force governing the interaction of charged particles, and the less macroscopically obvious strong and weak forces. Of course, we know that particles also interact via the gravitational force, but a theoretical understanding of gravity consistent with our view of the sub-atomic world has remained elusive.

According to the Standard Model (SM) of particle physics, there are six particles called quarks, which are only observable in composite particles called hadrons. Three of these quarks, the charm (c), bottom (b), and top (t), are traditionally termed 'heavy' in the sense that they have a rest mass above that of a proton. The most direct way to study these heavy quarks is to produce them directly by colliding electrons or hadrons at high energies. Roughly speaking, the kinetic energy of the collision is converted to the mass of the heavy quarks, which subsequently decay (in the case of top) or form hadrons (in the case of the

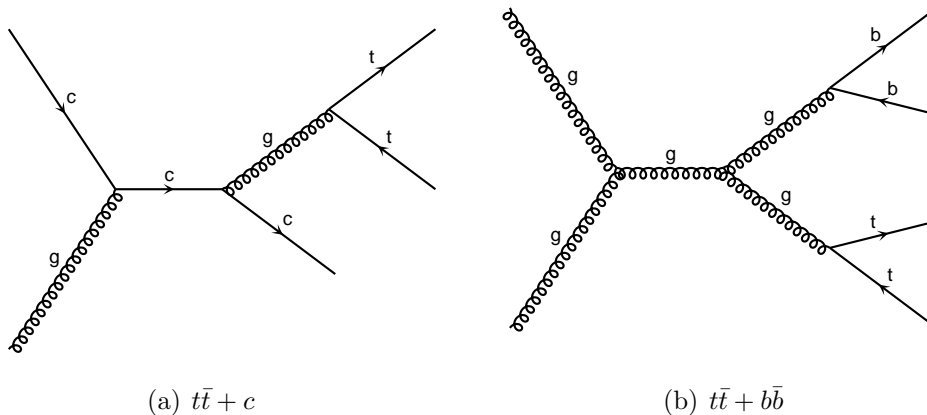


Figure 1: Feynman diagrams depicting production of $t\bar{t}$ events with associated heavy flavor, either c -quarks or b -quarks.

charm and bottom). Often, quarks are produced together with their anti-matter counterpart, denoted with a ‘bar,’ as in t for a top quark and \bar{t} for an anti-top. Owing to their large mass, we refer to b - and c -quarks together as ‘heavy flavor’ (HF). The top quark is of course heavy as well, but it is so special that it is regarded separately, and should not be assumed to fall under the HF label.

In this thesis, we present a study of the associated production of b - and c -quarks in association with top-anti-top ($t\bar{t}$) quark pairs. This study is conducted using 4.7 fb^{-1} of proton-proton (pp) collision data collected at $\sqrt{s} = 7 \text{ TeV}$ by the ATLAS detector, which operates at the Large Hadron Collider (LHC) outside Geneva, Switzerland. According to the SM, the dominant production mechanism for this process is gluon splitting to $b\bar{b}$ or $c\bar{c}$, which leads to a $t\bar{t} + b\bar{b}$ or $t\bar{t} + c\bar{c}$ final state. Any b - or c -quark content in the initial state proton can also contribute, leading to a $t\bar{t} + b$ or $t\bar{t} + c$ final state. More exotic production mechanisms (mostly the production of $t\bar{t}$ pairs with gauge bosons) are also possible, but the sum of these contributions is less than 1% of the signal expected for this analysis. Representative

diagrams (called Feynman diagrams) for the two dominant production modes (gluon splitting and initial state b or c content) can be seen in Figure 1. A next-to-leading-order calculation of the $t\bar{t} + b\bar{b}$ production cross-section at 14 TeV was done in [1], while similar calculations for $t\bar{t} + \text{jet}$ production were done in [2].

While studying the production of HF quarks in $t\bar{t}$ events may be of some interest in its own right, it is principally interesting as a prelude to future studies involving more potentially interesting physical processes. One of the biggest questions facing the SM now is whether the so-called Higgs mechanism accurately describes the process by which particles acquire mass. In the summer of 2012, the ATLAS and CMS collaborations announced the discovery of a new particle with a mass of approximately 125 GeV which appears consistent with the predictions made by the Higgs mechanism [3] [4]. Vital to a deeper understanding of this potential connection is the study of events containing a pair of top quarks, and the so-called Higgs boson. For a Higgs boson with mass at the value observed by ATLAS and CMS, the dominant decay mode for the Higgs is $H \rightarrow b\bar{b}$. This means that the $t\bar{t} + H \rightarrow t\bar{t}b\bar{b}$ channel will offer a useful way to test whether the new Higgs-like particle is indeed the long-awaited Higgs boson. A proper understanding of the $t\bar{t} + b + X$ process is crucial to this kind of study. There are also a number of theories for physics beyond the SM which predict excesses in $t\bar{t} + b\bar{b}$ candidate events above the SM, and which would have $t\bar{t} + b + X$ as a primary background. We study the production of $t\bar{t} + \text{HF}$ as a first step towards understanding $t\bar{t} + b + X$.

When HF quarks are produced in a pp collision, they form a shower of collimated hadrons, which is referred to as a ‘jet.’ Jets which contain b , and to a lesser extent c , quarks can be differentiated from jets which do not by extrapolating the observed tracks of the hadrons

which compose the jet back to a vertex which is displaced from the primary collision vertex. In general, a jet identified as containing a b -quark is termed a b -tagged jet.

We choose to focus on $t\bar{t}$ candidate events in which both tops are assumed to decay to leptons (the dilepton mode): $t\bar{t} \rightarrow W^+b W^-\bar{b} \rightarrow l^+\nu b l^-\nu\bar{b}$. The dilepton mode is preferred because it precludes events where additional c -quarks are produced via a $W \rightarrow c\bar{s}$, and thus makes identifying HF quarks not from the $t\bar{t}$ decay easier. Specifically, in the dilepton mode, it is known that the b -tagged jets in our signal contain either the b -quark produced directly by the top decay, additional HF quarks, or light quarks and gluons (which together comprise ‘light flavor’ of LF jets). The measurement of $t\bar{t} + \text{HF}$ is made by selecting a sub-set of $t\bar{t}$ candidate events en-riched in additional HF jets by requiring 3 or more b -tags. To determine the flavor composition of these events, we then perform a fit to the mass of the displaced vertex of the b -tagged jets.

The direct physical question of interest for this analysis is how often an extra jet in a $t\bar{t}$ event comes from HF. We choose to define this measurement as a ratio of production cross-sections inside the visible acceptance of the ATLAS detector. The numerator of this ratio measures the rate of $t\bar{t} + \text{HF}$ production, while the denominator measures the rate of producing $t\bar{t}$ events with at least one additional jet. By quoting the measurement in this way we are able to reduce the overall systematic uncertainty, and directly address our primary question of interest.

This thesis is organized as follows. In Chapter 2, a selection of theoretical details relevant to the analysis are introduced. Special attention is also given to how particles in the SM are measured by a detector like ATLAS. Chapter 3 reviews the LHC accelerator complex, and the ATLAS detector. The detector components are introduced with special attention given to

how various measurement are used in our analysis. The data acquisition system and quality control procedure used to maintain good-quality ATLAS data are presented. The following four chapters are used to outline the bulk of the analysis procedure. In Chapter 4, we detail the data and Monte Carlo samples used in the analysis, as well as the data-driven corrections applied to the Monte Carlo. Chapter 5 presents the object definitions for physics objects, and the selection cuts used to select $t\bar{t}$ candidate events. In Chapter 6, the fitting method used to extract our signal and the details of the cross-section calculation are presented. The details of our systematic uncertainty calculation are presented in Chapter 7. The final two chapters present our results. In Chapter 8, we present control region studies and validate the fitting machinery. Chapter 9 presents the extraction of the final cross-sections using the full 2011 data set.

2 Theory

In this chapter, the Standard Model (SM) of particle physics is introduced. Section 2.1 gives an overview of the SM, from its historical development to its most modern incarnation. In Section 2.2, we review broadly how SM particles (many of which are unstable) are observed at a detector like ATLAS. Particular attention is given to the more massive quarks (t , b , and c), the study of which form the basis of the rest of this thesis.

One key feature of the SM is the symmetry between the electro-magnetic and weak forces, termed the electro-weak symmetry. Of course, this symmetry is not realized in the universe as it is today, as the electro-magnetic and weak forces are observed as distinct entities. The precise details of how this symmetry is broken remains one of the most important issues confronting the SM. In Section 2.3, we discuss in detail the process of electro-weak symmetry breaking, which is mediated by the Higgs mechanism in the SM.

With the theoretical background of the SM in place, we turn our attention to a few theoretical points of interest for the measure of $t\bar{t} + \text{HF}$ events. In July 2012, the ATLAS and CMS collaborations discovered a neutral boson which has properties similar to the SM Higgs boson [3] [4]. To properly call this new particle the Higgs boson, however, one must study the couplings of this particle to other SM particles, including the top quark. In Section 2.4, we discuss how the measurement presented in this thesis can help inform future studies of this new particle and help determine whether it is the long-awaited Higgs boson or not. We also briefly review using this measurement to inform future studies of physics beyond the SM.

2.1 The Standard Model

The Standard Model of particle physics (SM) is a theoretical framework for understanding the fundamental constituents of and interactions in Nature. It is a relativistic quantum field theory (QFT) of twelve fermions interacting through three gauge forces defined by the $SU(3) \otimes SU(2)_L \otimes U(1)$ symmetry group. Developed over approximately 30 years, the SM has quickly become the most successful predictive theory of all time. Predictions of the SM have been tested to exceptional levels of precision, and to-date, no result measured in the context of sub-atomic physics has been found to contradict the SM.

In spite of all of its success, the SM is known to be incomplete. For one, it does not offer a coherent, sub-atomic description of gravity. For another, the SM contains no candidate for dark matter or dark energy, both of which have observed to varying levels in astrophysical experiments [5] [6]. A so-called ‘theory of everything,’ which would extend the SM to cover all observed phenomena, is often considered the Holy Grail of physics, but without more experimental input, it is hard to imagine a single theoretical framework emerging to challenge the SM any time soon.

In this section, we introduce the SM, beginning with its historical development and ending with a summary of the particle content of the theory.

2.1.1 Historical development

While humankind’s desire to understand the nature of the universe dates back to Ancient Greece, our modern understanding of the sub-atomic world began in the 1930’s with Dirac’s work on quantum mechanics. As a theoretical framework, QFT combined three important

areas of physics: classical field theory, quantum mechanics, and Einstein's Special theory of Relativity.

Formulated in 1905, the special theory of relativity led to a new understanding of the causal structure of space-time, and how material particles traverse it. In the late 1800's, it was largely believed that the physical sciences were on the precipice of a complete understanding of the basic principles of the physical universe. This was until the famous Michelson-Morley experiment showed that the speed of light in vacuum was a constant, independent of the relative motion of the observer [7]. This result, when combined with the Maxwell equations for electro-magnetism and Newtonian dynamical laws, led to a contradiction that theories of the day could not resolve. Einstein was able to resolve the conflict by formulating a new set of dynamic laws governing how particles travel through space and time.

Quantum mechanics, which reached maturity in the 1920's, achieved success in describing various experimental results in atomic physics by interpreting sub-atomic particles in terms of mathematical objects called 'wave functions' which live in a Hilbert space. These wave functions determine properties of the particle in a probabilistic manner by considering all possible properties the particle could have. When the wave function is acted on by an outside observer, the infinite number of possible properties are resolved into a single outcome, a process referred to as the 'collapse of the wave function.'

Finally, classical field theory, as its name describes is the somewhat older study of mathematical objects called fields. In physics, a field is an object defined at every point in space-time, which can evolve under the action of external forces. A common example of a classical field theory is electro-magnetism. Here, the fields are the familiar electric and mag-

netic fields, and the dynamical laws which govern their evolution are the Maxwell equations [8].

The first successful application of QFT to fundamental particles was the theory of quantum electrodynamics (QED) [9], which is perhaps most elegantly stated by Richard Feynman. To this day, QED provides accurate predictions about how the electromagnetic force behaves in a quantum regime. Using QED as a model, theories were developed to describe two other fundamental forces of Nature, the strong and weak nuclear forces.

In the 1960's, the electromagnetic and weak forces were shown to be two parts of a single, more fundamental force, called the electro-weak (EW) force by Weinberg, Salam, and Glashow [10] [11] [12]. The brilliance of the theory was to show that a single EW force, with four massless degrees of freedom, would naturally evolve to a theory of two forces, one with three massive degrees of freedom and one with a single, massless degree of freedom. The massless particle is the familiar photon of QED, while the three massive particles are the W^\pm and the Z^0 . In 1984, the UA1 and UA2 experiments at CERN were able to discover the W and Z particles, thus confirming the model. Of particular interest as of the writing of this thesis is how the EW symmetry is broken. The simplest explanation is the so-called Higgs mechanism [9], which breaks the symmetry by introducing a single extra field. One prediction of the Higgs mechanism is the presence of a neutral 'Higgs' particle. As of the writing of this thesis, the Higgs has not been definitively discovered, but there is mounting evidence that a discovery is imminent after a new particle with many Higgs-like properties was simultaneously discovered by the ATLAS [3] and CMS [4] collaborations in 2012. A more detailed discussion of Higgs physics will be given later in this chapter.

To date, there have been a number of moderately successful attempts to unify the strong

and EW forces under some more general symmetry group, a process termed Grand Unification. Unfortunately, direct evidence of Grand Unification may be hard to come by, given that no present or planned collider is likely to have anywhere near the energy to probe the energy scales of Grand Unification. Studies are underway, however, to search for evidence of Grand Unified theories at low energies, as indicated in [13]. Attempts have also been made to incorporate gravity into the SM [9] [14], but this has met with even less success. A potentially exciting example of this is string theory [15], which promises a consistent theoretical framework for understanding gravitational interactions on the same level as the familiar SM ones. To date, however, there is no experimental evidence in direct support of string theory.

2.1.2 Quarks and leptons

There are two sides to the SM: the particles that the theory describes, and the forces which mediate interactions between them. In this section, we discuss the former.

Generally in quantum mechanics there are two kinds of particles: fermions and bosons [16]. The key difference between the two is in how the multi-particle wavefunction behaves under the exchange of any two particles. Fermions are anti-symmetric under such an exchange:

$$\psi_{fermion}(p1, p2, \dots) = -\psi_{fermion}(p2, p1, \dots)$$

while bosons are symmetric:

$$\psi_{boson}(p1, p2, \dots) = \psi_{boson}(p2, p1, \dots)$$

For fermions, this fact leads to the well-known Pauli exclusion principle, which states that no two fermions can occupy the same quantum state. For bosons, there is no such restriction, and indeed some of the most fascinating results from low-temperature physics arise when a large number of bosons collapse into a single quantum state called a Bose-Einstein condensate [17].

For relativistic theories, there is a connection between the statistics a particle obeys (Fermi or Bose) and a property of the particle called ‘spin’ [18]. Spin is a quantum mechanical phenomena that manifests as the intrinsic angular momentum of a particle. Under this connection, fermions have half-integer spin values ($\pm 1/2, \pm 3/2, \dots$), while bosons have integer spin values ($0, \pm 1, \pm 2, \dots$). In the SM, all of the building blocks of matter are fermions, and all force carrying particles are bosons. The Higgs boson is somewhat distinct: it is a boson, but does not mediate any gauge force.

The SM contains twelve spin-1/2 fermions, which can naturally be divided into two groups based on their SM quantum numbers: leptons and quarks. Leptons and quarks both carry the electromagnetic and weak charges, while quarks alone carry the color charge of the strong interaction. Bound states of quarks form (among other things) the proton and neutron, which together form atomic nuclei. With electrons (the lightest charged lepton), nuclei form atoms, which are the basis for all known matter in the universe¹.

Another feature of the SM is that it includes ‘anti-matter.’ For each lepton and quark, there exists a particle with exactly the same properties (mass, spin, etc.) but opposite electric charge. When a particle and its anti-particle meet, they will mutually annihilate. In

¹As alluded to, astrophysical measurements indicate that the universe is made up of more than atoms, but no direct evidence of so-called dark matter has been found.

fact, one of the most important questions facing the SM is why there is more matter in the universe than anti-matter. Probably the most widely known example of anti-matter is the anti-particle of the electron, termed the positron. Positrons were theorized by Paul Dirac in 1928, and discovered experimentally in 1932 by Carl Anderson (a discovery which earned him the 1936 Nobel Prize). Today, they are used widely in medical imaging, and for a number of particle physics experiments. Other anti-particles have been produced, perhaps most famously anti-protons, which were used at, among others, the Tevatron experiment at the Fermi National Accelerator Laboratory in Batavia IL. For charged leptons, it is conventional to refer to anti-particles simply by their charge (e^+ for the positron, compared to e^- for the electron). For quarks, the conventional notation for an anti-quark is to place a ‘bar’ over the quark label (\bar{t} for the anti-top, compared to t for the top).

There are six quarks in total, arranged in three generations of increasing mass: the up (u) and down (d) in the first and lightest generation, the strange (s) and charm (c) in the second, and the bottom (b) and top (t) in the final and heaviest generation. The three “up-type” quarks (u , s & t) carry a $+2/3$ electrical charge, while the three “down-type” quarks (d , c & b) carry a $-1/3$ electrical charge. The mass spectrum for quarks is very broad: the heaviest quark (the t) is nearly 1000 times the mass of the lightest quark (the d). As will be described more in the next section, the strong force forbids the observation of single quarks: quarks can only exist in Nature in bound states called ‘hadrons.’ Generally, a hadron is what is termed a ‘color singlet.’ The charge of the strong force, by convention, is termed color, and carries three possible values: red, blue, and green. Anti-quarks carry ‘anti-color’: anti-red, anti-blue, and anti-green. Hadrons are color neutral states: a combination of quarks each with different colors (red/blue/green or anti-red/anti-blue/anti-green), or a quark and

anti-quark of the same color (red/anti-red, blue/anti-blue, or green/anti-green). The former combination is termed a ‘baryon.’ Common examples of baryons are the proton and the neutron. The latter combination is termed a ‘meson.’ No stable mesons exist, but they have been produced and studied in high energy particle collision experiments since just after World War II.

There are also six leptons, arranged in three generations. There are three leptons with a charge of -1 (the electron (e), muon (μ), and tau (τ)), and three uncharged leptons (the electron-neutrino (ν_e), muon-neutrino (ν_μ), and tau-neutrino (ν_τ)). The mass spectrum of the charged leptons is also quite large: the mass of the τ is over 3000 times the mass of the e .

The mass spectrum for the neutrinos is much less well known. It has proven difficult to perform accurate measurements of the neutrino mass, both because neutrinos interact only via the weak force, and because the neutrino mass appears so close to 0. Specifically, it was assumed that neutrinos were exactly massless, until a deficit in the flux of ν_e ’s coming from the Sun [19] was observed. This deficit is most naturally understood as evidence that neutrinos have non-zero mass, and that this mass allows neutrinos of one flavor to oscillate to another flavor. To be precise, the three flavor states (ν_e, ν_μ, ν_τ) are a super-position of three separate states (ν_1, ν_2, ν_3) with different mass [20]. The mass thus couples flavor states, and allows a neutrino of one flavor to change into another flavor. By measuring the rate of the oscillation for different combinations of neutrinoes (e.g. $\nu_e \rightarrow \nu_\mu$, or $\nu_e \rightarrow \nu_\tau$), one can infer the square of the mass splittings (e.g. $|m_1^2 - m_2^2|$ or $|m_1^2 - m_3^2|$). Much work is underway to measure these splittings with increasing precision, but the absolute magnitude of the neutrino masses and their order ($m_1 > m_2 > m_3$ or $m_1 < m_2 < m_3$) remains unknown.

2.1.3 Symmetry and gauge forces

With the benefit of hindsight, we can say that there are three fundamental forces relevant to particle physics: the electromagnetic, strong, and weak forces. In the modern understanding, each force is mediated by a set of particles called mediators, and affects any particle which carries the ‘charge’ of the force. The electromagnetic force, studied extensively since the 1800’s, is mediated by the photon, which has been known to physics in some form since the days of Isaac Newton. The strong force is responsible for the formation of protons and neutrons, and generally keeping atomic nuclei together. The charge of the strong force is often called ‘color’ or ‘color charge’ to differentiate it from the more familiar electric charge, and the strong force is mediated by eight particles called ‘gluons’. The weak force is responsible for some rare nuclear decay processes, and is mediated by the W and Z bosons.

The focus of this section is to draw out how these forces are described in the mathematical language of the SM. The foundation of the SM, in many ways, is the concept of symmetry. It is known that the SM (and any relativistic quantum field theory) contains a set of operations one can perform on the fields that comprise the theory that will leave the predictions of the theory unchanged. Such an operation is called a symmetry of the theory. For mathematical consistency, the presence (or imposition) of a symmetry requires the existence of extra particles. In the SM, these extra particles are bosons that mediate interactions between the lepton and quark fields. The SM symmetries are termed ‘gauge symmetries’ specifically because they are symmetries related to changing the gauge or ‘phase’ of the associated fields. As such, the particles produced by these symmetries (and the forces these particles mediate) are called ‘gauge forces.’

Using QED as an example, consider a complex vector field $\psi(x)$. A field of this form was shown by Dirac to describe a spin-1/2 particle, like an electron. The relativistic dynamics for such a particle were first described by Dirac in the famous equation which bears his name. The Lagrangian for ψ which leads to the Dirac equation is [21]:

$$L = i\bar{\psi}\gamma_{\mu}\delta^{\mu}\psi - m\bar{\psi}\psi \quad (1)$$

where γ_{μ} are the gamma matrices, δ^{μ} is the ordinary differential operator, and m is the mass of the particle. In this context, μ is an index with separate values for each space-time dimension (x , y , z , and t). It is understood that when the same index appears in a superscript and a subscript, it is summed over.

Quantum mechanics tells us that physical observables are proportional to $\bar{\psi}\psi$, where $\bar{\psi}$ is the complex conjugate of the ψ . Thus, physical results must be invariant under the following transformation:

$$\psi \rightarrow e^{i\alpha}\psi$$

where α is any real number. In the terminology used in the literature, this is a phase or gauge transformation, hence the phrasing mentioned earlier. It is easy to verify that the Lagrangian for the Dirac equation is invariant under this transformation, so we term this a gauge symmetry of that Lagrangian. Because α is simply a number, this is termed a global gauge symmetry.

All of this is well and good, but something interesting happens if we *demand* that this gauge symmetry applies locally, that is to say independently at each point in space-time. To

do this, we require the following relation:

$$\psi \rightarrow e^{i\alpha(x)}\psi$$

where $\alpha(x)$ is now a general function of space-time coordinates. The so-called mass term $(m\bar{\psi}\psi)$ is invariant under this transformation, but the kinetic term $(i\bar{\psi}\gamma_\mu\delta^\mu\psi)$ is not. The problem is that the ordinary derivative acts also on $\alpha(x)$. The solution is to define a new, so-called ‘covariant derivative’:

$$D^\mu = \delta^\mu - iqA^\mu$$

where A^μ is called the gauge field, and must transform according to:

$$A^\mu \rightarrow \frac{1}{q}\delta^\mu\alpha(x)$$

The new, gauge invariant Lagrangian is given by:

$$L = i\bar{\psi}\gamma_\mu D^\mu\psi - m\bar{\psi}\psi = \bar{\psi}(i\gamma^\mu\delta_\mu - m)\psi + q\bar{\psi}\gamma^\mu\psi A_\mu \quad (2)$$

where the new term can be interpreted as an electron (described by ψ) interacting with a photon (described by A^μ) with strength proportional to the electric charge (q). A physical photon field will also have a kinetic term, so the final, gauge invariant Lagrangian for QED is:

$$L = \bar{\psi}(i\gamma^\mu\delta_\mu - m)\psi + q\bar{\psi}\gamma^\mu\psi A_\mu - \frac{1}{4}F_{\mu\nu}F^{\mu\nu} \quad (3)$$

where

$$F_{\mu\nu} = \delta_\mu A_\nu - \delta_\nu A_\mu$$

is the field strength tensor for the electro-magnetic force, as described by Maxwell's equations. The key here is that the imposition of a local gauge symmetry leads to a new field, which can be interpreted as mediating the interaction between other particles in the theory. Put another way, if one starts with a theory containing some number of particles, the interactions between the particles can be thought of as the result of mathematical symmetries one demands the theory obey.

The SM has three principle symmetries, formally referred to as $SU(3)$, $SU(2)$, and $U(1)$. QED, which was discussed above, arises from a $U(1)$ symmetry (though not the SM $U(1)$). As we saw, there is one transformation related to this symmetry, and thus one new field. The number of separate transformations (termed 'generators' of the symmetry) turns out to be equivalent to the number of new fields.

Within the SM, the weak and electromagnetic forces arise from the combined symmetry group of $SU(2)$ and $U(1)$. The charge of the $U(1)$ symmetry is termed 'hypercharge' (to differentiate it from the electromagnetic charge) and has a generator Y . The $SU(2)$ symmetry has three generators labeled T_1 , T_2 , and T_3 . The electrically neutral EW bosons (the photon and Z^0) are formed by linear combinations of Y and T_3 , while the charged bosons (W^+ and W^-) are formed from combinations of T_1 and T_2 .

Similarly, the strong force is governed by the $SU(3)$ symmetry, and has eight generators (leading to the gluons). The strong force (referred to often as QCD, in analogy with QED)

is so-named because the coupling of particles under this force is many orders of magnitude larger than the next most strongly coupled force (the electromagnetic), at least in low energy environments. Formally, the generators for a non-Abelian symmetry do not commute with each other (they do for an Abelian symmetry like $U(1)$). This leads to the complication that gluons are also colored objects, meaning the mediator of the strong force is also charged under the strong force. Note the difference from QED where the photon does not have electric charge. This leads to a number of interactions not possible in QED like the self-interaction of gluons.

One of the crowning achievements of the SM was showing that the electromagnetic and weak forces are aspects of a higher-dimensional symmetry group ($SU(2)_L \otimes U(1)$) acting on electro-weak hyper-charge. This combined symmetry is termed the electro-weak (EW) symmetry. Since we observe distinct electromagnetic and weak forces, it is known that the EW symmetry is broken in our universe. In the SM, the EW symmetry (which is exact at high temperatures just after the Big Bang) is dynamically broken by the Higgs mechanism as the universe cools. We discuss the Higgs mechanism in more detail in Section 2.3.

2.2 Phenomenology at the LHC

Rather unfortunately, it is not possible to directly observe many of the particles described in the preceding two sections at a hadron collider like the LHC. With a few exceptions, all of the particles that have been discussed are unstable, and will decay to lighter particles as they travel away from the central collision point. Due to a property of QCD called confinement, it is actually impossible to observe single quarks [21]. In this section, we discuss briefly how

each of the particles described in the previous section are measured at ATLAS.

The specifics of QCD make it impossible to measure a single quark. Roughly speaking, the reason for this is that the strength of the QCD interaction between two quarks grows with the separation between them. The forces we are familiar with (gravity and electromagnetism) grow weaker as the separation between interacting particles increases. Because of this peculiar feature of QCD, as two quarks are pulled apart, the binding energy between them actually grows. At some point, there is enough energy to pair produce a new pair of quarks which then immediately form bound states with the existing quarks. The process of forming these new bound states is referred to as hadronization, as the final state hadrons are stable enough to travel some distance in the detector.

Hadrons themselves are not, as a rule, stable, and many will decay with some characteristic lifetime as the quarks which make them up decay into a lower-energy state. The obvious exception is the proton, which is completely stable (at least in the SM). As a high-energy hadron traverses the detector, it will generally initiate a cascade decay resulting in a collimated shower of secondary hadrons. This collection of particles is often reconstructed as an object called a ‘jet’ within the ATLAS detector.

Of particular interest to this analysis are the properties of hadrons containing b or c quarks. Most unstable hadrons formed with only lighter quarks (u, d, s) have a lifetime of 10^{-24} s. By contrast, hadrons containing b and c quarks tend to have a much longer lifetime: 10^{-12} s for B mesons, and 10^{-15} s for D mesons [22]. The reason for this large difference in lifetime is the force which mediates the decay process. Decays mediated by the strong or electro-magnetic forces lead to a short lifetime, but if such decays are suppressed (or actually forbidden), then the decay must proceed via the weak force, leading to a longer lifetime.

This extended lifetime allows for the differentiation of b (and to a lesser extent c) hadrons assuming the detector's tracking resolution is good enough to resolve the distance traveled by the b hadron before its decay (and subsequent formation of a jet). This measurement is made by extrapolating the measured tracks back to an assumed secondary decay vertex. More details of how b -jets are identified at ATLAS can be found in Chapter 5.

Gluons, like quarks, are not directly observable due to features of the QCD interaction. Being colored particles, gluons can also form jets and are only identifiable as such.

Charged leptons are very useful particles at a hadron collider, typically indicative of interesting physical processes. Electrons are, as we know, completely stable, and thus can be measured directly. Muons are not completely stable, but it is known that the average lifetime of a muon traveling near the speed of light is over 600 m. This is much longer than the average muon track through the ATLAS detector, so we consider muons to be stable, observable particles. Taus, by contrast, are not stable, and decay well within the detector, after traveling only 80 μm on average. The dominant decay mode for a tau is $\tau \rightarrow h\nu$, where h is some charged hadron. Decays directly to lighter leptons ($\tau \rightarrow l\nu\bar{\nu}$) or three charged hadrons ($\tau^\pm \rightarrow h^\pm h^\pm h^\mp$) are also possible.

Photons are also stable, and can be measured directly inside of ATLAS. One complication is that photons will readily interact with material inside of the detector and convert to a pair of electrons: $\gamma \rightarrow e^+e^-$. Nonetheless, the ATLAS calorimeter provides excellent photon identification.

The final class of particles that we must consider are those, like the τ , which are completely unstable. The W and Z bosons fit this description, as do the top quark and the (hypothetical) Higgs boson. Both weak bosons decay with an average lifetime of 10^{-25} s,

essentially immediately for all observable purposes. Approximately two thirds of W decays proceed to hadrons, with just under half of these proceeding via $W \rightarrow c\bar{s}$. Most of the remaining third of W decays proceed via $W \rightarrow l\nu$, where l is any charged lepton. Two thirds of Z decays proceed to quarks via $Z \rightarrow q\bar{q}$. Approximately 20% go to neutrinos, and the remainder are to charged leptons. The top quark is unique among the quarks in that it decays so fast (approximate lifetime of 10^{-25} s) that it does not undergo hadronization. It is also unique in that almost exactly 100% of top decays proceed via $t \rightarrow Wb$. Observation of the top quark, then, hinges on observing W 's and b 's, as described above.

The Higgs boson, if it exists with properties predicted by the SM, will behave similar to the W and Z bosons: its average lifetime is approximately 10^{-25} s, and it is only observable through its decay products. The dominant decay mode for the SM Higgs with a mass of 125 GeV is $H \rightarrow b\bar{b}$, while other channels of interest are $H \rightarrow \tau\tau$, $H \rightarrow ZZ$, $H \rightarrow WW$ and $H \rightarrow \gamma\gamma$.

2.3 Electroweak symmetry breaking

As discussed above, one of the major open questions facing the SM is how the symmetry between the electromagnetic and weak forces is broken. In this section, we discuss in some detail the EW symmetry breaking process as it is described in the the SM.

While the discussion of QED given above is generally correct, there is a problem that comes about when QED is combined with the weak force. Specifically, the mass term for ψ in equation 3 is not invariant under the gauge transformation of the combined EW symmetry. In fact, it turns out that imposing the EW symmetry forbids any mass terms of this form,

and thus makes the SM a theory of massless particles only. The SM breaks the EW symmetry (and thus acquires massive particles) using what is known as the Higgs mechanism [21]. The basic principle behind the Higgs mechanism is to introduce a doublet of complex fields ϕ_h which interacts with all other SM particles (including the EW bosons). At high energies, these interactions are no different from any other particle-to-particle interactions in the theory. Gauge invariance requires that all particles are massless in this regime. At low energies, however, something special happens.

It is generally assumed that the value of a SM field is zero when the energy contained in that field is also zero. This is merely the statement that a field does nothing if it has no energy. The Higgs field, however, is different. It is assumed that the Higgs field obeys a potential of the general form:

$$U = \frac{-1}{2}a^2\phi_h^2 + \frac{1}{4}b^2\phi_h^4$$

which has a minimum at $\phi_h = \pm a/b$. Thus, at low energies, the value of the Higgs field (what is usually called a vacuum-expectation-value or ‘vev’) is non-zero. As such, at low energies, we can replace the value of the *dynamical* Higgs field with a constant:

$$\bar{\psi}\psi\phi_h^2 \rightarrow \bar{\psi}\psi(a/b)^2$$

which is exactly the form of the old mass term in equation 3. The important difference is that this term only exists after the EW symmetry is broken at low energies. Thus the Higgs mechanism allows massive particles in a gauge invariant theory by spontaneously generating mass as the theory enters a low energy regime where a higher symmetry is broken down into

two lower symmetries.

2.4 Implications for future measurements

Measuring the $t\bar{t} + \text{HF}$ rate is interesting for a number of reasons. While the technique of performing a vertex mass fit to determine the flavor composition of jets has been used in previously published works [23], it has never been performed in an environment with an irreducible b -jet background. More importantly, however, it has significant implications for a number of future measurements. In this section, we review some of these measurements.

While the Higgs mechanism is the favored explanation for EW symmetry breaking, it has not been proven to be the correct one. However with the recent discovery of a Higgs-like boson with mass near 125 GeV, there is excitement that such a proof may come soon. Indeed, an important piece of the LHC physics program in the near future is to determine whether the couplings of this new particle are consistent with SM expectations for the Higgs or not. To date, the measured couplings of the Higgs-like object appear to be consistent with the SM expectation, but more data will be needed to pin this down. A crucial piece of this picture (and one which has not yet been directly measured with much precision) is the measurement of the Yukawa coupling between the Higgs and the top quark. The decay $H \rightarrow t\bar{t}$ is forbidden by kinematics, so the next leading candidate is to look for the associated production of $t\bar{t} + H$ in the same event. At tree level, the cross-section for this process is directly proportional to the desired coupling, so an accurate measurement of $\sigma(t\bar{t} + H)$ will help pin down an important property of the new boson. Information on the coupling can be inferred from other measurements ($H \rightarrow \gamma\gamma$), but these processes occur with loops, and so

are also sensitive other couplings.

As discussed previously, the most likely decay mode for the Higgs is $H \rightarrow b\bar{b}$, meaning $t\bar{t} + H, H \rightarrow b\bar{b}$ will be a significant part of the effort to measure $\sigma(t\bar{t} + H)$. For a given top selection, the dominant background to this process will be the SM production of $t\bar{t} + b\bar{b}$ via various QCD processes. While this has been studied in various theoretical calculations [1], no measurement of inclusive $t\bar{t} + b\bar{b}$ has been performed in the data. While this thesis studies the inclusive production of all extra HF ($b, b\bar{b}, c,$ and $c\bar{c}$), it nonetheless represents an important first step in understanding this crucial background. With more data, it is easy to envision using the same analysis method to separately measure $t\bar{t} + b + X$, and thus directly get at the desired cross-section.

Finally, the $t\bar{t} + \text{HF}$ final state is also interesting from the vantage point of exploring physics beyond the SM. Models with composite quarks [24], [25], [26] and [27], Kaluza-Klein excitations of the gluon [28], or non-resonant, top-philic interactions [29] all predict excesses in this channel over the SM. A solid understanding of the SM rate for $t\bar{t} + \text{HF}$ is crucial for any such studies.

3 The LHC and ATLAS detector

In this chapter, we describe the experimental apparatus used in this analysis: the Large Hadron Collider (LHC) and the ATLAS detector. We begin with a brief overview of the LHC accelerator chain in Section 3.1. First, the individual components of the detector are introduced, and we describe how they are used to measure the physically observable particles.

Like many multi-purpose particle detectors, ATLAS is composed of three main groups of detectors: the inner tracker (Section 3.2), the calorimeters (Section 3.3), and the muon chambers (Section 3.4). The signature used to define the signal region in this analysis (two isolated, high p_T leptons, and three or more high p_T , b -tagged jets) requires a good understanding of all three of these components. An event display showing an early $t\bar{t}$ candidate event is shown in Figure 2. In this event, the top quarks decay to electrons. Hits in all sectors of the detector are shown.

A combination of online and offline checks are performed on the data to select (or trigger) on events which are likely to contain physically interesting collisions section. If an event successfully passes these so-called trigger checks, it is written to tape for further offline analysis. The trigger system as a whole is described in Section 3.5. Once the data are collected, the status of the detector during the data taking period is assessed offline by a dedicated data quality control group. Depending on which sub-systems are experiencing which issues, a given data run may be flagged as usable or un-usable, depending on criteria defined by each physics group and their particular needs. Taken together, the recommendations from the data quality group is expressed as a ‘good run list’ (GRL) which analyzers use to select only runs where the data from ATLAS is well-understood and accurate. We summarize the

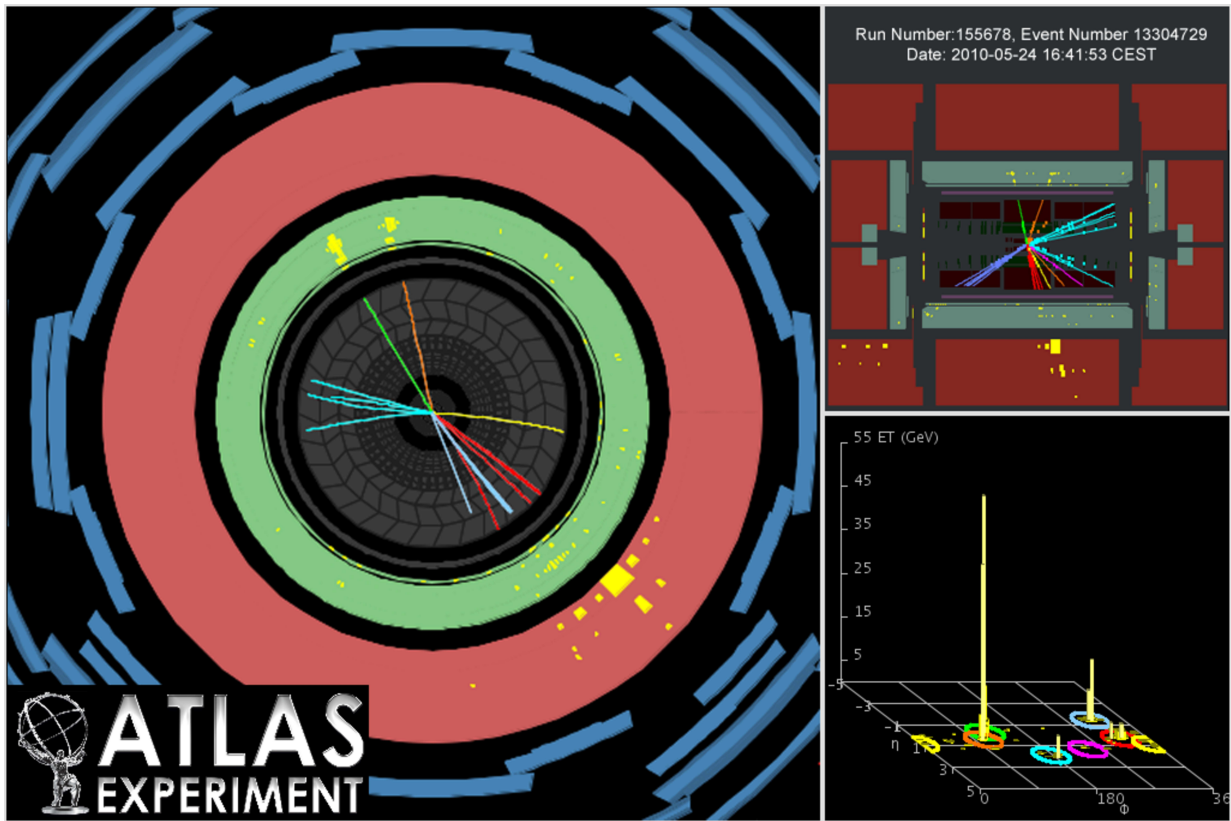


Figure 2: An event display for a $t\bar{t}$ candidate event in the di-electron decay mode. The event was recorded in 2010 during the first run of collision taking data at ATLAS. The two electrons are indicated by upward pointing green and orange lines. Additional jet activity (as evidenced by deposits in the red hadronic calorimeter) can also be seen.

procedures that are in place to ensure high quality data in Section 3.6.

3.1 CERN, and the LHC

The European Center for Particle Physics (CERN) has a long tradition of cutting edge research in the field of sub-atomic physics. Founded in the 1950's, CERN has been responsible for a number of important results, first in the field of nuclear physics, and more recently in elementary particle physics. First approved in 1994, the Large Hadron Collider (LHC) has been the flagship experiment at CERN since its predecessor, LEP, finished in 2000. The LHC was designed as a proton-proton (pp) collider, with a total center-of-mass energy $\sqrt{s} = 14$ TeV, and instantaneous luminosity of 10^{-34} cm^{-2} s^{-1} . As of the writing of this thesis, the LHC operated briefly at $\sqrt{s} = 900$ GeV in 2010 before a prolonged run at $\sqrt{s} = 7$ TeV in 2011. In 2012 and the first two months of 2013, the LHC operated at $\sqrt{s} = 8$ TeV, with a peak instantaneous luminosity of 5×10^{33} cm^{-2} s^{-1} . After a year-long shutdown, it is expected that the LHC will operate at higher center of mass energies starting in 2015.

While the LHC is responsible for accelerating the protons to their final energy, it is required that protons entering the LHC already have an energy of 450 GeV. To accomplish this, a complex of input accelerators are used to bring the protons from rest, up to the energy required by the LHC. The first stage involves a linear accelerator (the LINAC-2) which takes the protons from rest up to 50 MeV. The Proton Synchrotron Booster (PSB) takes protons from the LINAC, and bring them up to the input energy required for the next step. A circular Proton Synchrotron (PS) accepts protons from the PSB, and bring them

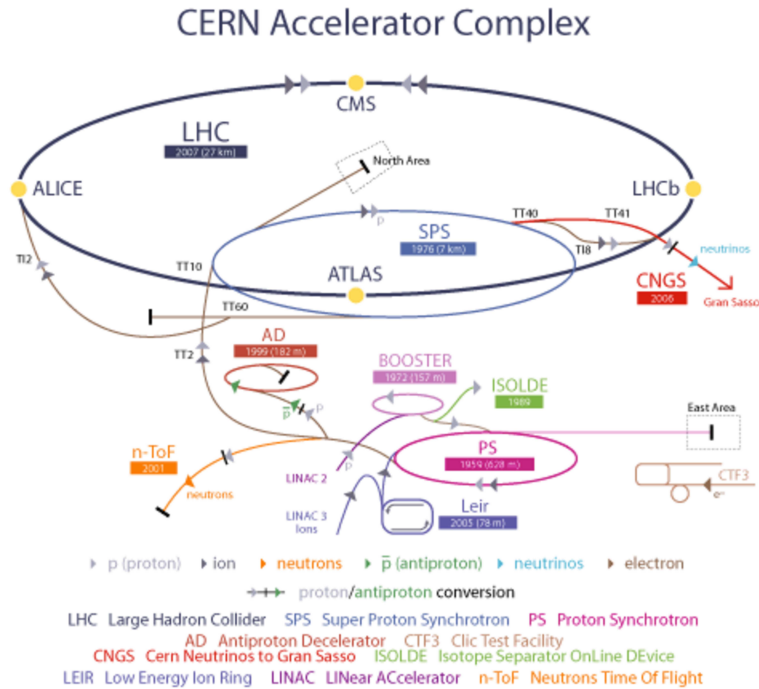


Figure 3: The accelerator complex at CERN. Protons are accelerated from rest to their final energy incrementally through a series of five machines: the LINAC, the PSB, the PS, the SPS, and the LHC. Much of the infrastructure is built from facilities used in previous experiments.

up to 28 GeV. An upgraded version of the PS, called the Super Proton Synchrotron (SPS) accepts protons from the PS and brings them up to 450 GeV. Finally, depending on the precise configurations of its magnets, the LHC is capable of accelerating protons up to their final energy (4 TeV in the current configuration, and up to 7 TeV by design).

Despite different design specifications, the basic physical principle used to accelerate protons throughout the LHC complex is, more or less, the same. Developed first in the 1940's, the principle of synchrotron accelerators is to contain particles using a magnetic field, and guide them with a constant frequency electromagnetic field. Direct acceleration is provided via radio-frequency (RF) cavities, while dipole and quadrupole magnets are used for fine adjustments to the beam trajectory. The maximum energy achievable by a given

accelerator is determined by the strength of the provided magnetic field, and the size of the ring. Modern synchrotrons utilize superconducting magnets to achieve higher magnetic fields. A consequence of this is that extensive cryogenic systems must be used to keep the magnets operating with the desired field strength.

3.2 The inner tracker

One piece of information often measured at detectors like ATLAS is the track produced by a charged particle as it traverses the detector. Historically, many of the first particle detectors were tracking chambers, and particles were identified strictly based on measurements of the track. While this is not suitable for modern analyses, tracking chambers nonetheless still have an important role to play.

The ATLAS inner tracker is designed to provide precision measurement of the trajectory that charged particles take as they leave the central interaction point. As a unit, the inner tracker and its associated services are contained in a cylindrical envelope whose length is 7024 mm and whose radial size is 1150 mm. This envelope is placed in a 2T solenoidal magnetic field. There are three main components to the inner tracker: a pixel detector, a silicon micro-strip detector (the Semiconductor Tracker or SCT), and a drift-tube detector (the Transition Radiation Tracker or TRT). The Pixels and SCT rely on fine granularity silicon technology to provide high-precision measurements of track parameters closest to the interaction point. The TRT, by contrast, has a much coarser inherent granularity, but benefits from a much larger volume over which to make its measurement. The TRT is also useful for particle identification as it is able to separate charged pions from electrons. Figure

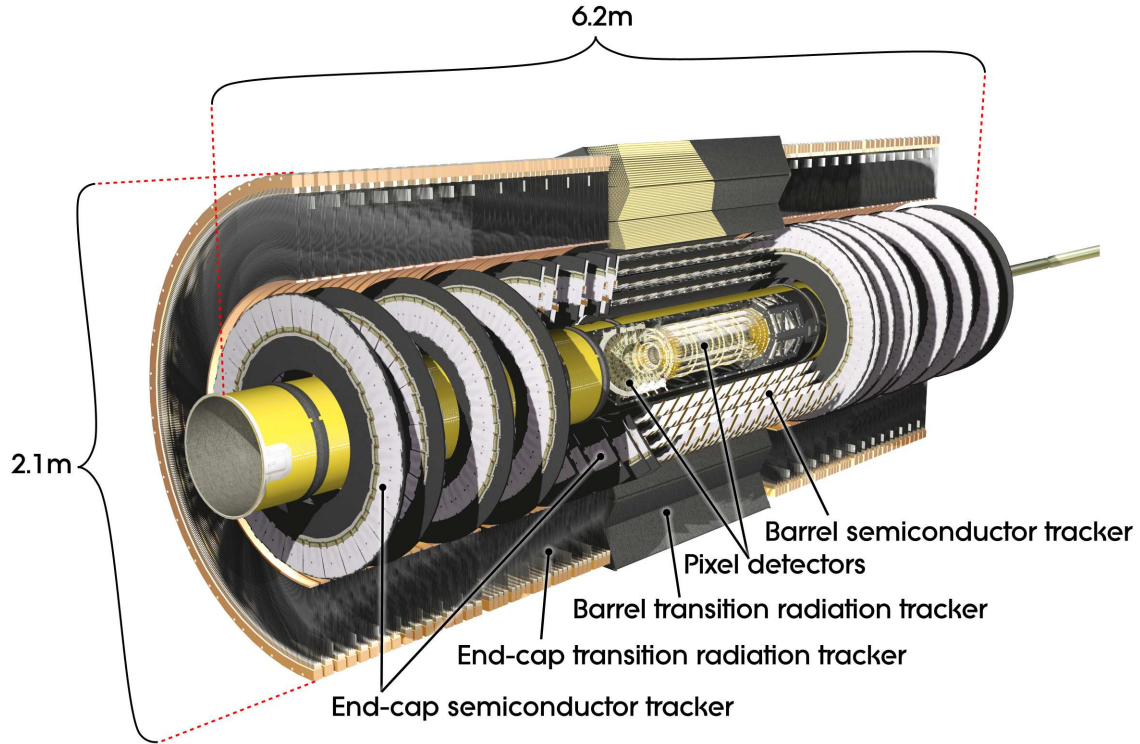


Figure 4: A graphic of the ATLAS inner tracker. Generally, the inner tracker is arranged in a central barrel region, with two endcaps. The system provides momentum measurements for charged particles for $|\eta| < 2.5$. The three main components of the tracking system (the Pixels, SCT, and TRT) are shown separately.

4 shows a graphic representation of the inner tracker.

In general, each detector element registers ‘hits’ as charged particles traverse them. Track-finding algorithms take these hits and form tracks. It is known that charged particles follow helical trajectories in the presence of a magnetic field, so these tracks, in general, will be curved according to:

$$p = BQr$$

where p is the momentum of the particle, Q is the charge, B is the magnetic field, and r is the radius of curvature. An accurate measurement of the track (and thus the radius of

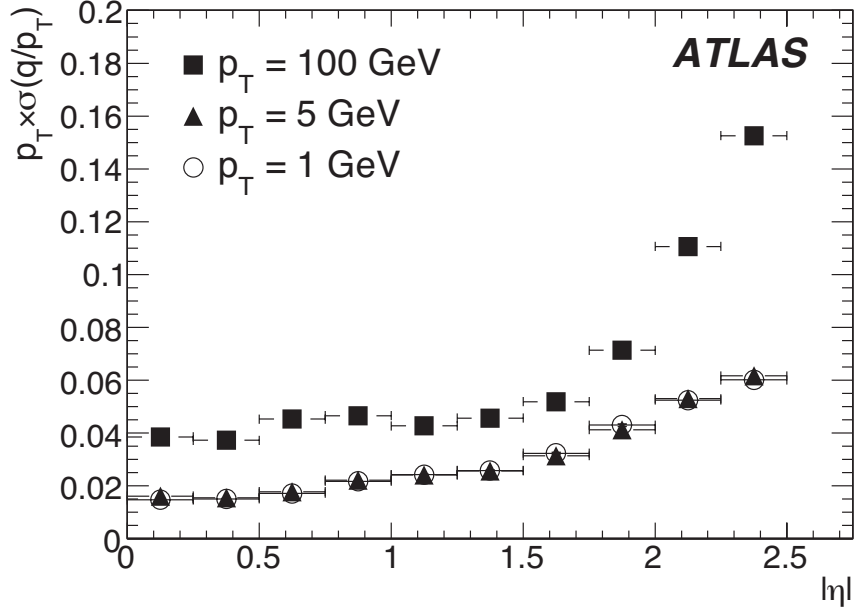


Figure 5: The relative momentum resolution for muons with $p_T = 1, 5,$ and 100 GeV as a function of the η of the muon.

curvature) is thus a measure of the particle’s momentum. Using only information from the inner tracker, ATLAS is able to achieve a relative resolution of less than 10% for central muons, as indicated in Figure 5.

3.2.1 The Pixel Tracker

The Pixel tracker uses silicon pixels to measure the position of charged particles near the interaction point: the Pixels occupy a radius between 5 and 12 cm from the beamline, and are arranged in a central barrel module with two endcap modules. The barrel consists of three concentric layers, and each endcap contains three wheels. As described in [30], the Pixel tracker contains 1744 individual sensors, each with 46080 readout channels. Each sensor is a $250 \mu\text{m}$ charge detector using oxygenated n -type wafers. As charged particles traverse the sensor element, they create free electrons which travel to and are readout by

electrodes in the chip. Once enough charge is accumulated, a hit is registered. An applied voltage of 150-600 V is used to maximize the charge collection efficiency at each electrode.

Each cell provides two dimensional location information on the hit (in local x and y coordinates as defined by the surface of the wafer). While pixel technology is generally more expensive to construct and operate than other, older designs, it offers resolutions of approximately $10\ \mu\text{m}$ in local x and $115\ \mu\text{m}$ in local y , far better than other types of tracking systems. Pixels are also very sensitive to prolonged radiation exposure, and need to be replaced after long running in high luminosity environments. Maintaining low running temperatures can help mitigate this effect, so the Pixel tracker is typically run at -5 to $-10\ ^\circ\text{C}$.

3.2.2 The Semiconductor Tracker

The Semiconductor Tracker or SCT operates on many of the same principles as the Pixel tracker. There is a central barrel region with four layers of concentric modules (2112 in total), and two sets of nine endcap wheels (with a total of 1976 modules). Detector elements in the SCT are single-sided 6cm-long wafers, glued together on opposite sides of a module with a 40 mrad stereo angle. Each module has 768 readout channels per side, for a total of over 6.3 million.

Hits are registered when free electrons created by charged particles as they pass through the detector element are readout by an electrode. To achieve high charge collection efficiency, the SCT is maintained at 150-350 V, depending on running conditions and age. The resolution of the SCT is approximately $17\ \mu\text{m}$.

3.2.3 The Transition Radiation Tracker

Unlike the Pixels and SCT, the Transition Radiation Tracker (TRT) is based on polyimide drift tubes surrounding a gold-plated tungsten wire. The tubes are 4mm in diameter and contain a mixture of 70% Xe, 27% CO₂, and 3% O₂. The wire is maintained at a voltage of -1530 V, and is mechanically reinforced by supporting carbon fibers to prevent sagging. The TRT has a barrel region with 96 modules arranged in three concentric layers, covering a radial distance of 56 - 107 cm. Two sets of 40 endcap wheels are arranged in two structures (the 'A'- and 'B'-type wheels). In total, the TRT has 350,848 readout channels, and is capable of tracking resolution on the order of 130 μm .

Beyond the differences in construction, the basic principles used to track particles in the TRT are similar to, but different than, those used in the Pixels and SCT. As charged particles travel through the drift tubes, they ionize gas molecules and thus create free electrons. These electrons drift to the central wire, with a maximum drift time of approximately 48 ns. Once enough charge is collected, a hit is registered.

The TRT is unique in that it employs two sets of thresholds, as described in [30]. The first threshold is typically set at 250 eV, and is set to be triggered by minimum ionizing particles. The primary purpose of this threshold is to construct tracks. The second threshold is typically set at 6 keV, and should only be triggered by electrons. A polyurethane radiator is interwoven around adjacent drift tubes. When an electron interacts with this radiator, it will generate a shower of δ photons which cascade into the tube. Other charged particles (e.g. π 's) will not lead to this shower. These photons induce more ionization within the gaseous mixture, and thus more charge accumulation. In this way, by counting the number of hits

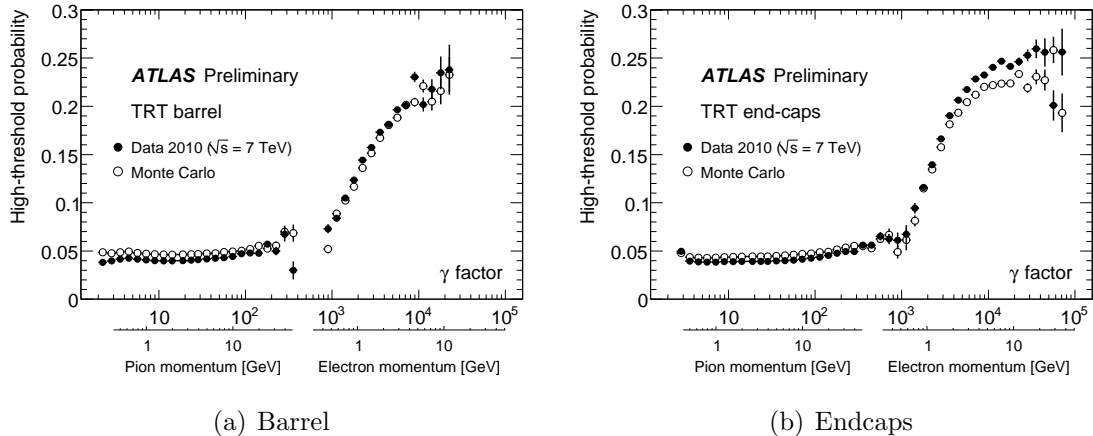


Figure 6: The fraction of high-level hits measured in the barrel (a) and endcap (b) regions of the TRT for electron and pion tracks, as a function of track momentum. At momenta above approximately 10 GeV, electrons exhibit a fraction of high-threshold hits around 25%, while pions at the same momentum have a fraction closer to 5%. This information is used by ATLAS to reduce the pion background when selecting electrons.

which pass the so-called high threshold, the TRT can be used to identify electrons. Figure 6 shows the fraction of high-threshold hits for electron and pion candidates in the TRT. As can be seen, electrons with momentum above approximately 10 GeV have a high-threshold fraction approximately 5 times larger than a pion of the same momentum.

3.3 The calorimeters

Another common measurement technique used at detectors like ATLAS is the measurement of the total energy content of particles produced in the decay. Often, this measurement involves the use of calorimeters. The basic principle of a calorimeter is that it measures the energy of a particle by absorbing it. In so-called sampling calorimeters, the particle is absorbed in stages: it passes through alternating layers of radiators (which cause the incident particle to generate a shower of secondary particles) and absorbers (which absorb the secondaries). By measuring the energy content of the secondaries, we measure the

energy of the initial incident particle. Other types of calorimeters are possible, the CMS electromagnetic calorimeter for instance [31].

Located outside the inner detector, ATLAS uses two main calorimeter systems to measure the energy of all out-going particles, with the exception of muons and neutrinos. While different in exact details, both are sampling calorimeters. The first (inner) stage of the calorimeter is designed primarily to absorb particles which interact electro-magnetically (electrons, photons, and to some extent charged hadrons). The second (outer) stage of the calorimeter is designed to absorb particles which interact chiefly via the strong interaction (both charged and neutral hadrons). Together with the inner detector, the calorimeter system allows for excellent reconstruction of electrons and charged hadrons. A graphic of the whole calorimeter system is shown in Figure 7.

Since they do not leave a track in the inner detector, photons and neutral hadrons are re-constructed by the calorimeter alone. Muons deposit a small amount of their energy in the calorimeter system, but a dedicated muon system is needed to measure them with any usable efficiency.

3.3.1 Liquid argon calorimeters

The inner section of the ATLAS calorimeter is designed for the measurement of the energy of electro-magnetically interacting particles out to $|\eta| < 4.9$. Housed in two endcap and one barrel cryostat, the liquid argon (LAr) calorimeter is so-named because it uses liquid argon as the active medium. The barrel cryostat contains an EM calorimeter, while each endcap cryostat contains an EM calorimeter, a hadronic calorimeter, and a forward calorimeter to cover the region nearest the beam line. In the barrel and endcap EM calorimeter, lead is

used as the primary absorber. The endcap hadronic and forward calorimeters use copper and copper/tungsten, respectively. Precision measurements are made using three sampling layers in the central-most region of the detector ($|\eta| < 2.5$). Two sampling layers are used in the more forward region ($2.5 < |\eta| < 3.2$), which contains the overlap between the barrel and endcap EM components, as well as the endcap hadronic component. The forward calorimeter is responsible for the most forward region ($3.1 < |\eta| < 4.9$). Taken together, the EM calorimeter has 226,176 readout channels, while the hadronic calorimeters have 18,312 readout channels.

3.3.2 Tile calorimeter

The tile calorimeter is located outside the liquid argon calorimeter, and is specialized in the detection of the energy of hadronic particles, for $|\eta| < 1.7$. The active medium for the Tile calorimeter is made of specially made scintillator tiles. The absorber is steel. The tile calorimeter is divided into a central barrel, and two extended barrels. Each barrel contains 64 modules with alternating layers of active medium and absorber. These barrels are oriented radially outward, and normal to the beamline. Photo-multiplier tubes are used to collect the photons generated by interactions in the scintillator. In total, the tile calorimeter contains 13,944 readout channels.

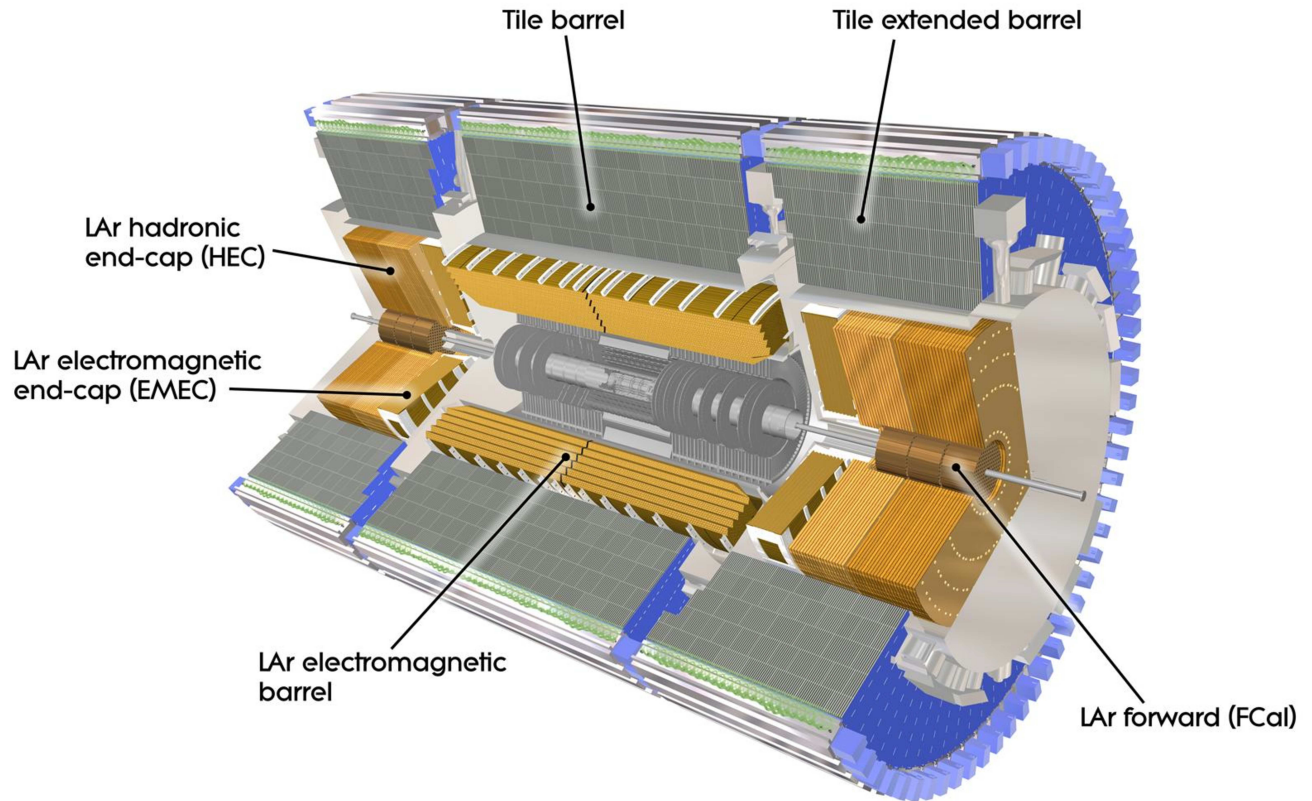


Figure 7: The ATLAS calorimeter systems. The liquid argon systems are used to detect particles which interact electro-magnetically (in the EM calorimeter), as well as via the strong force (in the hadronic end-caps and forward calorimeters). The tile calorimeter is used to measure hadrons in the central region of the detector.

3.4 The muon system

A dedicated system is constructed specifically to trigger and track muon candidates, as they will not generally leave large energy deposits in either calorimeter system. While the Inner Tracker will measure a muon's track, proper muon identification requires more information than the Tracker alone can provide. There are four main components of the ATLAS muon system: resistive plate and thin gap chambers for triggering, and cathode strip and monitored drift tube chambers for muon tracking and identification, as shown in Figure 8. Three large air torroidal magnets, one in the barrel and two in the endcaps, provide a magnetic field for the muon system. The endcap torroids are rotated by an angle of 22.5° with respect to the barrel to provide optimal coverage and bending power.

3.4.1 Monitored Drift Tube chambers

As mentioned previously, a dedicated detection system is needed for the proper identification of muons. A central piece of this system is the Monitored Drift Tube chambers (MDT's). As their name suggests, the MDTs are based around drift tube technology. The basic detecting element in the MDTs is a 29.970 mm drift tube with a central tungsten-rhenium wire held at a potential of 3080 V. The tube is immersed in a mixture of 93% Ar and 7% CO₂. As muons traverse the drift tube, they induce the ionization of the gas mixture. Free electrons produced in this way drift toward the wire, with a maximum drift time of 700 ns.

MDT's are arranged in three concentric layers in the barrel around the beam pipe, and in three planes perpendicular to the beam pipe in the endcaps. They provide coverage over a range of $|\eta| < 2.7$ for the whole detector, but only $|\eta| < 2.0$ for the innermost layer in the

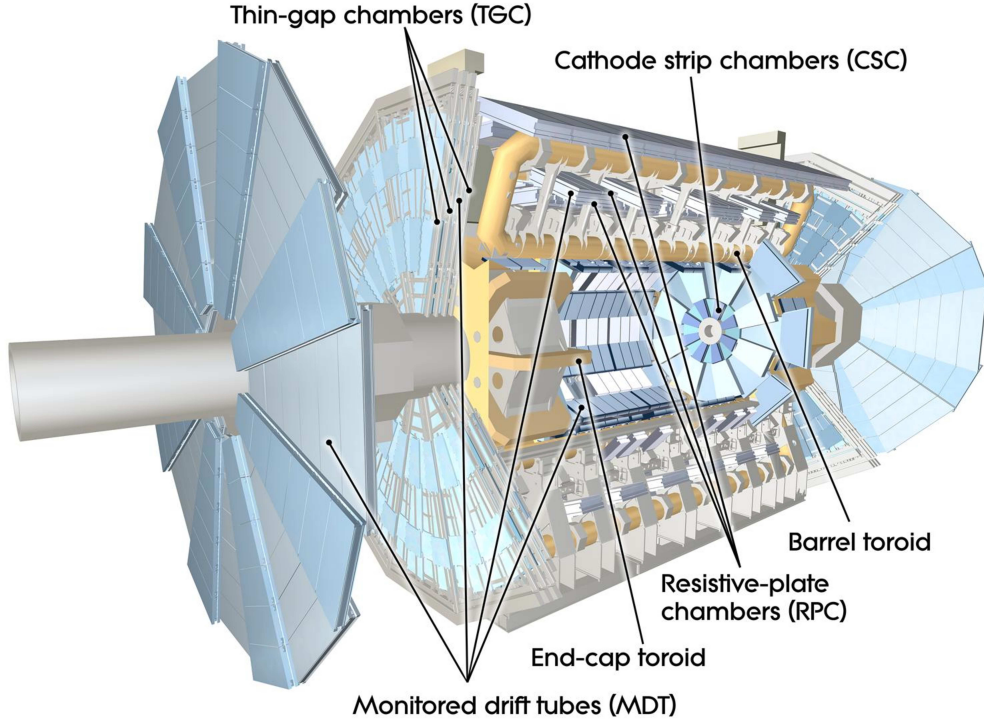


Figure 8: A graphic displaying the muon system at ATLAS. The Monitored Drift Tube chambers and Cathode-Strip chambers provide precision tracking information for muon candidates using drift chamber technology. Triggering is handled by the Resistive Plate and Thin Gap chambers. A torroidal magnetic field allows for the measurement of muon momentum by the observed bending of the muon track.

barrel. The drift tubes are collected into 1150 chambers, and give a total of 354,000 separate readout channels.

3.4.2 Cathode-Strip chambers

The Cathode-Strip chambers (CSC's) are multiwire proportional chambers, operating on a similar drift tube detection principle as the MDT's. They principally provide extra muon identification at higher values of $|\eta|$ where the readout rate is too high for the MDT's. As multiwire proportional chambers, CSC's contain a series of anode wires held at a voltage of 1900 V, relative to two cathode strips, as shown in Figure 9. The distance between the cathode strips and the anode wires is 2.5 mm. A mixture of 80% Ar and 20% CO₂ fills the

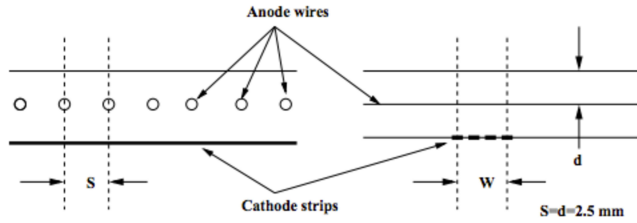


Figure 9: A graphic showing the layout of anode wires and cathodes strips in the Cathode-Strip chambers. Muon tracks are measured by charge accumulation at the cathode strips.

space between the anodes and cathodes. When a charged particle traverses the gas, it will ionize atoms in the gas, causing free electrons to drift to the cathodes with a maximum drift time of 40 ns. Unlike the MDT's which rely on charge accumulation at the wire, tracking resolution in the CSC's is achieved by interpolating the charge accumulated on each cathode strip.

Specifically, the CSC's cover $2.0 < |\eta| < 2.7$, adding to the measurements for muons in this η range provided by the outer layers of the MDT's. The CSC's are grouped into 32 chambers, with a total of 31,000 readout channels.

3.4.3 Resistive plate chambers

Resistive-Plate chambers (RPC's) use parallel electrode plates without wires to trigger on muons in the central region of the ATLAS detector. The plates are constructed of phenolic-melaminic plastic laminate, and held at a distance of 2mm from one another by insulating spacers. The space between the plates is filled with a gaseous mixture of 94.7% $C_2H_2F_4$, 5% Iso- C_4H_{10} , and 0.3% SF_6 , which ionizes as charged particles traverse the inter-plate volume. An electric field of 4.9 kV/mm is maintained between the two plates, and free electrons created by the ionization of the gas molecules drift along the electric field lines to be readout. RPC's are grouped into 606 chambers, with a total 373,000 readout channels. They

give coverage to the central part of the ATLAS detector, corresponding to $|\eta| < 1.05$.

3.4.4 Thin gap chambers

Thin gap chambers (TPC's) complement the RPC's and allow for triggering of muons at higher η , as well as supplementing the tracking capability of the MDT's. The TPC's are multi-wire proportional chambers, with two wires immersed in a mixture of 55% CO₂ and 45% n-C₅H₁₂. Graphite cathodes are located 1.4 mm from the anode wires, compared with a 1.8 mm wire-to-wire separation. This leads to a total cathode-to-cathode gap of 2.8 mm. The anode wires are held at a potential of 2900 V. The TPC's are collected in a combination of double and triple-wire units called chambers. In total, there are 3588 chambers, with a total of 318,000 readout channels. Coverage from $1.05 < |\eta| < 2.4$ is given for the trigger, while the TPC's give measurement coverage out to $|\eta| < 2.7$.

3.5 The trigger and data acquisitions system

To efficiently record data as it is measured by the detector, ATLAS employs a three level trigger system to identify interesting events. It is actually not possible with the technology we have to record all of the data put out by ATLAS during normal running. The raw output rate is approximately 40 MHz, with each non-empty event requiring approximately 2 MB of disk space. In order to be faithfully written to disks, the output rate must be reduced to a few hundred Hz.

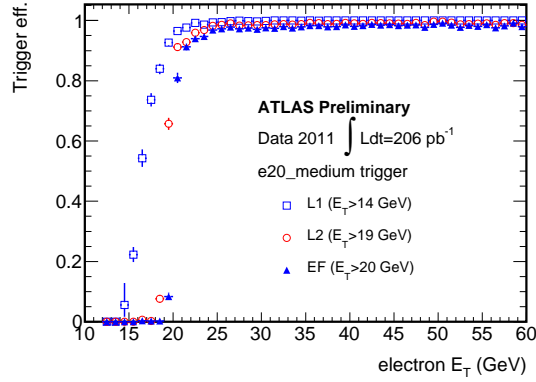
The first level, called Level 1 or L1, is based on custom-made electronics. L1 trigger decisions are made entirely with detector-level information and identify so-called 'regions of interest' (ROI). ROI's include electron, muon, and τ candidates, highly energetic jets, signif-

icant E_T^{miss} , and large total transverse energy. For muons, information from the RPC's and TGC's are used. The calorimeters are responsible for all other L1 trigger measurements. After L1 trigger decisions, the output rate is decreased to 100 kHz, with a maximum processing time of $2.5 \mu\text{s}$.

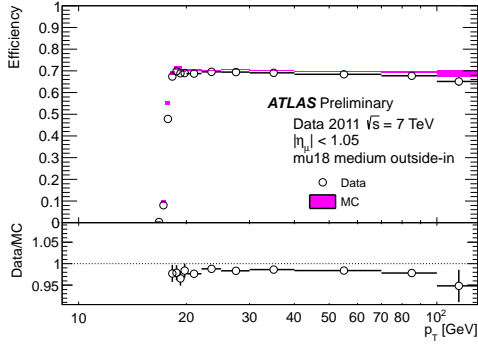
The next two levels in the trigger system, called the Level 2 (L2) and event filter, form what is called the High-Level Trigger (HLT). The L2 trigger is seeded by ROIs from the L1 trigger. Fast processing of detector level data is done at L2, and some rough object reconstruction is done. After L2, the output rate is reduced to 3.5 kHz with an average processing time of 40 ms. The event filter uses full event information to further select interesting events. The final output rate is on the order of 200 Hz, with an average processing time of about 4 s.

The precise details of the cuts used by the trigger system are not generally constant in time, or even during a single data taking run. As conditions at the LHC change, the raw input rate of data increases. However, it is required that the final output rate remain approximately constant. For a fixed set of L1 cuts trigger selections, if the final output rate of the HLT cannot be made small enough, events are randomly dropped from processing. This procedure is called 'pre-scaling' the trigger. Generally, pre-scaled trigger streams are not used in physics analyses, as they contain only a sub-set of the total available data. In this analysis lepton triggers are used to select interesting events. As the peak luminosity at the LHC increased (see Chapter 4), the minimum p_T cut used by the lepton triggers is increased.

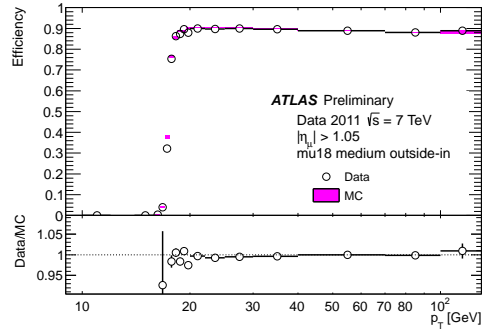
The efficiency of the lepton triggers used in this analysis (and in general) are a function of the p_T of lepton. The precise turn-on curve for a given trigger is usually measured in



(a) Electron trigger



(b) Muon barrel trigger



(c) Muon endcap trigger

Figure 10: Trigger efficiency as a function of p_T for electrons and muons, as measured in $Z \rightarrow ll$ events. The electron trigger chain is e20 medium, shown in (a). For muons, the trigger chain is mu 18 medium, and the efficiency is plotted separately for muons reconstructed in the barrel ($|\eta| < 1.05$) (b) and the endcaps ($|\eta| > 1.05$) (c).

$Z \rightarrow ll$ using a tag-and-probe method. Figure 10 shows the trigger efficiency for the e20 medium and mu18 medium triggers. To ensure that our selected leptons are not sensitive to the trigger efficiency turn-on curve, reconstructed leptons are required to have p_T slightly above the point at which the efficiency curve plateaus.

3.6 Data quality and GRL's

The quality of the data recorded by ATLAS ultimately depends on how well the various detector components are operating. If there is a mechanical failure or other read-out inefficiency in part of the detector, any analysis object which uses this information as input will be affected. To ensure that this feature does not affect the quality of analysis-level work, ATLAS has created a Data Quality (DQ) sub-group responsible for assessing how much data is usable from a given run period. The DQ group receives input from other ATLAS sub-groups (the various detector groups, as well as dedicated combined performance groups, whose goal is the proper reconstruction of objects like electrons, muons, and jets) and flags a run as usable or not, based on a logical 'OR' of this input. The amount of data that is deemed usable is termed a good run list, or 'GRL.'

The most restrictive GRL, termed 'All good,' requires that all sub-groups report no issues with the data-taking. In 2011, approximately 5.2 fb^{-1} of data were collected, with an efficiency for the All good GRL of approximately 90%, as indicated in Figure 11. Depending on the physics needs of a specific analysis, a looser GRL may be used to recover some fraction of integrated luminosity. Generally, analysis groups within ATLAS determine in a self-consistent way what GRL is to be applied. Owing to the nature of its complicated final

state, the ATLAS Top group recommends a GRL very close to All good. Taking into account all inefficiencies, the GRL used in this analysis corresponds to a total integrated luminosity of 4.7 fb^{-1} . Given the large number of runs involved, it is not efficient to reproduce the GRL in this thesis.

ATLAS p-p run: March-October 2011										
Inner Tracker			Calorimeters		Muon Spectrometer				Magnets	
Pixel	SCT	TRT	LAr	Tile	MDT	RPC	CSC	TGC	Solenoid	Toroid
99.8	99.6	99.2	96.9	99.2	99.4	98.8	99.4	99.1	99.8	99.3
All good for physics: 89.9%										
Luminosity weighted relative detector uptime and good quality data delivery during 2011 stable beams in pp collisions at $\sqrt{s}=7$ TeV between March 13 th and October 30 th (in %) - corresponding to 5.2 fb ⁻¹ of recorded data. This data quality status refers to the data after the summer reprocessing campaign.										

Figure 11: The data quality efficiency for all sub-detectors, weighted by total integrated luminosity, for each detector component during the 2011 run. The ‘All good’ fraction shown refers to the fraction of the data marked as usable by all sub-groups.

4 Monte Carlo and data samples

In this chapter, the details of the data and Monte-Carlo samples used in this analysis are presented. The Monte-Carlo samples are given in Section 4.1. Information about the data set is found in Section 4.2. In Section 4.3, we discuss the scale factors which are applied to the Monte-Carlo in order to more accurately reproduce the data. By convention, the spatial separation between physics objects is defined using a cone $\Delta R = \sqrt{(\Delta\phi)^2 + (\Delta\eta)^2}$, where $\Delta\phi$ is the separation in ϕ and $\Delta\eta$ is the separation in η between the two objects.

4.1 Monte Carlo Samples

We use both inclusive $t\bar{t}$ samples and those in which $t\bar{t}$ is accompanied by extra HF partons at the matrix element level, as generated by the ALPGEN MC generator [32]. The parton shower is modeled using the HERWIG package [33], and the underlying event is modeled with JIMMY [34]. Additional HF quarks can be generated at either the matrix element level, by the underlying event, or during the parton shower. The $t\bar{t}$ samples used in this analysis, along with cross-sections (including k-factors) and ATLAS data-set ID's, are shown in Appendix A. As a notational note, Monte Carlo samples contain so-called 'truth information' which stores information on particles actually produced in an event (rather than particles observed in the detector). Using truth information is often used to understand various detector affects and efficiencies.

A feature of these Monte Carlo samples is that there is some double-counting of processes when the samples are used together: the inclusive $t\bar{t}$ samples contain some events where the extra jet activity is due to HF quarks. To remove this double-counting, we follow the

Process	HFOR designation
Hard scatter HF in HF sample	isHF
Soft scatter HF in HF sample	Kill
Hard scatter HF in inclusive sample	Kill
Soft scatter HF in inclusive sample	isHF

Table 1: Details of how events are classified when combining Monte Carlo samples where extra HF is generated at the matrix element level. Hard scatter HF is defined by requiring the HF partons to be well-separated ($\Delta R > 0.4$). Events in the inclusive sample without HF are designated ‘isLF.’

procedure described in [35], termed heavy flavor overlap removal (HFOR). The motivation for this scheme is to keep $t\bar{t} + \text{HF}$ events which contain a hard scatter from the dedicated HF samples, and to keep events containing $t\bar{t} + \text{HF}$ events which contain a weak scatter from the inclusive samples. A hard scatter is defined by requiring the two HF partons be well-separated ($\Delta R > 0.4$), and is generally better modeled by inclusion in the matrix element than by the parton shower. To be specific, the HFOR algorithm can classify an event as either ‘isHF’ or ‘Kill’ according to the scheme shown in Table 1.

isHF events are kept and Kill events are not used. After the application of the HFOR to the sum of inclusive and HF samples, the $t\bar{t}$ cross-section one measures is measured to be 10% lower than what one obtains using only the inclusive samples. To recover the correct top cross-section, $t\bar{t}$ events are re-weighted by a factor of 1.1.

Samples for the associated production of $t\bar{t}$ pairs with an additional boson (W , Z , or H) generated with the MADGRAPH generator [36] are included for reference, but are not used in the analysis. Details of the Monte Carlo used to model other SM backgrounds are also included in Appendix A. We also apply the HFOR tool to the $W + \text{jets}$ and $Z + \text{jets}$ samples, where necessary. After the application of HFOR in the W and Z samples, no significant difference in cross-section is observed, and so no separate re-weighting is done.

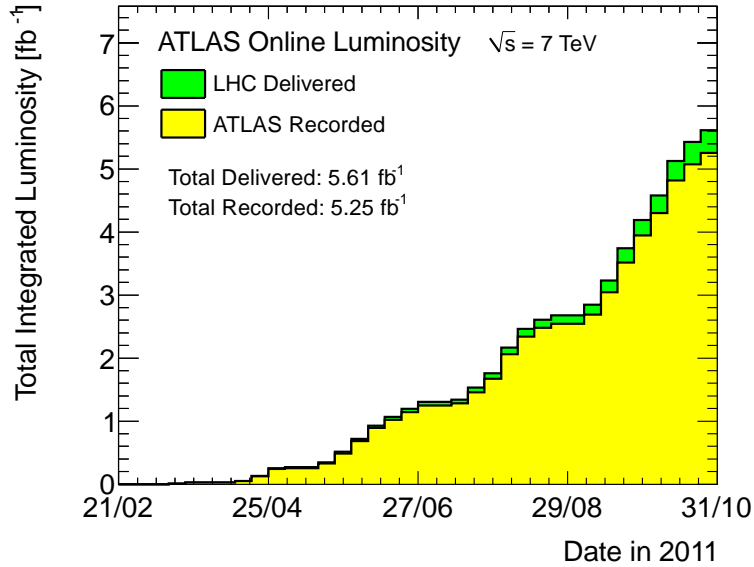


Figure 12: The total integrated luminosity recorded by ATLAS, as a function of time during the 2011 run period.

4.2 Data samples

Data recorded during the 2011 run are used for the analysis presented in this thesis. The top good runs list (GRL) was used in order to assure stable data-taking conditions, corresponding to an integrated luminosity of $\int \mathcal{L} dt = 4.7 \text{ fb}^{-1}$. The integrated luminosity (before the application of a GRL) recorded by ATLAS during the 2011 run is shown in Figure 12. Depending on the data-taking period, different lepton triggers were used. Electron triggers used for the analysis are EF e20 medium (before period K), EF_e22_medium (period K), EF_e22vh_medium1 OR EF_e45_medium1 (period L-M). Muon triggers used for the analysis are EF_mu18 (before period J), EF_mu18_medium (starting period J). Details of each data taking period can be found in Appendix A.

During the 2011 run period, the condition of the LHC beam was constantly changing to deliver higher instantaneous luminosity to the detectors. The most convenient way to

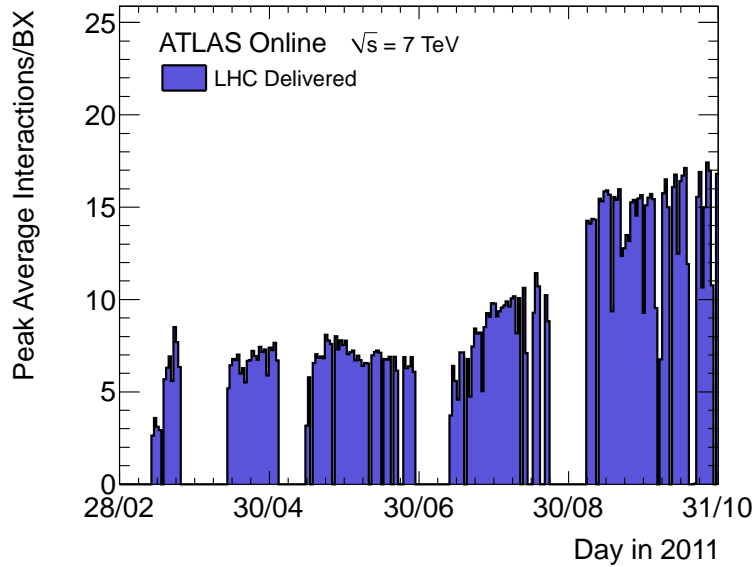


Figure 13: The peak average number of interactions per bunch crossing in data recorded at ATLAS during the 2011 run period.

parametrize this change is by the average number of bunch crossing measured per luminosity block, a quantity referred to as $\langle \mu \rangle$. Roughly, $\langle \mu \rangle$ corresponds to the number of pp interactions that occur during a given bunch crossing. Over the course of the 2011 run period, $\langle \mu \rangle$ increased steadily from approximately 6 to 17, as indicated in Figure 13.

Any additional interactions are generally termed ‘pileup’. There are two types of pileup that can occur: in-time and out-of-time. In-time pileup is defined as additional interactions occurring within the same bunch crossing (as described by $\langle \mu \rangle$). Out-of-time pileup, by contrast, is due to interactions from an adjacent bunch crossing that are still present in the detector. The bunch spacing for the 2011 run period was 50 ns, so the dominant source of pileup is in-time.

4.3 Data-driven corrections to the Monte Carlo

While the Monte Carlo generally describes physical processes well, it is known that certain aspects of the simulation do not describe the data well, or are changing too fast in the data to allow for adequate tuning in the Monte Carlo. To correct for these discrepancies, we define scale factors which are used to re-weight events in the Monte Carlo so the resulting expectation matches the data. Generally, scale factors are defined in some well-understood control region of the data, and then applied to the region of interest. In these control regions, the ratio of data to Monte Carlo is measured, and the result is taken as the scale factors. If many scale factors are needed for a given event, the weight of the event is taken as the product of the individual scale factors. In our analysis, scale factors are needed for the following quantities: lepton identification and trigger efficiency, jet tagging efficiency, pileup jet suppression efficiency, and total pileup content.

The ATLAS Top group has developed a set of common scale factors to be used by all analyses, barring special needs of a particular analysis to use non-standard object or event selection cuts. With the exception of jet tagging efficiency, our analysis uses only these common scale factors.

Scale factors used for lepton identification and trigger efficiency are measured by comparing data and Monte Carlo in $Z \rightarrow ll$ events using the so-called tag-and-probe method. In this type of analysis, one identifies a good ‘tag’ lepton using some tight selection, and then measures the properties of the other ‘probe’ lepton candidate. Generally, the efficiency is measured as a function of the p_T and η of the probe. For electrons, identification scale factors are derived in 9 bins of η and 6 bins of E_T , while trigger scale factors are derived in 18

bins of η . Scale factors for the electron reconstruction cuts used in this analysis, integrated over η and E_T respectively, are shown in Figure 14. For muons, trigger scale factors are parametrized by η and ϕ of the muon candidate, with separate measurements made in the barrel and endcap systems. Reconstruction efficiencies are parametrized by p_T and η as well. Figure 15 shows the total scale factor for muon identification as a function of the number of reconstructed vertices in the event, for a number of possible isolation cuts. Isolation cuts are quoted as either an energy (E_T) measured in the muon chambers or as sum of track p_T around surrounding the muon candidate. For each type of isolation (E_T or p_T), we define a cone in ΔR around the muon candidate and sum up the energy (or momentum) inside the cone. Cone 20 refers to a cut of $\Delta R < 0.20$, cone 30 refers to a cut of $\Delta R < 0.30$, and so on.

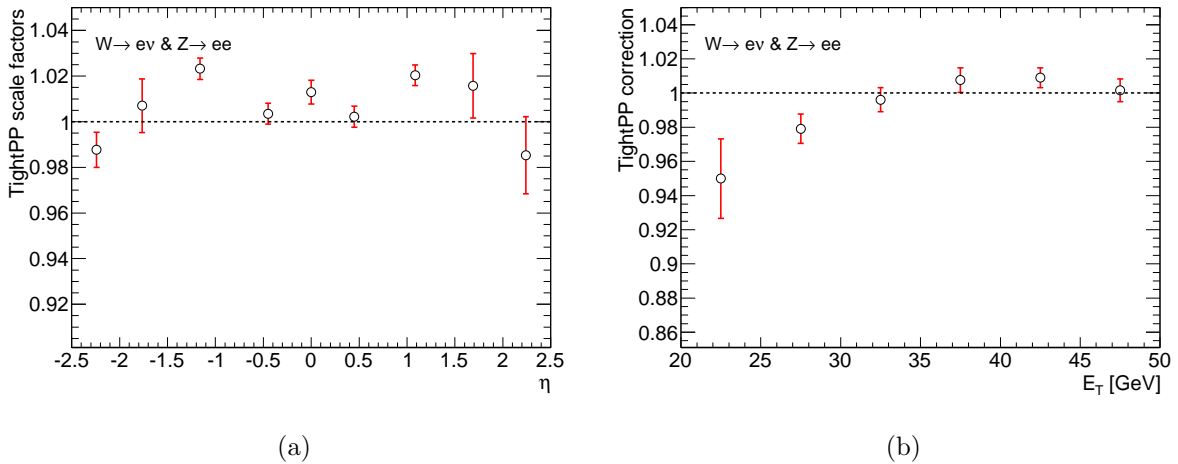


Figure 14: Electron **Tight++** scale factors as a function of η (integrated over $E_T > 20$ GeV) (left) and E_T -corrections (right).

Scale factors for the b -tagging efficiency of jets is measured separately for b , c , and light-flavor jets, as well as a function of the p_T and η of the jet. The scale factors for b -jets are derived from $t\bar{t}$ control samples, and measured as a function of p_T and η of the jet. For c -jets, scale factors are derived by a dedicated study of D^* decays. Light jet tagging scale factors

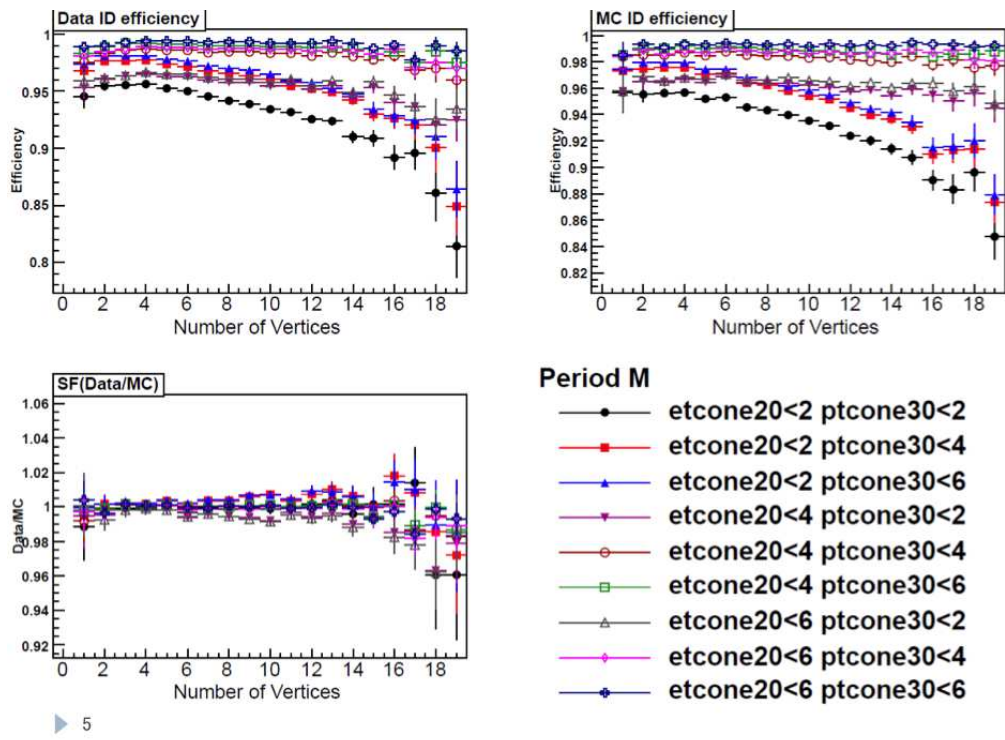


Figure 15: Muon scale factors as a function of the number of reconstructed vertices in the event. Different isolation cuts are compared. Subsequent optimization studies showed that the best option was to require E_T (cone 20) < 2 GeV and p_T (cone 30) < 4 GeV (red squares).

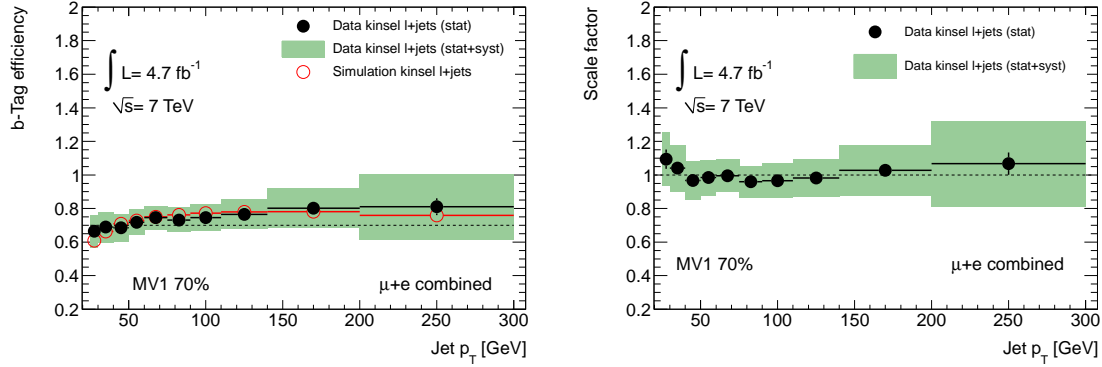


Figure 16: The b -jet tagging efficiency estimated from data compared with the efficiency estimated from Monte Carlo simulations (left) and the resulting scaling factors (right) together with statistical and systematic uncertainties for the tagger MV1 as a function of p_T at the working point corresponding to 70% efficiency.

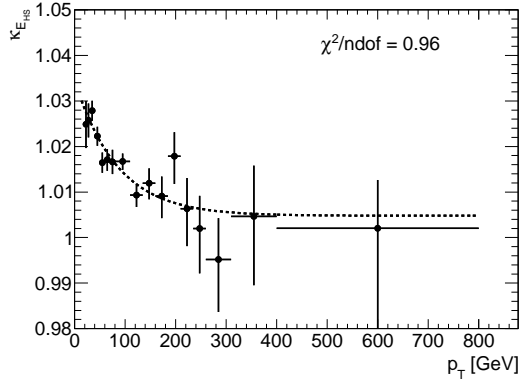
are derived by performing a fit to the vertex mass returned by the ATLAS SV0 b -tagging algorithm. ATLAS recommends certain cuts (termed ‘operating points’) on the output of each b -tagging algorithm, and scale factors are derived separately for each operating point and tagger. In Figure 16, the b -tagging efficiency in data and Monte Carlo, as well as the resulting scale factor, are shown as a function of p_T for the MV1 tagger at the operating point corresponding to 70% b -tagging efficiency.

When performing control region studies for this analysis, the default scale factors are used, as tagged jets are defined by simply requiring the output of the MV1 algorithm to be above some value. However, as described in Section 6, we derive new scale factors (albeit in terms of the default ones) for the purpose of our signal measurement. The reason for this is that the signal measurement is made by considering jets in separate, mutually exclusive bins of MV1 output.

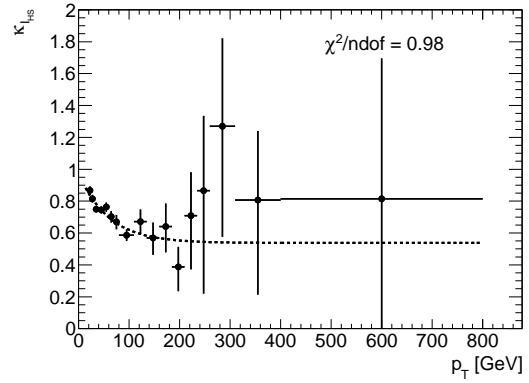
Another aspect of jet reconstruction and identification which requires correction is the efficiency for jets to pass the JVF cut (described in Chapter 5. This cut is aimed at removing

jets arising from pileup interactions, and so treats jets from pileup separately from jets coming from the primary vertex (so-called ‘hard scatter’ jets). Scale factors are measured separately for pileup and hard-scatter jets, as well as for jets which pass and fail the JVF cut. In the Monte Carlo, hard-scatter jets are defined as jets with $p_T > 20$ GeV which match to jets in the truth record (pileup interactions are not stored in the truth record). Pileup jets in the Monte Carlo are any jets which do not match an object in the truth record. Efficiencies in the data are measured using $Z + \text{jet}$ events. For hard-scatter jets, we require a good Z (which has decayed to two leptons) with $p_T > 10$ GeV, and two back-to-back jets with $p_T > 20$ GeV. Pileup jet efficiencies are measured in events with a good Z with $p_T < 10$ GeV, and a single jet with $p_T > 20$ GeV. Scale factors as a function of jet p_T for hard-scatter jets are shown in Figure 17. The corresponding scale factors for pileup jets are shown in Figure 18.

Finally, it is known that a number of kinematic properties depend on the amount of pileup in an event. For in-time pileup, we can parametrize this dependence using $\langle \mu \rangle$, as described in the previous section. It is known the $\langle \mu \rangle$ distribution in the Monte Carlo does not match the $\langle \mu \rangle$ distribution in the data: indeed, the $\langle \mu \rangle$ distribution is not the same from one Monte Carlo sample to another. Using the $\langle \mu \rangle$ for a specific event in the Monte Carlo as input, we can re-weight the Monte Carlo such that the final $\langle \mu \rangle$ distributions agree. Of course, this procedure assumes a $\langle \mu \rangle$ distribution from the data, and so will change as different data samples (or portions of a single data sample) are used.

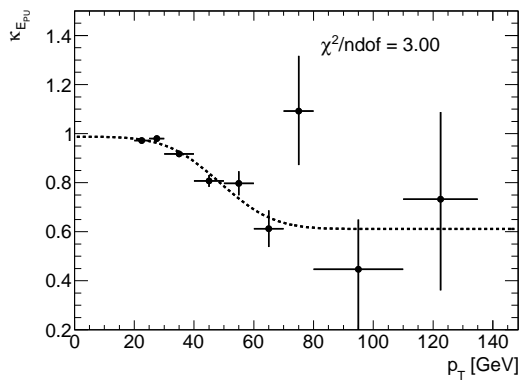


(a)

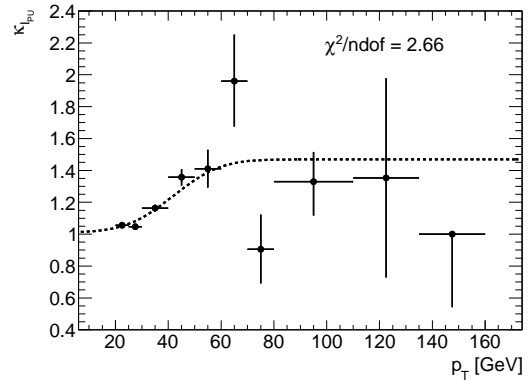


(b)

Figure 17: Hard-scatter (a) efficiency and (b) inefficiency scale factors as a function of the p_T of the jet.



(a)



(b)

Figure 18: Pile-up (a) efficiency and (b) inefficiency scale factors as a function of the p_T of the jet.

5 Object and event selection

In this chapter, the selection cuts used to identify interesting events in the analysis are introduced. Section 5.1 introduces the reconstructed physics objects: electrons (e), muons (μ), and jets. These objects represent physically observable particles that are measured by the ATLAS detector. We additionally introduce the b -tagging algorithm used to identify jets originating with a b quark. By invoking conservation of momentum, we can calculate the missing energy in the transverse plane (E_T^{miss}). Significant E_T^{miss} is an indication that neutrinos are present in the event, and is thus a useful way to select the $t\bar{t}$ signal. Most of the selection cuts used are standard to the rest of the ATLAS collaboration.

Section 5.2 introduces the cuts placed on physics objects to select events likely to contain $t\bar{t}$ pairs. A baseline set of cuts used to isolate $t\bar{t}$ events is outlined, without any requirement on b -tagged jet multiplicity. We define control regions used to validate our simulation and background estimates, using events with low numbers of b -jets. The selection cuts used to measure the cross-section for inclusive $t\bar{t}$ and $t\bar{t} + \text{HF}$ are then described.

Section 5.3 introduces the fiducial volume in which we calculate our fiducial cross-sections. Separate cuts are used for the fiducial measurement of inclusive $t\bar{t}$ and $t\bar{t} + \text{HF}$.

5.1 Kinematic requirements

5.1.1 Electrons

Electrons (e) are identified using the Inner Detector and EM calorimeter systems. We apply the ATLAS-standard ‘tight ++’ selection criteria to identify electron candidates. The tight ++ criteria uses various calorimeter and track measurables to identify electrons and

reject the background from charged hadrons, as described in [37]. Specifically, tight p_T and η -dependent cuts are made on the shower-shape variables as measured in the strips and second compartment of the EM calorimeter. Track quality is enforced by requiring at least 1 hit in the Pixel detector, 7 hits in the SCT, and at least 1 hit in the b-layer. The calorimeter deposit and track are required to match within an η of 0.05, and the candidate must have an impact parameter less than 5.0 mm. A loose requirement is made on the fraction of high-threshold hits in the TRT to reduce the background from charged π 's. Cuts are also made on the ratio of the electron's energy over it's momentum (E/p) to reject converted photons. Using tag-and-probe with electrons from Z boson decays, these cuts are found to be approximately 78% efficient [37].

Electron reconstruction can be based on information from either the inner tracker or the calorimeter, depending on the transverse momentum of the electron candidate. Owing to the large bending of low-momentum tracks, electron candidates with $p_T < 20$ GeV are preferentially identified using information from the inner tracker. For electron candidates above 20 GeV, it is advised to reconstruct electrons using seeds from the calorimeter, due to improved resolution in the calorimeter. Information from the inner tracker is added after the primary calorimeter cluster is identified. Given that electrons produced by top decays generally have momenta above 20 GeV, the calorimeter seeded algorithm is used in this analysis. Beyond the requirements made by the tight ++ quality flag, the following selection criteria are also applied to electron candidates:

- $p_T > 25$ GeV
- $|\eta| < 2.47$, excluding $1.37 < |\eta| < 1.52$

- Calorimeter isolation ($\Delta R < 0.2$) and track isolation ($\Delta R < 0.3$) at the 90% operating point, as defined by the Eiso tool
- Candidate does not pass through a dead region of the calorimeter
- Transverse impact parameter < 2 mm

High p_T is required to select electrons on the stable plateau of the electron trigger efficiency curve. Low values of $|\eta|$ are required so the electron candidates fall inside the fiducial acceptance of the calorimeters. $|\eta|$ between 1.37 and 1.52 represent a dead region in the ATLAS detector in between the barrel and endcap calorimeter systems, and thus is excluded for the purpose of electron reconstruction. During the 2011 run period, there were temporary dead regions in the calorimeter. For the sake of consistent electron performance, electron candidates are rejected if they fall inside one of these regions. The Eiso tool is a multi-variate algorithm which defines the isolation for electron candidates in terms of a number of track and calorimeter quantities [38]. Unlike simple cuts on an isolation variable, this tool provides uniform isolation efficiency across a wide range of p_T and η . The cut on the transverse impact parameter is added to ensure the electron candidate comes from the primary vertex.

5.1.2 Muons

Muons are reconstructed using a combination of the Inner Detector and Muon Spectrometer systems, as described in [39]. To ensure high quality muons, we require muons reconstructed with the Muid algorithm and which pass the ‘tight’ quality flag, as defined by the Muon CP group. There are 4 reconstruction algorithms used by Muid: Muid Standalone, MuGirl, MuTagIMO, and Muid Combined [39]. Muid Standalone starts reconstruction in

the Muon Spectrometer by constructing a track in the Muon Spectrometer and extrapolating back to the primary vertex. By contrast, MuGirl uses an Inner Detector track as a seed for track reconstruction of hits in the Muon Spectrometer, and MuTagIMO associates an Inner Detector track with track segments from the Muon Spectrometer. Muid Combined takes advantage of both sub-detectors by performing a global re-fit to tracks from the Inner Detector and Muon Spectrometer. A ‘tight’ muon from the Muid standpoint must satisfy any of the following [39]:

- Muid Combined
- MuGirl with an extended track in the Muon Spectrometer (at least two MDT+CSC stations OR less than six MDT+CSC holes on track)
- Muid Standalone with $|\eta| > 2.5$ and 3 MDT + CSC stations

The following additional quality cuts are applied to muon candidates:

- $p_T > 20$ GeV
- $|\eta| < 2.5$
- Absolute track isolation ($\Delta R < 0.3$) < 2.5 GeV
- Absolute calorimeter isolation ($\Delta R < 0.2$) < 4.0 GeV
- One b-layer hit (if any are expected)
- Less than 3 missed hits in the silicon
- At least 2 pixel hits + at least 6 silicon hits

- At least 5 TRT hits + outliers, with at most 10% outliers (this requirement is applied for tracks within $|\eta| < 1.9$)
- Transverse impact parameter < 2 mm

As with electrons, the p_T and η thresholds are designed to ensure the muon is within the acceptance of the muon system and Inner Detector and is on a stable portion of the trigger turn-on curve. Hit requirements in the Inner Detector (including one hit in the b-layer) are required to ensure the track used in the muon reconstruction is of good quality.

5.1.3 Jets

Jets are reconstructed by summing topological cells in the calorimeter system using the anti-kt algorithm with a ΔR cone of 0.4 [40]. Calibrations are applied to the raw, measured output from the clusters to correct for the energy deposited in the calorimeter by electrons and photons (termed the ‘EM’ scale). Corrections are applied to remove deposits due to interactions not from the primary collision (pileup).

Additional kinematic cuts are applied to ensure high-quality jets:

- $p_T > 25$ GeV
- $|\eta| < 2.5$
- | jet vertex fraction | > 0.75

where the jet vertex fraction is defined as the fraction of a jet’s tracks that come from the same primary vertex as the jet itself.

In order to identify b -jets, we use the MV1 tagger, a neural network which takes as input the weights of three other b -tagging algorithms: JetFitterCombNN, IP3D, and SV1 [41]. The JetFitter algorithm identifies b -jets by reconstructing the b -quark decay chain by looking at tracks inside the jet. It is useful for differentiating b and c jets, by taking advantage of the kinematic differences in b and c decays. IP3D, by contrast, uses the measured impact parameter of the jet to discriminate b and light jets. The SV1 algorithm is also specialized for the differentiation of b and light jets, and looks to reconstruct a secondary decay vertex. In Figure 19, we present the b -tagging efficiency as a function of the light flavor rejection factor for the JetFitter, IP3D, SV1, and MV1 taggers. As can be seen, the MV1 tagger gives the best light flavor rejection for a given b -tagging efficiency. In this analysis, we define a b -tagged jet as one with a MV1 weight above 0.404219. This corresponds to b -tagging efficiency of approximately 75%, a c -tagging efficiency of approximately 30%, and a light flavor rejection factor of 30.

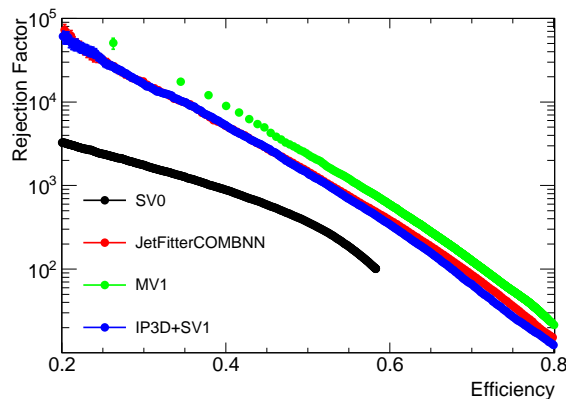


Figure 19: The rejection factors as a function of the tagging efficiency for different b -jet taggers available at ATLAS. As can be seen, the MV1 tagger shows the best rejection power for light jets and is therefore highly recommended to be used.

To prevent double counting of electrons as jets, the jet closest to a reconstructed electron

is removed, if it is within a ΔR of 0.2. Leptons (both e and μ) are removed if there is a jet within a ΔR of 0.4.

5.1.4 E_T^{miss} calculation

The E_T^{miss} is calculated as the momentum imbalance which results when the momenta of all analysis level objects are considered. Specifically, the total E_T^{miss} is defined as:

$$E_T^{\text{miss}} = \sqrt{(E_x^{\text{miss}})^2 + (E_y^{\text{miss}})^2} \quad (4)$$

where

$$E_i^{\text{miss}} = -(E_i^{\text{El}} + E_i^{\text{Mu}} + E_i^{\text{Jet}} + E_i^{\text{SoftJet}} + E_i^{\text{CellOut}}) \quad (5)$$

for $i = x, y$. The electron term is calculated using all electrons satisfying the tight++ criteria, with $p_T > 10$ GeV. The muon term uses all muons from the Muid collection with $|\eta| < 2.7$. The contribution to the E_T^{miss} from jets is broken up into two pieces. Reconstructed jets with $p_T > 20$ GeV calibrated to the EM + JES scale are counted in the E^{Jet} term, while jets with $7 < p_T < 20$ GeV calibrated to only the EM scale are counted in the E^{SoftJet} term. Any topological clusters not associated with these terms are counted in the E^{CellOut} term. Photons and τ candidates are not considered as part of the calculation.

5.2 $t\bar{t}$ candidate event selection cuts

In this section, we describe the event-level cuts used to isolate a sample of events with a $t\bar{t}$ pair candidate. Dilepton $t\bar{t}$ events are generally characterized by two high p_T , isolated

leptons of opposite charge, with significant jet activity and E_T^{miss} . A number of selection criteria are put in place to ensure high quality events with a good primary collision vertex (with no real bias towards the selection of $t\bar{t}$ events). These criteria include:

- Require a good primary vertex with at least 4 high p_T tracks
- Veto events with bad quality jets
- Veto events in which a reconstructed electron and muon result from the same particle
- Veto di-muon events consistent with a cosmic ray
- Veto events with a noise burst in the LAr calorimeter

where ‘bad quality’ jets are defined in [42]. During a portion of the 2011 run period, the LAr calorimeter experienced a series of noise bursts which affected the data taking efficiency. Events in which these noise bursts are present are not useable.

We further require events to pass an appropriate trigger (as described in Chapter 3), with at least one of the leptons matching to the region of interest which fired the trigger. Events with two electrons or two muons are required to pass the relevant single lepton trigger. Events containing one electron and one muon are triggered using a logical ‘OR’ of the above single-lepton triggers.

To select events likely to contain a $t\bar{t}$ pair decaying in the dilepton channel, the following basic selection criteria are applied:

- Two oppositely charged leptons
- Two or more jets

For events where the two leptons are the same flavor (ee or $\mu\mu$), the dominant remaining background come from events containing a neutral boson (e.g. Z/γ , also known as Drell-Yan) which decays directly to electrons or muons. If a real Z is involved, one can re-construct the mass of the Z boson using the kinematics of the two leptons. In general, Drell-Yan events will tend to have low $E_{\text{T}}^{\text{miss}}$, as no neutrinos are produced. We use these two facts to reduce the Drell-Yan background by requiring:

- $E_{\text{T}}^{\text{miss}} > 60 \text{ GeV}$
- $|M_{ll} - 91| > 10 \text{ GeV}$

where M_{ll} is the lepton-lepton invariant mass, and the mass of the Z boson is taken to be 91 GeV. For events with opposite flavor leptons ($e\mu$), the dominant backgrounds are events with two electro-weak bosons (WW , WZ , or ZZ) and events with a Z boson decaying to tau leptons (which then decay to electrons and muons). This background tends to lead to low p_{T} leptons and jets. To isolate the $t\bar{t}$ signal, we require:

- $H_{\text{T}} > 130 \text{ GeV}$

where H_{T} is defined as the scalar sum of the p_{T} of selected leptons and jets in the event.

As described in Chapter 1, two high p_{T} b -jets are produced as part of the decay of the two top quarks and can be used to further purify the $t\bar{t}$ selection. The primary focus of this analysis is events with extra b or c -jets (termed $t\bar{t} + \text{HF}$ events). To preferentially select these events, we define our signal region by requiring 3 or more b -tagged jets. Monte-Carlo indicates that this selection produces a sample of $t\bar{t}$ events with essentially no background. Events in this selection are dominantly those in which both b -jets from the top decay are

tagged and either a light-flavor jet has been mis-tagged or a true, extra b or c -jet has been identified. In Chapter 6, we describe how these two components of the signal region are resolved. A selection of pure $t\bar{t}$ events used in the denominator of the ratio of cross-sections is defined by requiring at least 3 selected jets, at least 2 of which are b -tagged.

b -tagging is used to define three control regions where the analysis framework is tested prior to looking in the signal region. These control regions are those events with exactly 0, 1 and 2 b -tagged jets. As more b -tags are required, the purity of the $t\bar{t}$ selection increases, so each control region is sensitive to different physics processes. To validate our understanding of events containing a fake lepton, we also consider events with like-sign lepton pairs. Details of the study done in these control regions can be found in Chapter 8.

5.3 Definition of the fiducial volume

As described in Chapter 6, these cross-sections are calculated using quantities measured in the data, which are corrected back to the super-set of events which are actually produced. Rather than consider all $t\bar{t} + \text{HF}$ and $t\bar{t} + \text{j}$ events which are produced, we only consider the sub-set of these events which are observable by the ATLAS detector. A cross-section measured in this way is termed a ‘fiducial’ cross-section. The primary advantage to quoting fiducial cross-sections is that the visible acceptance of the ATLAS detector is generally better modeled in the Monte Carlo, and thus systematic modeling uncertainties are generally smaller in this region. In this section, we define selection criteria applied to objects in the Monte Carlo truth record which define the fiducial volume used to calculate the cross-sections for $t\bar{t} + \text{HF}$ and $t\bar{t} + \text{jet}$.

The fiducial volume for the measurement of $\sigma_{\text{fid}}(t\bar{t} + \text{HF})$ is defined by requiring the following:

- 2 true leptons (e, μ) matched to the leptons from the W 's from the $t \rightarrow Wb$ decays
- Lepton $p_{\text{T}} > 25$ GeV for electrons and $p_{\text{T}} > 20$ GeV for muons, and $|\eta| < 2.5$
- 3 or more truth jets with $p_{\text{T}} > 20$ GeV and $|\eta| < 3.0$
- 3 or more truth jets with true heavy flavor content

Stable, truth level leptons are used, and the matching to a W boson is done to exclude leptons from the semi-leptonic decay of b or c -hadrons. Truth jets are constructed from all truth-level particles with a lifetime longer than 10 ps, excluding muons and neutrinos. Particles arising from pileup events are not considered. A jet is identified as 'heavy flavor' if there is a b or c -quark with $p_{\text{T}} > 5$ GeV that satisfies $\Delta\text{R}(\text{j},\text{q}) < 0.25$.

The fiducial volume for the measurement of $\sigma_{\text{fid}}(t\bar{t} + \text{j})$ is similarly defined:

- 2 true leptons (e, μ) matched to the leptons from the W 's from the $t \rightarrow Wb$ decays
- Lepton $p_{\text{T}} > 25$ GeV for electrons and $p_{\text{T}} > 20$ GeV for muons, and $|\eta| < 2.5$
- 3 or more truth jets with $p_{\text{T}} > 20$ GeV and $|\eta| < 3.0$
- 2 or more truth jets with true heavy flavor content

In Table 2, the reconstruction efficiency for events in each fiducial volume is presented. This efficiency is defined as the fraction of events in the fiducial volume that pass each reconstruction-level cut.

Selection cut	Yield of $t\bar{t}$ + HF events	Yield of $t\bar{t}$ + j events
No cuts	643.5	15852.7
Trigger, other minimal event cuts	607.7	15038.6
Two reconstructed leptons	290.0	7580.9
Remaining event cuts	170.3	2827.3
Tagging requirements	40.8	1686.6
Final efficiency	0.063 ± 0.006 (stat)	0.106 ± 0.001 (stat)

Table 2: Expected event yields, and the final reconstruction efficiency for the two fiducial regions ($t\bar{t}$ + HF and $t\bar{t}$ + j). The yields are calculated assuming 4.7 fb^{-1} of integrated luminosity. The efficiency is defined as the ratio of reconstructed, fiducial events to generated, fiducial events for the two processes: $t\bar{t}$ + HF, and $t\bar{t}$ + j. We require three reconstructed b -tags for $t\bar{t}$ + HF and two reconstructed b -tags for $t\bar{t}$ + j. Only statistical uncertainties are included.

6 Analysis method

This analysis is designed to measure the fraction of $t\bar{t}$ dilepton events which contain extra b or c -quark jets (i.e. beyond the b -jets from the $t \rightarrow Wb$ decay). To do this, we measure the production cross-section for dilepton $t\bar{t}$ events with at least three jets ($\sigma(t\bar{t} + \text{j})$), and the cross-section for the subset of these events which contain at least one additional HF jet ($\sigma(t\bar{t} + \text{HF})$). To reduce the overall systematic uncertainty, we quote cross-sections which are corrected back to a fiducial region corresponding to the visible ATLAS acceptance (as described in Section 5.3), rather than to the entire allowed kinematic phase space. As such, the measurements described in this section are for the so-called fiducial cross-sections for $t\bar{t} + \text{HF}$ ($\sigma_{\text{fid}}(t\bar{t} + \text{HF})$) and $t\bar{t} + \text{jet}$ ($\sigma_{\text{fid}}(t\bar{t} + \text{j})$) production. To further reduce the total systematic uncertainty, the primary result of this thesis is the ratio of fiducial cross-sections (R_{HF}).

The methods used to estimate the signal and background processes for each cross-section are described in Section 6.1. Special attention is given to the background due to fake leptons in Section 6.2. In Section 6.3, the fitting method used to extract the flavor composition of b -tagged jets in the $t\bar{t} + \text{HF}$ signal region is described in detail. Section 6.4 details how each fiducial cross-section is measured.

6.1 Signal & background estimate

In this section, we describe how the signal and background rates are measured for $\sigma_{\text{fid}}(t\bar{t} + \text{HF})$ and $\sigma_{\text{fid}}(t\bar{t} + \text{j})$. Generally, the signal for this analysis is $t\bar{t}$ events in the dilepton decay mode: $t\bar{t} \rightarrow W^+b W^- \bar{b} \rightarrow l^+ \nu b l^- \bar{\nu} \bar{b}$. Selected events are defined by the presence of

leptons and b -jets, and as such, we differentiate signal and background events based on the source of these objects.

It is common practice at ATLAS to define a ‘fake’ lepton as a hadron which is improperly reconstructed as a lepton, or an actual lepton which comes from a ‘non-signal’ source. Signal sources for this analysis are taken to be the leptonic decay of EW bosons: $Z \rightarrow ll$ or $W \rightarrow l\nu$. Common sources of non-signal leptons are converted photons (in the case of electrons) and the semi-leptonic decay of heavy-flavor hadrons. In this thesis, we adopt this terminology, and differentiate fake leptons based on their source: heavy flavor (HF), light flavor (LF), or conversions (for photons). Identified b -jets in this analysis come from four sources: b -jets from the $t \rightarrow Wb$ decay, additional b -jets, c -jets, and light-flavor (LF) jets. To measure $t\bar{t} + \text{HF}$, care must be given to correctly identify the source of identified b -jets.

For the measurement of $t\bar{t} + \text{jet}$ production, we require two reconstructed leptons, at least three total jets, and at least two b -tagged jets. For consistency with the measurement of $t\bar{t} + \text{HF}$, we require that both of the b -tagged jets come from real HF. Monte Carlo is used to remove events with one or more LF b -tags from the yield observed in the data. $t\bar{t}$ events are modeled using Monte Carlo simulation produced with the ALPGEN generator interfaced with HERWIG parton showering, as described in Chapter 4. The background due to $Z + \text{jets}$, single top, and di-boson (WW , WZ , ZZ) events with no fake leptons are expected to be small and modeled with the Monte Carlo simulation. We leave a discussion of the fake lepton background to the next section.

For the measurement of $t\bar{t} + \text{HF}$ production, we require two reconstructed leptons, and at least three b -tagged jets. The signal is defined by events containing any c -jets or b -jets not from the decay of the top quark. The background from non- $t\bar{t}$ events with no fake leptons is

expected to be small and is estimated directly from the Monte Carlo. The background from fake leptons is estimated using the same method as for $t\bar{t}$ + jet events. Due to the large rate of $t\bar{t}$ + LF jet, there is a sizable background due to $t\bar{t}$ events with b -tagged jets coming from LF. This background is measured by performing a fit, as described in Section 6.3.

6.2 Fake lepton estimate

An important background to events containing leptons are those events which contain at least one fake lepton. Traditionally, this background is not well-modeled by the Monte Carlo, so data-driven methods are often required. The signal for this analysis contains a pair of oppositely-signed (OS) leptons. We estimate the fake lepton background for a given kinematic selection using the yield of events containing a same-sign (SS) pair of leptons, but otherwise passing identical selection criteria. To correct for charge correlations between leptons in an event with a fake, we scale the SS yield by the ratio of OS/SS fakes, as measured in the Monte Carlo. Due to limited statistics in the Monte Carlo, the OS/SS ratio is measured using a looser lepton selection. Details on this loose selection are given in Section 8.1.

The motivation for this approach is that the Monte Carlo indicates that the yield for SS events passing the nominal $t\bar{t}$ selection with at least one b -tagged jet is dominated by events with a fake lepton. As such, we measure the fake yield directly in the data using the SS yield for a given kinematic selection. If the SS yield contains a non-fake component in the Monte Carlo, this is subtracted from the yield observed in the data.

Depending on the physics process involved, there may or may not be charge correlation

between the leptons in events with at least one fake. To account for this correlation, we use the Monte Carlo to measure the OS/SS ratio for events with a fake lepton, and re-scale the SS yield in the data to obtain the fake yield in the OS region.

To understand the charge correlation in fake events, we need to consider the specific ways in which a fake event can occur. Though it is possible for a single event to have two fake leptons, the Monte Carlo indicates that the majority of fake events contain only one. For the dilepton $t\bar{t}$ final state, the main sources of single fake events are $W + \text{jet}$ events and $t\bar{t}$ events in which only one W decays leptonically. In $W + \text{jet}$ events, the fake is usually due to radiated jets, and thus there is little correlation between the charge of the leptons. For semi-leptonic $t\bar{t}$ events, there are two scenarios to consider. In the first, the fake is due to one of the b -quarks, or additional background radiation. Since the two b 's have opposite sign and the fake is equally likely to come from either, there is little correlation between the charges of the leptons. As with $W + \text{jet}$ events, fakes from radiated jets show little charge correlation. Fakes in semi-leptonic $t\bar{t}$ events can also be produced when the W decays to hadrons, which then fake a lepton. The charge of the lepton produced in this way is strongly correlated with the charge of the W , and thus with the charge of the real lepton in the event. This leads to a correlation between the charge of the two leptons, as indicated in Table 3.

As discussed in detail in Chapter 7, we assess a systematic uncertainty on the fake lepton estimate by re-scaling the SS yield by an OS/SS ratio assuming only LF fakes. Since the SS yield comes from the data, the largest potential bias in our estimate comes from mis-measurement of the OS/SS ratio. Based on the above discussion, it is apparent that the OS/SS ratio could be biased if the rate of different kinds of fake process are mis-modeled. Fakes from heavy-flavor jets (and conversions, for electrons) are approximately charge sym-

Channel	OS/SS ratio for W fakes	OS/SS ratio for non- W fakes
ee	7.6 ± 2.9	2.6 ± 0.7
$\mu\mu$	4.5 ± 2.9	1.5 ± 0.4
$e\mu$	3.8 ± 0.9	1.4 ± 0.1

Table 3: Comparison of the OS/SS ratio for events with a fake lepton coming from a light flavor jet (predominantly mis-identified hadrons). We separately examine events where the fake lepton matches to a W boson and events where the fake lepton does not match to a W .

metric, leading to an OS/SS near 1.0. Light flavor fakes (predominantly from mis-identified hadrons in semi-leptonic $t\bar{t}$ events) by contrast give a larger OS/SS ratio. To be conservative, we take the largest possible variation in the OS/SS ratio, which happens when only light flavor fakes are assumed.

In Table 4, the OS/SS ratio for events with at least one fake lepton is presented as a function of the b -tag multiplicity, separately for each dilepton channel. Contributions from each kind of fake lepton are given as reference. In Figure 20, we perform a fit to the OS/SS ratio as a function of b -tagged jet multiplicity, and extrapolate out to a multiplicity of three (where the signal region is located). Minimal variation is observed as a function of b -tag multiplicity, so we calculate the OS/SS ratio by summing over bins of b -tag multiplicity.

Channel	Tag multiplicity	R(all)	R(HF fakes)	R(LF fakes)	R(conversion fakes)
ee	0	1.38 ± 0.17	1.11 ± 0.21	3.02 ± 0.95	1.05 ± 0.19
ee	1	1.15 ± 0.12	1.09 ± 0.17	2.87 ± 0.8	0.95 ± 0.15
ee	2	1.49 ± 0.21	1.19 ± 0.48	4.3 ± 1.83	1.17 ± 0.2
$\mu\mu$	0	1.35 ± 0.14	1.3 ± 0.14	1.78 ± 0.86	–
$\mu\mu$	1	1.01 ± 0.07	0.98 ± 0.07	1.69 ± 0.51	–
$\mu\mu$	2	1.2 ± 0.23	1.12 ± 0.22	1.84 ± 1.09	–
$e\mu$	0	1.18 ± 0.05	1.13 ± 0.06	1.64 ± 0.2	1.04 ± 0.09
$e\mu$	1	1.06 ± 0.04	1.02 ± 0.04	1.45 ± 0.22	1.03 ± 0.1
$e\mu$	2	1.4 ± 0.09	1.35 ± 0.15	2.75 ± 0.47	1.09 ± 0.11

Table 4: OS/SS ratio for fake events using loose leptons, for three dilepton channels and tag multiplicity bins. Errors quoted are statistical. To understand potential systematic variations in R, we show R for different kinds of fakes: heavy and light flavor jets, and conversions. The nominal OS/SS ratio used is 1.32 ± 0.10 (stat.) ± 1.82 (sys.) for ee , 1.15 ± 0.07 (stat.) ± 0.68 (sys.) for $\mu\mu$, and 1.16 ± 0.03 (stat.) ± 0.54 (sys.) for $e\mu$. The systematic uncertainty is computed by comparing the nominal OS/SS ratio with that obtained using only LF fakes.

Channel	Tag multiplicity	R(all)	R(HF fakes)	R(LF fakes)	R(conversion fakes)
ee	0	1.61 ± 0.61	–	–	1.26 ± 0.51
ee	1	1.6 ± 0.54	–	0.47 ± 0.67	1.58 ± 0.57
ee	2	3.99 ± 2.01	–	–	2.64 ± 1.24
$\mu\mu$	0	1.58 ± 0.64	1.12 ± 0.51	3.83 ± 4.14	–
$\mu\mu$	1	0.97 ± 0.29	0.71 ± 0.24	4.03 ± 3.61	–
$\mu\mu$	2	2.6 ± 1.59	1.6 ± 1.17	8.01 ± 7.18	–
$e\mu$	0	1.15 ± 0.21	1.82 ± 0.58	1.13 ± 0.62	0.99 ± 0.24
$e\mu$	1	1.36 ± 0.22	1.32 ± 0.28	6.06 ± 3.7	0.96 ± 0.23
$e\mu$	2	1.57 ± 0.3	2.57 ± 1.22	–	1.07 ± 0.24

Table 5: OS/SS ratio for fake events using tight, for three dilepton channels and tag multiplicity bins. Errors quoted are statistical. Within statistical uncertainties, there is no observed bias in the OS/SS ratio caused by the tighter selection.

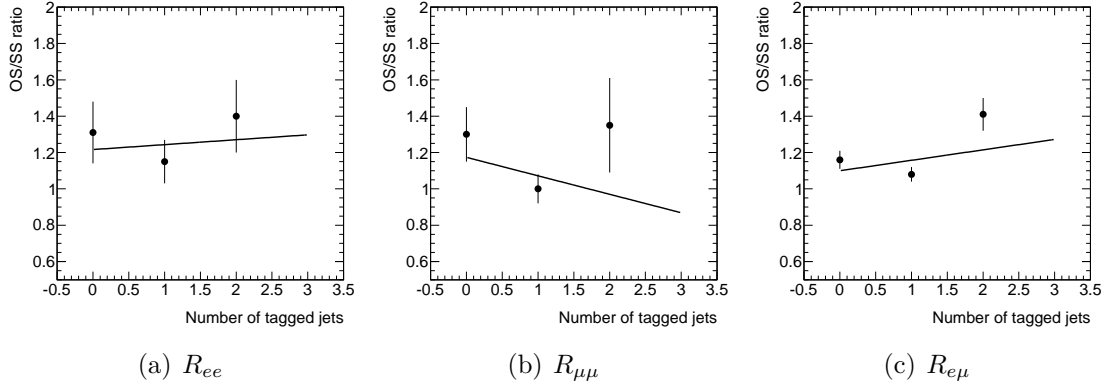


Figure 20: The OS/SS ratio in ee (a), $\mu\mu$ (b), and $e\mu$ (c) events, as a function of tagged jet multiplicity. A linear fit is performed to extrapolate to events with 3 tagged jets. The fitted slope is 0.03 ± 0.13 for ee events, -0.10 ± 0.13 for $\mu\mu$ events, and 0.06 ± 0.05 for $e\mu$ events.

It is possible that fakes satisfying the looser lepton selection behave differently than fakes using the tighter selection used in the rest of the analysis. To examine this, we re-compute the OS/SS ratio using the full tight selection, as shown in Table 5. Within the sizable statistical uncertainty on the latter, the two estimates are in agreement.

6.3 Fitting method

To extract the fiducial cross-section for $t\bar{t} + \text{HF}$ production, we perform a binned, maximum-likelihood fit to all b -tagged jets in dilepton $t\bar{t}$ candidate events with at least three b -tagged jets. Generally, there are five kinds of b -tagged jets in this selection:

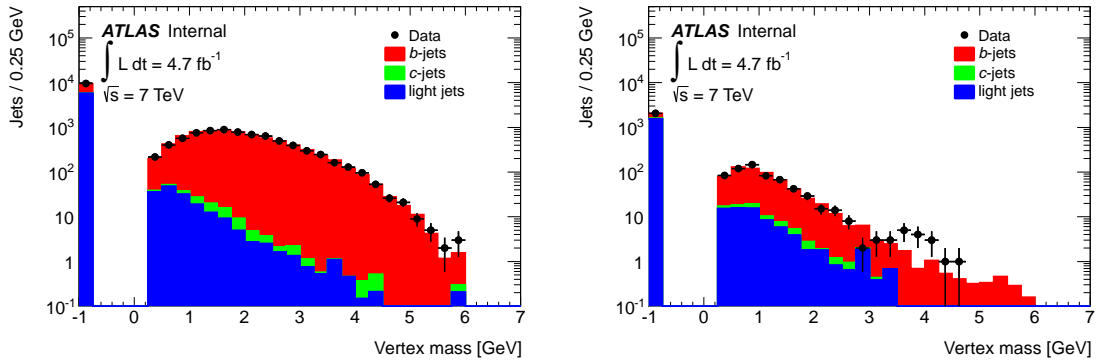
- b -jets from the $t \rightarrow Wb$ decay
- Additional b -jets
- c -jets
- Light flavor jets

- Background jets

where background jets are any jet in a non- $t\bar{t}$ or fake event. If this analysis was performed using semi-leptonic $t\bar{t}$ events, a sixth category would be needed: c -jets from $W \rightarrow c\bar{s}$. One of the primary reasons for choosing to perform this analysis in the dilepton channel is to avoid this additional complication in determining the flavor composition.

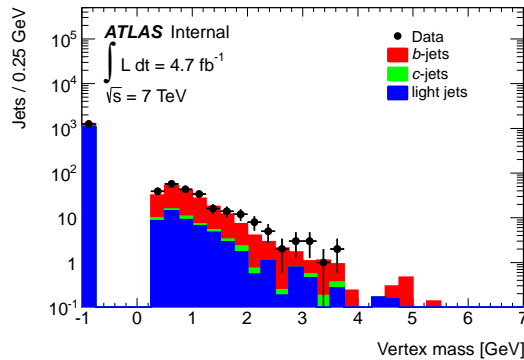
To differentiate these five categories of jet, we employ two discriminating variables: vertex mass, and p_T . The first and more powerful discriminating variable is the vertex mass of the jet. The vertex mass correlates to the flavor of the quark species which produces the vertex: the mass will be highest for b -jets, lowest for mis-identified light jets, and in between for c -jets. Jet p_T is useful for differentiating additional b -jets from b -jets from the top decay. The vertex mass is also slightly correlated with jet p_T , so using it as a second discriminating variable means differences in the p_T spectrum between data and Monte Carlo will not significantly bias our result.

As described in Chapter 5, b -tagged jets in this analysis are required to have an MV1 weight above the 75% operating point. Our fit takes advantage of the 60% and 70% operating points as well. Specifically, the fit is performed simultaneously in three bins of MV1 weight: the first bin (termed ‘High b -purity’) requires jets with weight above the 60% operating point, the second bin (termed ‘Medium b -purity’) requires a jet have weight below the 60% operating point but above the 70% operating point, and the final bin (termed ‘Low b -purity’) requires a weight above the 75% operating point but below the 70% operating point. The advantage to this approach is that each bin contains a different flavor composition: the first bin contains the highest fraction of b -jets, the second bin contains a higher fraction of c



(a) High b -purity tagged jets

(b) Medium b -purity tagged jets



(c) Low b -purity tagged jets

Figure 21: Vertex mass distributions for b , c , and light flavor jets in events, passing the nominal $t\bar{t}$ selection, with at least one b -tagged jet. The first selection (termed ‘High b -purity’) requires a jet to have a b -tag weight above the 60% operating point, and contains the highest fraction of true b -jets. The second selection (‘Medium b -purity’) requires a jet to fail the 60% operating point but pass the 70% operating point. A higher c fraction is observed in this bin. The final selection (‘Low b -purity’) requires the jet to fail the 70% operating point but pass the 75% operating point. This bin contains the largest fraction of light jets.

and light jets, and the last bin is dominated by light jets. This leads to a total of 15 (5 flavors of jet \times 3 bins of MV1 weight) independent parameters. The shape of the vertex mass distribution for b , c , and light jets in each of the three b -purity bins is compared in Figure 21.

The fit is performed using the ROOT module RooFit [43], version 3.17. For each parameter, a binned, two-dimensional probability density function (termed a ‘template’) is defined. Three bins each of vertex mass and p_T are used, for a total of 9 bins per template. Jet p_T is

binned in bins of 30 GeV from 25 to 115, with overflows included in the last bin. The first bin of vertex mass contains jets without a reconstructed vertex. The second bin of vertex mass contains jets with a vertex mass below 2 GeV, while the final vertex mass bin contains jets with mass above 2 GeV.

Templates are filled using a combination of data and Monte Carlo. Monte Carlo predicts that 97% of tagged jets in $t\bar{t}$ events with exactly two b -tagged jets come from real b -jets from the $t \rightarrow Wb$ decay. To leverage this, we fill our template for b -jets from top using this selection in the data. A 3% subtraction derived in the Monte Carlo is applied to the data to remove the expected background for jets not from the top decay. It is difficult to derive pure templates for the other types of jets used in the fit from the data, so we take their shape directly from the Monte Carlo in events with three or more b -tagged jets.

For each of the three MV1 distributions, we calculate the Poisson probability P_{ij} , for the i^{th} vertex mass bin and j^{th} p_T bin:

$$P_{ij} = P(N_{ij}^{fit}, N_{ij}^{data})$$

where P is the Poisson probability function for observing N_{ij}^{data} , given N_{ij}^{fit} in that bin. N_{ij}^{fit} is the sum of the fitted number of jets for each type:

$$N_{ij}^{fit} = N_{ij}^{bt} + N_{ij}^b + N_{ij}^c + N_{ij}^{lf} + N_{ij}^{bkg}$$

where N^{bt} is the number of b -jets from the top decay, N^b is the number of additional b -jets, N^c is the number of c -jets, N^{lf} is the number of light flavor jets, and N^{bkg} is the number of background jets. Schematically, one can think of the fit as a weighted sum of templates,

where each coefficient is allowed to float. For b -jets from the top decay:

$$N^{bt} = n_1^{bt} \cdot p_1^{bt} + n_2^{bt} \cdot p_2^{bt} + n_3^{bt} \cdot p_3^{bt}$$

where p_m^{bt} is the template for b -jets from top in the m^{th} bin of MV1 weight, and n_m^{bt} is the relevant coefficient.

A number of simplifying assumptions are used to reduce the number of independent fit parameters from 15 to 2. Most importantly, we use the MV1 calibration to relate the number of jets of each flavor across each MV1 bin. By definition, we can relate the number of b -tagged jets passing a given selection (N^{tag}) to the total number of pre-tagged jets ($N^{\text{pre-tag}}$) by the efficiency (ϵ) of the selection:

$$N^{\text{tag}} = N^{\text{pre-tag}} \cdot \epsilon$$

The calibration provides the efficiency for each flavor of jet (b , c , and light) at each operating point. Thus for a given flavor, we can relate the number of jets selected at each operating point to the number of pre-tagged jets using the efficiency of that operating point:

$$\frac{N_1}{\epsilon_1} = \frac{N_2}{\epsilon_2} = \frac{N_3}{\epsilon_3} = N_{\text{pre-tag}} \quad (6)$$

where 1, 2, and 3 are taken to be the three b -tagging selections.

As described in Chapter 4, the calibration is implemented via scale factors applied to the Monte Carlo. Nominally, scale factors are defined only for inclusive cuts on the MV1 weight (i.e. for all jets above a certain operating point). In this context, the calibration provides a

scale factor, and the tagging efficiency in the Monte Carlo. In order to properly select jets using exclusive bins of MV1 weight, we need to re-define the scale factors. For instance, the scale factor for the medium b -purity bin must take into account the efficiency for the jet to fail the high b -purity selection. As described first in [44], we define scale factors for exclusive cuts on the MV1 weight in terms of the inclusive scale factors and efficiencies according to:

$$SF_{AB} = \frac{\epsilon_A^{data} - \epsilon_B^{data}}{\epsilon_A^{MC} - \epsilon_B^{MC}} = \frac{\epsilon_A^{MC} \cdot SF_A - \epsilon_B^{MC} \cdot SF_B}{\epsilon_A^{MC} - \epsilon_B^{MC}} \quad (7)$$

where SF_A is the inclusive scale factor for operating point A, and ϵ_A is the tagging efficiency. This reduces the number of independent fit parameters from 15 to 5 (one for each flavor of jet).

We further reduce the number of independent parameters in the fit by appealing to some physical insight. First, the background contribution (i.e. from non-dilepton- $t\bar{t}$ events, or events with a fake lepton) is negligible, so we fix the normalization for this template to the value predicted by the Monte Carlo. Next, we know there is a large contribution of b -jets from the top decay. For every $t\bar{t}$ event, we assume that two of the b -tagged jets are from the top decay, and we fix the normalization of the template for b -jets from top accordingly. Together, this reduces the number of independent parameters in the fit to three (the number of additional b -, c -, and light jets). The final piece of insight is that we fix the sum of the fit results to equal the total number of b -tagged jets observed in the data:

$$N^{obs} = N^b + N^c + N^{light} + N^{bt} + N^{bkg}$$

This allows us to reduce the number of independent parameters by one, and means that we fit for the fraction of jets of a given flavor. We choose to use the fraction of additional b - and light jets as our fit parameters. As described in Chapter 8, the reason for this is that the fit is very good at differentiating light jets from b 's and c 's, but it is less successful at differentiating b 's from c 's. Using the fraction of light jets, we can measure the total HF production. The fraction of additional b -jets is used as part of the systematic uncertainty calculation.

6.4 Cross-section calculation

In this section, we describe how the fiducial cross-sections $\sigma_{\text{fid}}(t\bar{t} + \text{HF})$ and $\sigma_{\text{fid}}(t\bar{t} + \text{j})$ are calculated. The generic formula for deriving a cross-section is:

$$\sigma = \frac{N}{\int \mathcal{L} dt \cdot \epsilon}$$

where N is some number measured in the data, $\int \mathcal{L} dt$ is the total integrated luminosity of the data sample, and ϵ is a correction term used to convert the measured number from data to the desired number of generated events. The integrated luminosity used in this analysis is 4.7 fb^{-1} .

All events are required to have two leptons, and at least three jets. For the measurement of $t\bar{t} + \text{HF}$ events, at least three b -tagged jets are required, and it is assumed that two of these b -tagged jets are from the $t \rightarrow Wb$ decay. N is the number of additional HF jets (as returned by the fit), and ϵ corrects the number of HF jets to the number of $t\bar{t} + \text{HF}$ events in the fiducial volume. Since N assumes all b -tagged jets are from HF, we make the same

requirement in the calculation of ϵ . Specifically, ϵ is defined as the ratio of the number of reconstructed events passing the selection outlined in Section 5.2 to the number of fiducial events (at truth level in the Monte Carlo) passing the selection outlined in Section 5.3:

$$\epsilon_{HF} = \frac{2 \text{ identified leptons \&\& 3 or more } b\text{-tagged HF jets}}{2 \text{ fiducial leptons \&\& 3 or more fiducial HF jets}}$$

where events in the numerator are filled using reconstructed events, and events in the denominator are entirely taken from the truth record. Using the Monte Carlo, we find the value for ϵ for $\sigma_{\text{fid}}(t\bar{t} + \text{HF})$ to be 0.070 ± 0.004 (stat).

For the measurement of $t\bar{t} + \text{jet}$ events, at least two b -tagged jets are required. N is the number of events with at least two b -tagged jets, and ϵ corrects to the number of events in the $t\bar{t} + \text{jet}$ fiducial volume. To be consistent with the selection applied to $t\bar{t} + \text{HF}$, all b -tags are required to be from real HF. The Monte Carlo is used to remove events in the data which have light flavor b -tags. Following the pattern for ϵ for the measurement of $\sigma_{\text{fid}}(t\bar{t} + \text{HF})$, we define ϵ for the measurement of $\sigma_{\text{fid}}(t\bar{t} + \text{j})$ as the ratio of reconstructed to fiducial events:

$$\epsilon_j = \frac{2 \text{ identified leptons \&\& 2 or more } b\text{-tagged HF jets}}{2 \text{ fiducial leptons \&\& 2 or more fiducial HF jets}}$$

In both the numerator and the denominator, at least three jets are required, but only 2 are required to contain HF. Using the Monte Carlo, we find ϵ_j to be 0.108 ± 0.001 (stat).

As will be discussed more in Section 7, the reconstruction efficiency for $t\bar{t} + b$ events is very different from $t\bar{t} + c$ events. As such, the value for ϵ_{HF} , used in the calculation of $\sigma_{\text{fid}}(t\bar{t} + \text{HF})$, depends on the ratio of $t\bar{t} + b$ events to all $t\bar{t} + \text{HF}$ events. The value for ϵ_{HF} quoted

here assumes the $t\bar{t} + b$ to $t\bar{t} + \text{HF}$ ratio taken directly from the Monte Carlo.

7 Systematics

In this chapter, the systematic uncertainties that affect the analysis are outlined. Generally, there are two ways in which a given source of systematic uncertainty can affect the final calculation of the two fiducial cross-sections. First, a systematic may affect the shape of the vertex mass templates used in the fit to extract the flavor composition of extra b -tagged jets in the signal region. Systematic uncertainties of this sort will only affect the calculation of $\sigma_{\text{fid}}(t\bar{t} + \text{HF})$. Second, a systematic may affect the reconstruction efficiency of physics objects, and thus the acceptance factor used to correct from the measured quantities to the final fiducial cross-sections. These systematic uncertainties will generally affect both the calculation of $\sigma_{\text{fid}}(t\bar{t} + \text{HF})$ and $\sigma_{\text{fid}}(t\bar{t} + \text{j})$.

In Section 7.1, we describe the uncertainties related to the modeling of lepton identification. As the analysis is based around an understanding of jets, two primary sources of systematic uncertainty related to jet identification and reconstruction are treated separately. We discuss the reconstruction of jets in Section 7.2 while a b -tagging efficiency is taken up in Section 7.3. Section 7.4 describes the systematic evaluated on the $E_{\text{T}}^{\text{miss}}$ calculation. Another major source of uncertainty in the analysis comes from the Monte Carlo used to simulate $t\bar{t}$ events. The details of the uncertainty from this source are addressed in Section 7.5. A minor systematic on the RSS method is discussed in Section 7.6. All of these uncertainties affect both the fit and acceptance calculation.

As described in Chapter 6, a number of assumptions are made when constructing the fit used to extract the cross-section for $t\bar{t} + \text{HF}$. We assess a number of systematics on these assumptions in Section 7.7. By definition, these uncertainties affect only the fit.

Finally, due to a difference in b -tagging efficiencies, the acceptance calculation is sensitive to the fraction of events for which the extra HF comes from a b -quark, as opposed to a c -quark. This fraction is termed $f_{b/HF}$. We discuss a systematic evaluated on the value of $f_{b/HF}$ from the Monte Carlo using information from our fit.

7.1 Lepton identification

As described in Section 4.3, ATLAS-standard scale factors are applied to the Monte Carlo to account for the modeling of lepton reconstruction and trigger efficiencies. For both electrons and muons, the scale factors and their associated uncertainties are evaluated using the tag-and-probe method in $Z \rightarrow ll$ events [37], [45], [46]. These uncertainties are reported as an ‘up’ and ‘down’ variation on the respective scale factor. To be conservative, the scale factors for trigger and reconstruction efficiency are varied together. For a dilepton event, where each lepton has scale factors s^{id} and s^{trig} for ID and trigger efficiency respectively, we evaluate the product of scale factors as:

$$w = s_1^{\text{id}} \cdot s_2^{\text{id}} \cdot s_1^{\text{trig}} \cdot s_2^{\text{trig}} \quad (8)$$

For an event with two leptons of the same flavor, the Monte Carlo is re-weighted using the product of scale factors with their given variations:

$$w = s_1^{\text{id up/down}} \cdot s_2^{\text{id up/down}} \cdot s_1^{\text{trig up/down}} \cdot s_2^{\text{trig up/down}} \quad (9)$$

For an event with leptons of different flavor, the scale factors are varied independently:

$$w = s_1^{\text{id}} \cdot s_2^{\text{id up/down}} \cdot s_1^{\text{trig}} \cdot s_2^{\text{trig up/down}} \quad (10)$$

After the re-weighting, both the fit and acceptance calculations are re-done. The final systematic is taken as the average of the deviations, as measured from the baseline, of R_{HF} .

7.2 Jet properties

The calibration of the jet energy scale is measured within ATLAS using a large sample of inclusive QCD events simulated in PYTHIA [47]. A re-scaling is applied to all jets in the Monte Carlo, to compliment the calibration applied to jets in the data. The uncertainty on this calibration is derived by performing a multi-dimensional fit in various control regions, where each component of the jet energy scale uncertainty is treated as a nuisance parameter for the fit [48], [49]. A separate calculation is done for the energy scale for b -jets.

The jet energy resolution is measured using the di-jet balance and bi-sector techniques, as described in [50]. By default, no scaling is applied, but uncertainties are used to calculate a systematic.

Systematic shifts in the jet energy scale and resolution can affect the number of reconstructed jets, and thus the number of reconstructed leptons (as there is a minimum ΔR requirement between reconstructed leptons and jets, as described in Chapter 5). For the jet energy scale measurement, ‘up’ and ‘down’ variations are defined. The jet energy resolution is assigned a single symmetric error, which is used to smear the p_T of reconstructed jets assuming a Gaussian smearing factor centered at 1.0. In both cases, the Monte Carlo is re-run and the whole calculation of R_{HF} is repeated. For the jet energy scale, the final systematic

is taken as half the deviation given by the ‘up’ and ‘down’ variations. For the jet energy resolution, the final systematic is simply the deviation from the baseline result.

Another systematic associated with jet reconstruction comes from the application of the JVF cut used to reject jets coming from pileup events [51]. Scale factors are applied to the Monte Carlo to account for the difference in observed efficiency for this cut between data and Monte Carlo. Uncertainties on this scale factor are derived in data by the JetTauEtmis group using a tag-and-probe analysis. As described in Chapter 4, scale factors for this cut are defined separately for four cases:

- Hard-scatter jet, which passes the JVF cut (ss)
- Hard-scatter jet, which fails the JVF cut (sb)
- Pileup jet, which passes the JVF cut (bs)
- Pileup jet, which fails the JVF cut (bb)

A single variation is defined for each kind of scale factor. Using kinematic information for all jets in an event which pass all selection cuts except the JVF cut, a weight is derived using a standard ATLAS software package. Variations on this weight are defined in terms of the four types of scale factor and grouped into two components: one for hard-scatter jets and one for pileup jets. The total variation for hard-scatter jets is defined in terms of the scale factor (s) and associated error (σ):

$$\sigma_s = \frac{\sigma_{ss} * \sigma_{sb} - s_{ss} * s_{sb}}{s_{ss} * s_{sb}} \quad (11)$$

Similarly, for pileup jets, the total variation is defined as:

$$\sigma_b = \frac{\sigma_{bs} * \sigma_{bb} - s_{bs} * s_{bb}}{s_{bs} * s_{bb}} \quad (12)$$

These uncertainties are added in quadrature, and the event weight is modified by adding (and subtracting) this total uncertainty. Using the re-weighted Monte Carlo, the analysis is re-run, and the total systematic is taken as the average deviation from the baseline after applying the ‘up’ and ‘down’ variations.

7.3 Jet tagging efficiency

As part of the calibration for the MV1 b -tagger, ATLAS-standard assesses a set of scale factors and uncertainties for jets of three flavors: b , c , and light-flavor. Separate scale factors and uncertainties are derived for each operating point. When considering a single operating point, an inefficiency scale factor is defined and applied to jets failing the b -tagging criteria. As described in Section 4.3, the product of scale factors for all selected jets in the event is used to re-weight each event in the Monte Carlo.

Systematic uncertainties are assessed separately for b , c , and light jets by comparing data and Monte Carlo in a number of control regions. The uncertainties for b and light jets are determined using a $t\bar{t}$ selection, while uncertainties for c -jets are determined by looking at D^* decays [41]. The three selections are statistically independent, so systematic variations are applied separately for each flavor of jet.

When selecting events in this analysis for control region studies, the nominal scale factors are taken directly from the calibration. Systematics are assessed by changing each scale factor up or down by its associated error. By definition, the b -tagging efficiency scale factor is 100%

anti-correlated to the b -tagging inefficiency scale factor. Separate calculations are done for b , c , and light-flavor jets. The final systematic is calculated as the average deviation in the re-weighted yield after ‘up’ and ‘down’ variations are applied.

For the measurement of R_{HF} , where jets are selected in exclusive ranges of the MV1 weight, it is necessary to evaluate new scale factors, as described in Chapter 6. The scale factor for jets b -tagged between two operating points (A and B) is defined as:

$$SF_{AB} = \frac{\epsilon_A^{data} - \epsilon_B^{data}}{\epsilon_A^{MC} - \epsilon_B^{MC}} = \frac{\epsilon_A^{MC} \cdot SF_A - \epsilon_B^{data} \cdot SF_B}{\epsilon_A^{MC} - \epsilon_B^{MC}} \quad (13)$$

where the ϵ 's are the b -tagging efficiencies, and the SF 's are the nominal scale factors at the respective operating points. The systematic variation on these scale factors are similarly defined in terms of the nominal ‘up’ and ‘down’ variations provided by the CP groups. Specifically, for a systematic associated with the variation of the efficiency at operating point A , the modified scale factor would be:

$$SF_{AB}^{A,+/-} = \frac{\epsilon_A^{MC,+/-} \cdot SF_A^{+/-} - \epsilon_B^{MC} \cdot SF_B}{\epsilon_A^{MC,+/-} - \epsilon_B^{MC}} \quad (14)$$

It is assumed that the systematic variation in the efficiency is 100% correlated with the systematic variation on the scale factor.

Templates in the fit are populated on a jet-by-jet basis, and by default weighted by the total event weight (i.e. the product of b -tagging scale factors for all jets in the event). To avoid over-counting the effect of the b -tagging systematic, the weight for each jet is defined by considering the nominal event weight with only the scale factor for the jet itself varied by the prescribed systematic. Separate estimates are made for b , c , and light jets in four

ranges of MV1 weight: jets passing the tight, medium, and loose b -tagging selections, and those failing the loose selection. The final systematic is taken as the average of the ‘up’ and ‘down’ variations, summed in quadrature over flavor and b -tagging selection.

7.4 Missing E_T calculation

Corrections to the E_T^{miss} are made separately to each term, as described in Chapter 5. Since our analysis is only sensitive to E_T^{miss} as it affects the event selection for the fit and acceptance calculation, it is sufficient to only evaluate the largest uncertainty on the E_T^{miss} , which comes from the term related to cells not associated with a reconstructed physics object (i.e. the CellOut term). The JetTauEtmiss group has defined corrections to the CellOut term, which are evaluated for each event by considering the momentum of all other objects in the event. To evaluate the systematic, these ‘up’ and ‘down’ variations are applied to the E_T^{miss} calculation, and the new, corrected value used in the event selection. The final uncertainty is taken as the average difference when these variations are applied.

7.5 Top quark event generation and showering

Our analysis is sensitive to the details of the top quark decay process, as it is simulated in the Monte Carlo. The generated properties of the top quark decay process can lead to a bias in the kinematics of b -quark produced in the top decay, or in the kinematics of the W boson. Similarly, the properties of the parton shower model used in the fragmentation process can have a dramatic effect on the final value of R_{HF} , as extra HF jets can be created directly during this step. As described in Chapter 4, the baseline Monte Carlo sample used

to generate $t\bar{t}$ events is ALPGEN [32], using the CTEQ6L1 [52] parton distribution function. The parton shower and fragmentation processes are handled by HERWIG [33].

To evaluate the effect of different fixed-order calculations, the POWHEG [53] generator is used, interfaced with HERWIG. Uncertainty in the showering algorithm is evaluated using ALPGEN samples interfaced with PYTHIA. Another uncertainty is associated with the total amount of parton showering that occurs during the fragmentation process. To evaluate this, ACERMC [54] samples interfaced with PYTHIA are generated with different values for the parameters which govern the amount of showering. The varied values are consistent with the PERUGIA Hard/Soft tune [55]. The systematic is taken as the average difference when the samples with the ‘up’ and ‘down’ variation of these parameters are used. Finally, there are a number of uncertainties related to the parton distribution function set used in the generation process which can effect the kinematics of the decay products. Uncertainties for the leading-order parton distribution function used by the ALPGEN generator is evaluated in two steps. In both cases, an event weight related to the difference in parton distribution function is calculated using the MC@NLO [56] generator. The analysis is re-run with the new event weights, and the systematic is taken as the observed change in the final value of R_{HF} . The first step in the calculation involves uncertainties on the parameters in a next-to-leading-order parton distribution function. The second step compares the central value when the leading-order parton distribution function used by ALPGEN and the next-to-leading-order parton distribution function used in the uncertainty calculation are used. These variations are statistically independent and added in quadrature.

A list of the Monte Carlo samples used to evaluate the uncertainties in top quark modeling are listed in Tables 24 and 25. A comparison of the fitted number of HF jets (N_{fit}), the

acceptance factor for $\sigma_{\text{fid}}(t\bar{t} + \text{HF})$, and the value of R_{HF} are presented in Table 6 for a number of different Monte Carlo samples.

Sample	N_{fit}	ϵ_{fit}	$\sigma_{\text{fid}}(t\bar{t} + j)$	R_{HF}
ALPGEN + HERWIG	78.7 ± 13.6	0.070 ± 0.003	3.04 ± 0.08 pb	0.079 ± 0.014
ALPGEN + PYTHIA	83.8 ± 11.5	0.075 ± 0.005	3.09 ± 0.08 pb	0.078 ± 0.012
ACERMC, more PS	81.2 ± 14.6	0.078 ± 0.002	3.16 ± 0.08 pb	0.070 ± 0.013
ACERMC, less PS	81.6 ± 15.9	0.076 ± 0.003	3.07 ± 0.08 pb	0.074 ± 0.015
POWHEG + HERWIG	76.0 ± 14.5	0.067 ± 0.002	3.23 ± 0.08 pb	0.074 ± 0.015
ALPGEN + PYTHIA, kt fac = 2.0	85.2 ± 13.0	0.064 ± 0.004	3.31 ± 0.09 pb	0.086 ± 0.014
ALPGEN + PYTHIA, kt fac = 0.5	71.5 ± 13.9	0.071 ± 0.005	2.87 ± 0.08 pb	0.074 ± 0.016
MC@NLO	78.9 ± 15.8	0.061 ± 0.003	3.32 ± 0.09 pb	0.096 ± 0.017
POWHEG + PYTHIA	78.9 ± 15.8	0.075 ± 0.002	3.41 ± 0.09 pb	0.066 ± 0.013

Table 6: Fit result, acceptance factor, $\sigma_{\text{fid}}(t\bar{t} + j)$, and R_{HF} compared across a number of generators. ALPGEN + HERWIG is the baseline sample used in the rest of the analysis. ALPGEN + PYTHIA and ACERMC samples are used to evaluate showering and initial / final state radiation systematics. POWHEG + HERWIG is used to quote a systematic on the event generator (ALPGEN). MC@NLO, POWHEG + PYTHIA, and ALPGEN + PYTHIA with varied kt factors are quoted only as a reference.

One component of the systematic uncertainty related to the generation of $t\bar{t}$ events is the fraction of $t\bar{t} + \text{HF}$ events which contain an extra b -jet (rather than an extra c -jet). This ratio is called $f_{b/HF}$. Since b -jets are tagged with approximately twice the efficiency as c -jets, the value of $f_{b/HF}$ will strongly affect the fiducial acceptance factor used in the calculation of $\sigma_{\text{fid}}(t\bar{t} + \text{HF})$. This effect is not taken into account with this systematic. Instead, a data-driven approach is taken to evaluate a systematic on $f_{b/HF}$, as discussed in Section 7.9.

7.6 RSS method

The RSS method (described in Chapter 6) is sensitive to any systematic mis-modeling of the charge correlation in events containing a fake lepton in the Monte Carlo. One way in which this uncertainty can be manifested is in the rate at which different kinds of events with a fake lepton occur. For electrons, there are three principle sources of fake leptons: real

electrons from a converted photon, real electrons from a heavy-flavor hadron, and hadrons mis-identified as electrons. For muons, fake leptons come mostly from real muons resulting from the decay of a heavy-flavor hadron, though a small contribution from mis-identified hadrons is also observed.

Monte Carlo shows that the dominant source of fake events (events with at least one fake lepton) are real $t\bar{t}$ events where one of the leptons is a fake. The first class of these events are those in which a fake comes from one of the b -jets produced in the $t \rightarrow Wb$ decay. Since either b -jet may produce the fake lepton, there is little average correlation between the charge of the real lepton and the charge of the fake. The second class of events are those in which the fake is produced via some radiative process (a photon, light quark, or gluon). On average, there will be no correlation between the charge of a fake produced in this way and the real lepton in the event. The third and final class of fake events are those in which the fake is produced by the decay products of a hadronically decaying W . Significant charge correlation is observed in these events, as a result of charge conservation. As the $t\bar{t}$ pair have net 0 charge, the two W bosons produced in by the decay of the $t\bar{t}$ pair will have opposite sign. The charge of the lepton produced by a W decay will have the same charge as the W itself. Similarly, the charge of a high p_T hadron produced by the decay of a W (such as would fake a lepton) will also have the same charge as the W . As such, a charge correlation exists between leptons in events where the fake comes from the hadronic decay products of a W boson in a $t\bar{t}$ event. Since the dominant decay mode for W 's is to light quarks, this affect is seen most prominently in events with light flavor fakes. As shown in Table 4, the OS/SS ratio is approximately 1:1 for events containing only heavy-flavor or conversion fakes, while it is between 1.5 and 4 for events with a light-flavor fake. Specifically, the nominal OS/SS

ratio used is 1.32 ± 0.10 (stat.) ± 1.82 (sys.) for ee , 1.15 ± 0.07 (stat.) ± 0.68 (sys.) for $\mu\mu$, and 1.16 ± 0.03 (stat.) ± 0.54 (sys.) for $e\mu$. The systematic uncertainty is computed by comparing the nominal OS/SS ratio with that obtained using only LF fakes.

To further support this interpretation, truth information is used to classify events with a light flavor fake by whether or not the fake lepton was produced by a W . As can be seen in Table 3, the OS/SS ratio for events with a light flavor fake is approximately four times larger when the fake is identified as coming from a W .

It is expected that the Monte Carlo does not accurately model the total fake rate or the relative rate for each type of fake event. The RSS method is insensitive to the total fake rate in the Monte Carlo, but it can be biased if the relative rates are badly modeled. To be conservative, our systematic is evaluated assuming the largest possible deviation from the baseline in the final fake yield. This is accomplished by assuming that all fake events are light-flavor. To evaluate this systematic for the fit, we use the OS/SS ratio for light-flavor fakes to re-calculate the normalization for the fake lepton templates. Since no SS events are observed in the signal region (see Chapter 9) we also consider the up-ward statistical fluctuation on 0 (1.38). For systematics in control regions, the fake lepton estimate is simply re-scaled by the ratio of the OS/SS ratios.

7.7 Fit template uncertainties

As described in Chapter 6, in the fit to the signal sample, the template used to describe b -jets from the top quark decay is derived using b -tagged jets in $t\bar{t}$ events with exactly two b -tags. The Monte Carlo predicts that 97% of the jets in this sample are b -jets from the top

decay, and a subtraction is made to remove the remaining background. Two assumptions are made here, and we assess a systematic for each one. Firstly, it is assumed that the kinematics of b -jets from top are the same whether or not there is additional HF content in the event. We test this assumption by replacing the b -jet from top template derived in the data with one derived in the Monte Carlo in events with 3 or more b -tagged jets. Secondly, it is assumed that the Monte Carlo accurately predicts the background for b -jets from top in the data-driven selection. To assess a systematic on this assumption, the scale of the subtraction is varied up and down by 25%, which corresponds to the statistical uncertainty on the background in the Monte Carlo. In both cases, a new fit is run, and the systematic is taken as the difference in the final value of R_{HF} .

The normalization of the template for b -jets from the top decay is derived by assuming that two b -tagged jets in each event are from from the top decay, which leads to a relative normalization of 65%. The normalization for b -jets from the top decay is assumed fixed in the fit, and thus not treated as a floating parameter in the fit, as described in Chapter 6. The Monte Carlo predicts this relative normalization to be 61%, meaning that some events in our signal region contain more than one b -tagged jet not from the top decay. The fit is re-run assuming the normalization predicted by the Monte Carlo, and we quote a systematic as the difference in final R_{HF} values.

Lastly, when considering the template for b -jets not from the top decay, it is assumed that the Monte Carlo accurately predicts the kinematic features of b -jets which contain one b -quark as compared to two b -quarks. It is known that the presence of two b -quarks in a single jet can lead to a bias towards a higher observed vertex mass. Since the dominant production mechanism for the additional b -jets is predicted to be gluon splitting to two

b -quarks, it is important that the Monte Carlo accurately predicts the correct fraction of additional b -jets with two b -quarks. To assess a systematic on this, we replace the nominal template for additional b -jets with the nominal template b -jets from the top decay (b -tagged jets in events in the data with exactly two b -tagged jets). It is assumed that these b_t -jets contain only one b -quark, and the difference in the ratio of additional b -jets with one and two b -quarks is covered by assuming all additional b -jets contain one b -quark.

7.8 Fit template cross-checks

As detailed in previous sections, a number of systematic uncertainties that affect the shape of the vertex mass distributions used in our fit are considered. To double check that the systematic uncertainty range is sufficient, we compare data and Monte Carlo in control regions enriched by the three primary types of jets: b , c , and light. The ratio of data to Monte Carlo is measured in bins of vertex mass, and these scale factors are used to re-weight the Monte Carlo for a new fit. We then compare the modified fit result to the baseline result with all other fit systematics included.

The control regions are defined by considering all $t\bar{t}$ events with exactly one b -tagged jet. The b -enriched control region is taken to be all b -tagged jets passing the tight b -tagging selection. The medium b -tagging selection is used to define a region with a higher (but still small) fraction of c -jets. Finally, two control regions are defined for light jets: jets failing the loosest b -tagging requirement, and jets which have a reconstructed axis opposite the direction of the jet. The vertex mass comparison in these four control regions is shown in Figure 22.

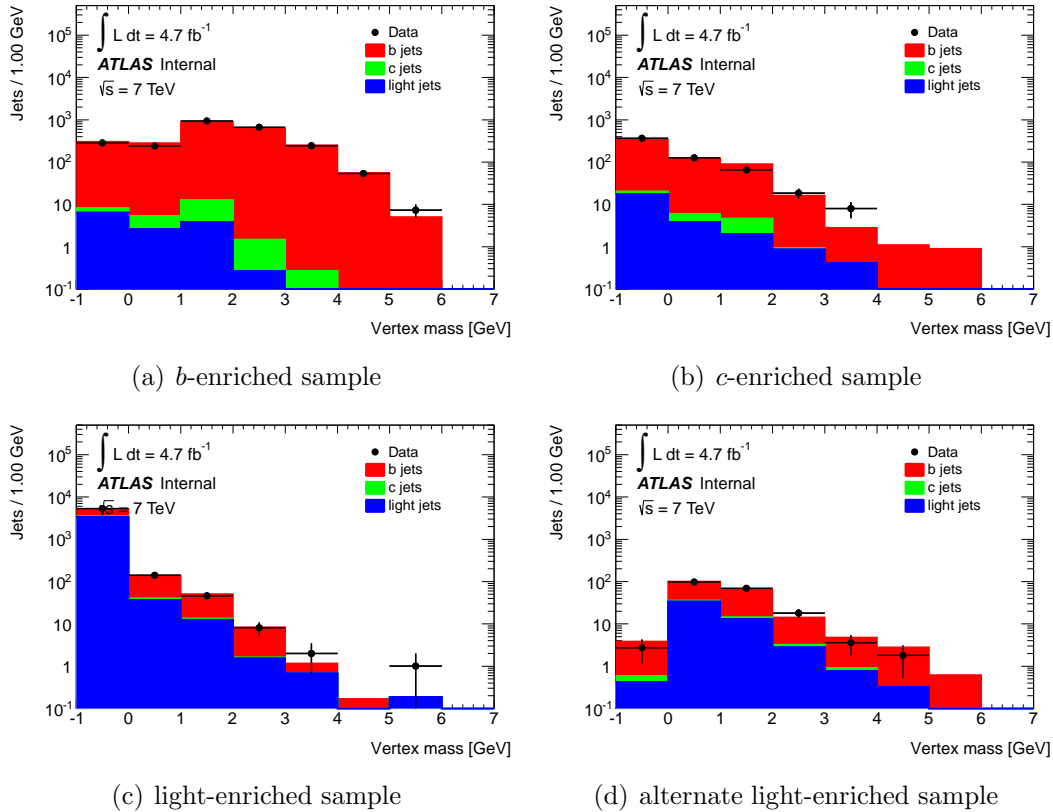


Figure 22: Comparison of data and MC for vertex mass in three regions of MV1 weight. The samples are defined using dilepton events with exactly one *b*-tagged jet. The *b*-enriched region selects all jets with MV1 weight above the 60% efficiency point (a). The intermediate region contains all jets with MV1 weights between the 60 and 75% efficiency points (b). The light-enriched region contains all jets that fail the 75% efficiency point (c) and which have a jet axis pointed opposite the direction of the jet (d).

The scale factors used to re-weight the Monte Carlo are shown in Figure 23. It is found that the total systematic estimate from the sources listed in sections 7.1 - 7.7 are sufficient to cover the variation found by applying these scale factors (see Chapter 9). As such, no extra systematics are assessed, and we are confident that the shapes of the vertex mass distribution for *b*, *c*, and light jets are well described.

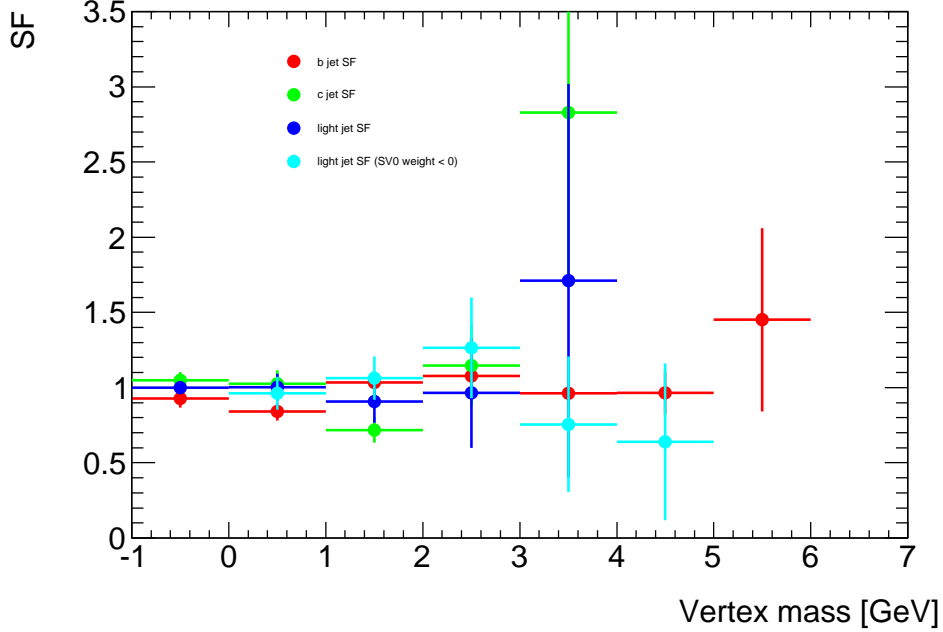


Figure 23: Scale factors used to evaluate the modeling systematic associated with the vertex mass templates used to fit for the flavor composition of extra jets in the signal region.

7.9 Acceptance calculation

As discussed previously, the fiducial acceptance factor for $\sigma_{\text{fid}}(t\bar{t} + \text{HF})$ is sensitive to the fraction of $t\bar{t} + \text{HF}$ events which contain an extra b -jet ($f_{b/\text{HF}}$). This dependence is shown in Figure 24. One approach to evaluate this uncertainty is to look at different Monte Carlo generators. Our analysis, however, does measure the fraction of reconstructed events which contain an additional b -jet. The statistical uncertainty on this measurement is not sufficient for us to quote a separate measure of $t\bar{t} + b$, but we can use it to place an upper limit on the value of $f_{b/\text{HF}}$. Assuming reconstruction efficiencies measured in the Monte Carlo for $t\bar{t} + b$ and $t\bar{t} + c$, we can convert the measured value for reconstructed $t\bar{t} + b$ events to a measured value for the generated value of $f_{b/\text{HF}}$. Because of the poor statistical resolution on the measurement of $t\bar{t} + b$, the central value for R_{HF} is quoted using the value of $f_{b/\text{HF}}$ taken

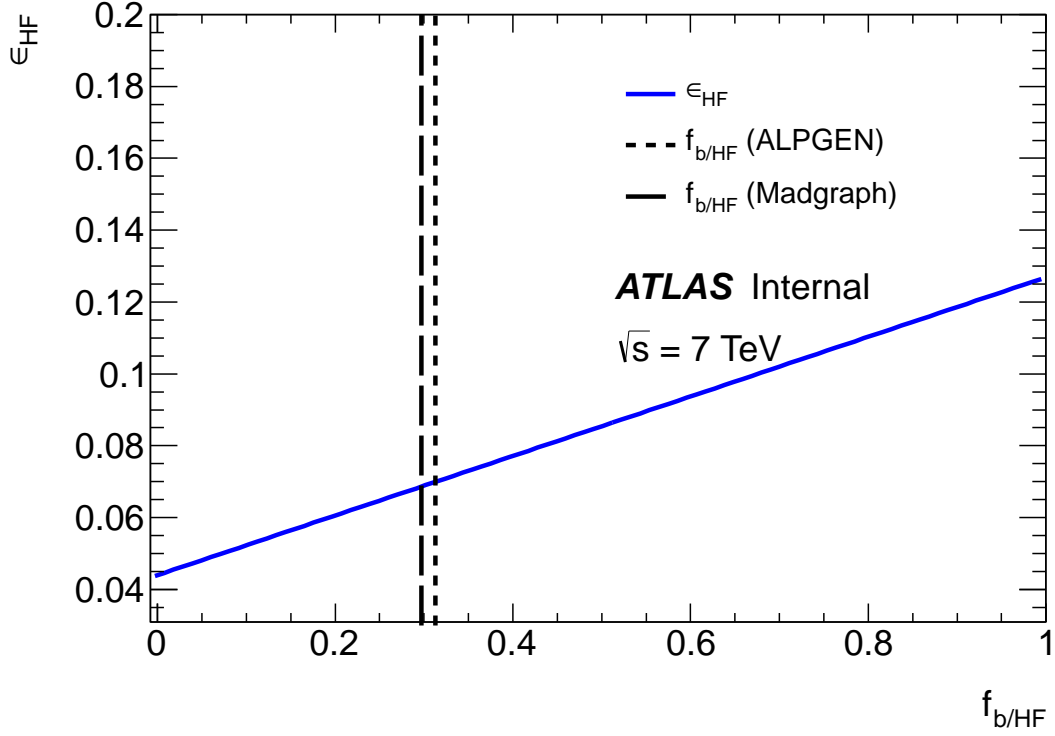


Figure 24: The fiducial acceptance factor used in the measurement of $\sigma_{\text{fid}}(t\bar{t} + \text{HF})$ as a function of $f_{b/HF}$. The value of $f_{b/HF}$ as predicted by the ALPGEN and MADGRAPH Monte Carlo generators are included for reference.

from the Monte Carlo. However, we use the difference in the predicted and fitted values of

$f_{b/HF}$ to assess a systematic on the value of R_{HF} .

8 Expected background and signal yields

In this chapter, the expected yields of signal and background events are presented for a number of event selections. First, we present the expectation in a number of control regions. These regions are defined by applying the nominal $t\bar{t}$ event selection, as defined in Chapter 5. Events with zero, one, and two b -tagged jets are considered separately to show that all relevant kinematics are well-modeled, independent of tagged jet multiplicity.

To validate that our method for estimating the background from fake leptons is accurately modeled, a different lepton selection is used. Using the nominal lepton selection, the fake background is expected to be very small, so it is difficult to accurately validate the method. To enrich the fake lepton background, a looser lepton selection is applied. As can be seen in Section 8.1, the predictions in this region agree with the data within standard systematic uncertainties, indicating the RSS method is sufficient to accurately model the fake lepton background.

Next, we compare the yield and expectation in events passing the full $t\bar{t}$ event selection, with 0, 1, and 2 b -tagged jets in Section 8.2. By demonstrating agreement between data and Monte Carlo for events passing this selection, we can be confident in our understanding of the data in our signal regions. A detailed break-down of the systematics in these regions is given in Section 8.3

For completeness, the yield of events where the two leptons have the same sign are shown in Section 8.4. This event selection is dominated by events with at least one fake lepton. Since the method used to evaluate this background is only defined for events with opposite-signed leptons, the Monte Carlo prediction is taken directly. It is not expected that the

Monte Carlo will accurately predict the fake rate, so good agreement between data and the total expectation is not expected. These regions are not used anywhere in the main analysis result, however, so good agreement is not required.

Finally, we present a number of studies done on the signal region used in this analysis. Yields and kinematic distributions in the signal region are presented to show that the Monte Carlo sufficiently models various properties of these events in Section 8.5. Systematics on the yield of events in the signal region are also presented. We also present a number of studies done using simulated data from Monte Carlo to show that our fit machinery will faithfully extract the flavor composition of the tagged jets in the signal region in Section 8.6. The predicted fit result and value for R_{HF} are also presented, in preparation for the final fit to the data.

8.1 Control regions with loose leptons

Using the lepton selection outlined in Chapter 5, the background due to events with a fake lepton is expected to be small. It is difficult to assess how well the RSS method works in this region. If, however, the lepton selection is loosened, a more sizeable fake background is observed.

For electrons, the selection outlined in Chapter 5 is used with the following changes:

- Loose ++ quality flag
- No isolation requirement

where the ‘loose ++’ quality flag is defined in reference [37]. In general, the selection cuts applied by the ‘loose’ flag are similar to, but not as restrictive as, the cuts used by the

Process	ee yield	$\mu\mu$ yield	$e\mu$ yield
$t\bar{t}$ + HF	4.7 ± 0.5	10 ± 0.7	27.9 ± 1.3
$t\bar{t}$ + LF	113.7 ± 3.7	194.5 ± 5.1	612.9 ± 9.2
Single top	10.7 ± 1	15 ± 1.3	56.2 ± 2.4
Z + jets	128.4 ± 5	190.4 ± 6.3	251.5 ± 6.9
WW,WZ,ZZ	34.2 ± 1.1	60.9 ± 1.6	209.4 ± 3
RSS fakes	53.9 ± 8.4	35.4 ± 6.7	668.1 ± 27.9
Total expectation	$345.7 \pm 10.6 \pm 61$	$506.6 \pm 10.8 \pm 71.4$	$1826.3 \pm 30.5 \pm 306.3$
Data	375	593	2054

Table 7: Event yield expected in 4.7 fb^{-1} in opposite-sign dilepton events with loose lepton selection. Uncertainties on individual components are statistical only. For the final estimate, systematics are included (listed second). To assess the validity of the RSS estimate, we compare the observed yield in data with the expected signal yield from Monte Carlo subtracted to the RSS estimate. These two numbers are in agreement, indicating the RSS method accurately predicts the background from events with fake leptons.

‘tight’ flag. Some track quality cuts (in particular the requirement of hits in the b-layer) are removed, as are the E/p cut and explicit conversion veto. Using a tag-and-probe analysis, it is shown that the ‘loose’ quality flag is approximately 95% efficient, though it does have a much higher fake rate.

Similarly, for muons, the default selection is used, with the following changes:

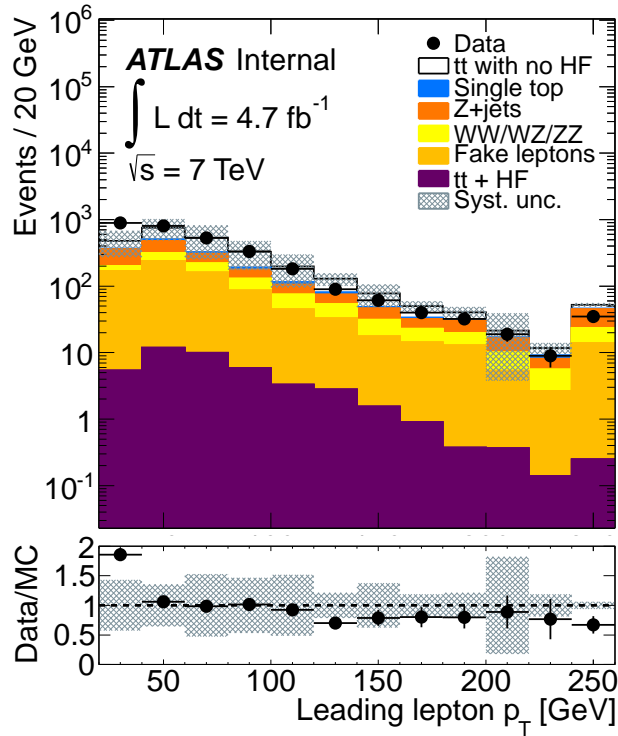
- Loose Muid quality flag
- No quality cuts on the ID track
- No isolation requirement

The ‘loose’ Muid quality flag admits muons reconstructed by any of the 4 reconstruction algorithms, rather than just Muid Combined.

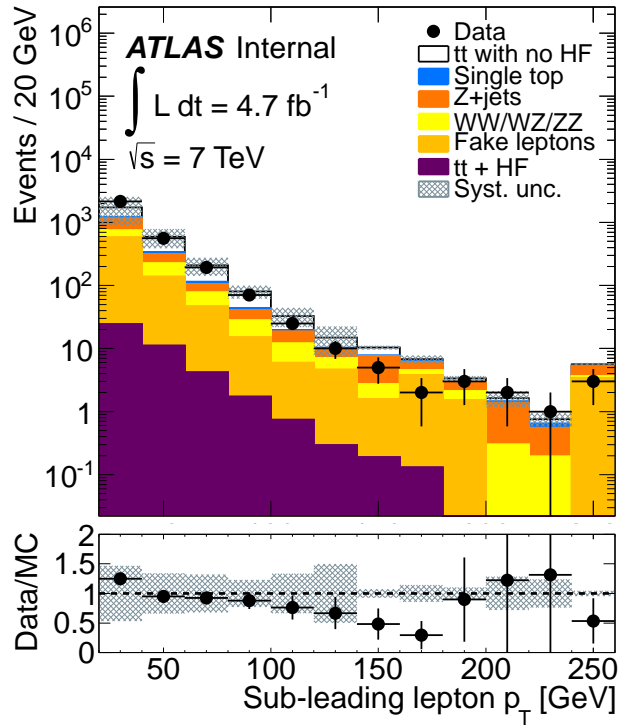
By applying the looser lepton selection described above, we can isolate a sample of $t\bar{t}$ candidate events with a relatively large fraction of fakes. As more b -tags are required, the

number of fake events decreases, so we isolate the most fake-enriched sample by requiring exactly 0 tagged jets. The expected and observed yields are compared in Table 7, and select kinematic distributions are shown in Figures 25 - 28.

Summed over channels, the total MC prediction without fakes is 1881 ± 16 (stat). The data yield is 3022 so the MC subtracted data, or fakes in data are 1141. The RSS method fake prediction is 757.4 ± 30 (stat). Within systematic uncertainties (± 317), the two estimates are in agreement, indicating the RSS method can accurately predict the fake background in regions expected to be relatively fake-enriched.

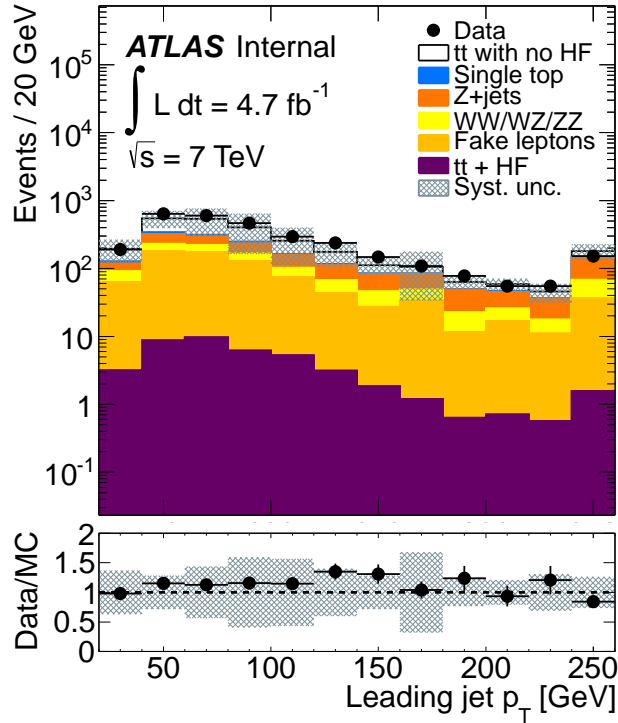


(a) Leading lepton p_T

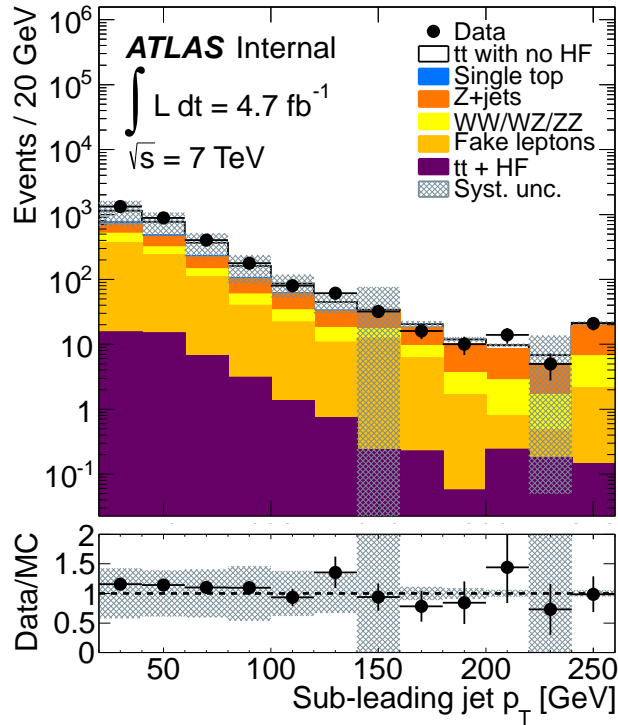


(b) Sub-leading lepton p_T

Figure 25: Leading (a) and sub-leading (b) lepton p_T observed using the loose dilepton $t\bar{t}$ event selection and 0 tagged jets.

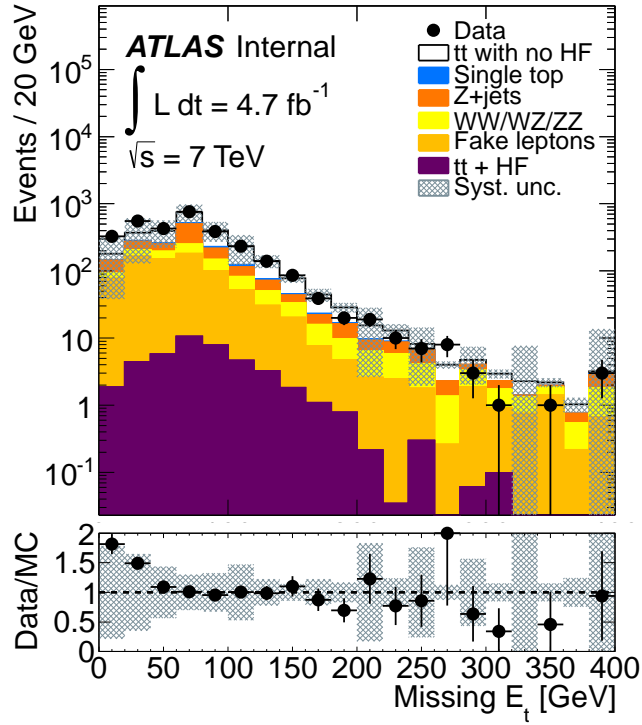


(a) Leading jet p_T

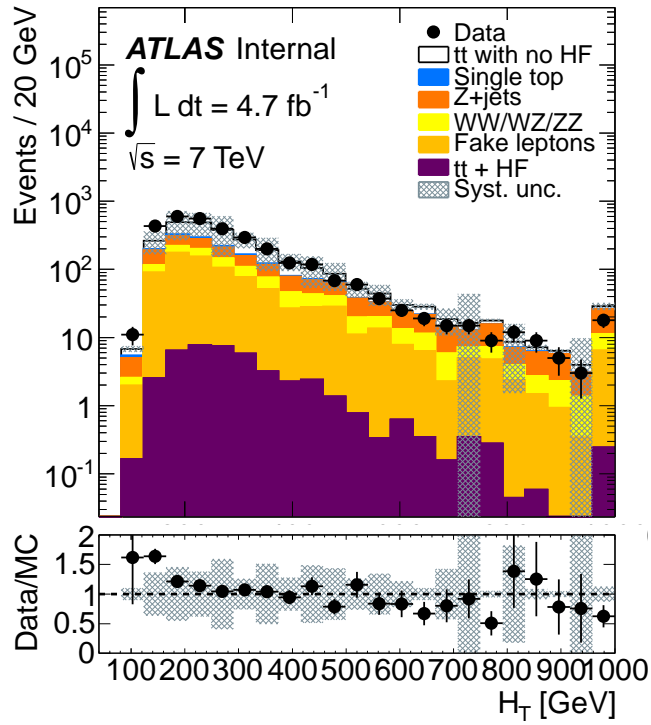


(b) Sub-leading jet p_T

Figure 26: Leading (a) and sub-leading (b) jet p_T observed using the loose dilepton $t\bar{t}$ event selection and 0 tagged jets.

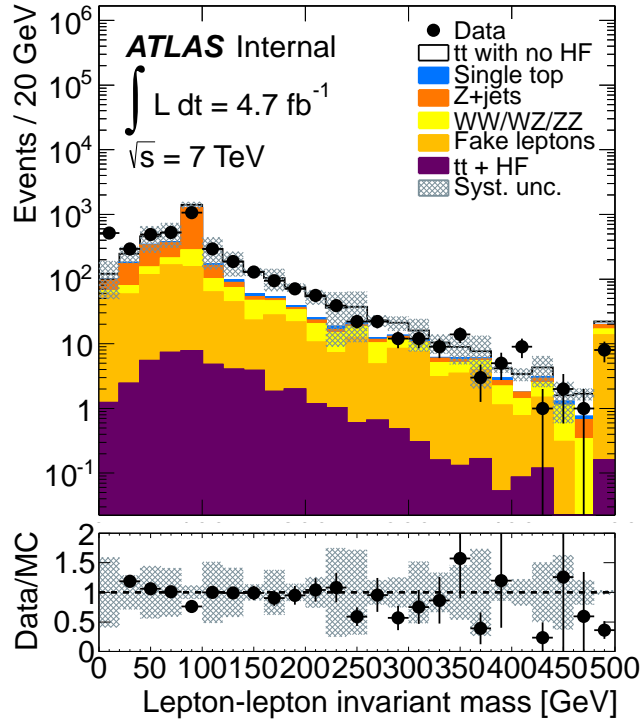


(a) E_T^{miss}

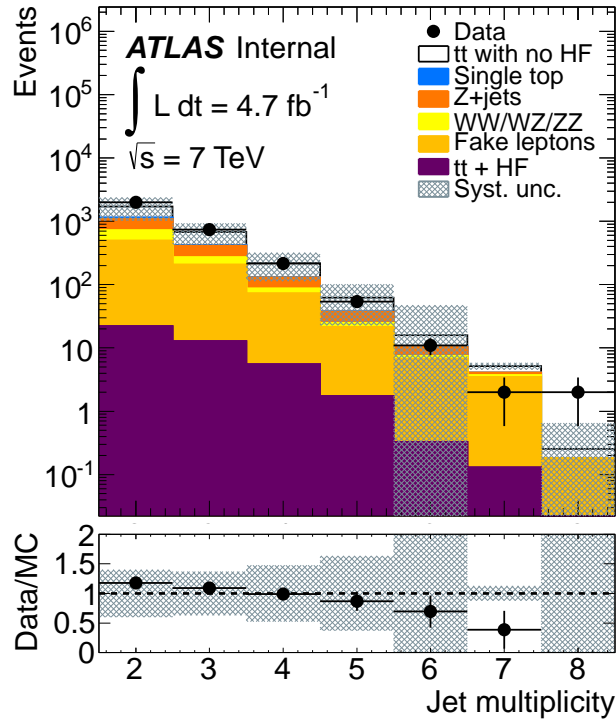


(b) H_T

Figure 27: E_T^{miss} (a) and H_T (b) observed using the loose dilepton $t\bar{t}$ event selection and 0 tagged jets.



(a) $M_{\ell\ell}$



(b) N_{jets}

Figure 28: Lepton-lepton invariant mass (a) and selected jet multiplicity (b) observed using the loose dilepton $t\bar{t}$ event selection and 0 tagged jets.

8.2 OS control regions

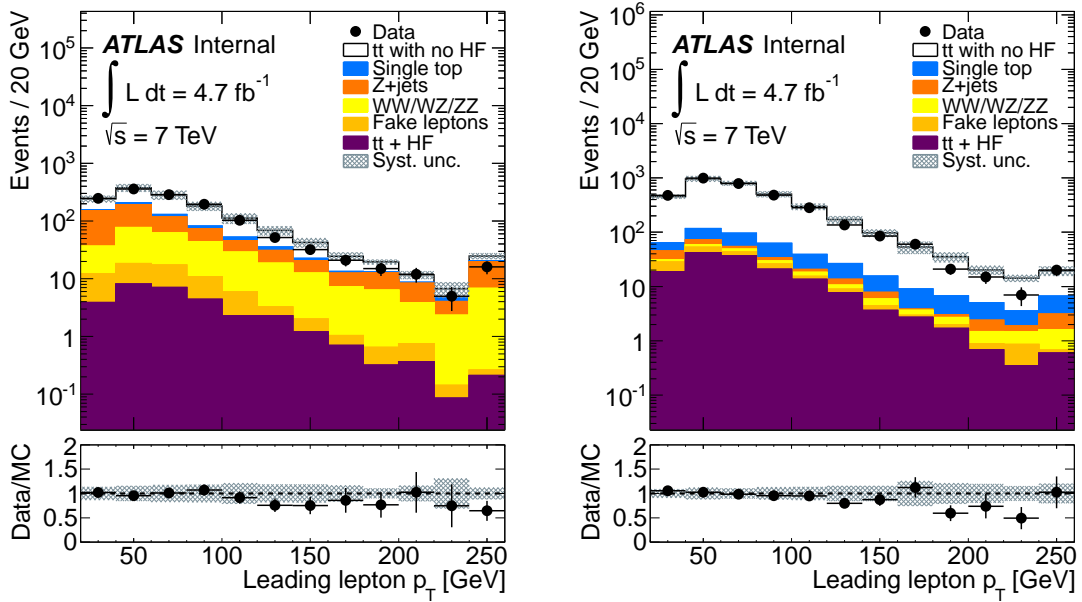
Process	ee yield	$\mu\mu$ yield	$e\mu$ yield
$t\bar{t}$ + HF	2.4 ± 0.4	8.6 ± 0.7	19.6 ± 1.1
$t\bar{t}$ + LF	60.4 ± 2.7	171.8 ± 4.8	423.9 ± 7.6
Single top	5.4 ± 0.7	13.9 ± 1.2	38.6 ± 2
Z + jets	49 ± 2.9	160.9 ± 5.7	170 ± 5.7
WW,WZ,ZZ	19.8 ± 0.9	55.9 ± 1.5	156.8 ± 2.6
RSS fakes	0 ± 0	0 ± 0	41.5 ± 6.9
Total expectation	$137.1 \pm 4.2 \pm 24.2$	$411.3 \pm 7.8 \pm 70$	$850.7 \pm 12.3 \pm 156.7$
Data	146	398	803

Table 8: Event yield expected in 4.7 fb^{-1} in the oppositely-charged dilepton sample with zero b -tagged jets. Uncertainties on individual components are statistical only. For the final estimate, systematics are included (listed second).

Process	ee yield	$\mu\mu$ yield	$e\mu$ yield
$t\bar{t}$ + HF	12.1 ± 0.9	39.4 ± 1.7	96.7 ± 2.7
$t\bar{t}$ + LF	269.5 ± 6	759.9 ± 10.4	1952 ± 16.8
Single top	17.8 ± 1.3	45.1 ± 2.1	124.4 ± 3.5
Z + jets	7.7 ± 1.2	23.9 ± 2.1	18 ± 1.8
WW,WZ,ZZ	2.2 ± 0.3	6.6 ± 0.5	16.9 ± 0.9
RSS fakes	12.4 ± 3.7	4.5 ± 2.1	20.3 ± 4.7
Total expectation	$322 \pm 7.4 \pm 42.1$	$879.7 \pm 11.2 \pm 112.1$	$2228.5 \pm 18.1 \pm 269.2$
Data	282	851	2228

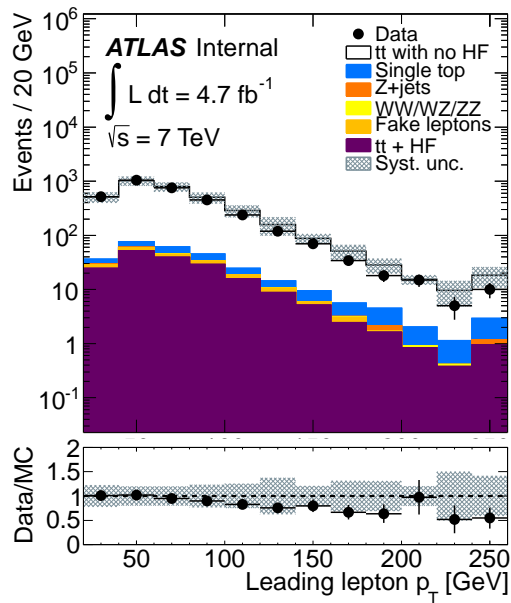
Table 9: Event yield expected in 4.7 fb^{-1} in the oppositely-charged dilepton sample with one b -tagged jet. Uncertainties on individual components are statistical only. For the final estimate, systematics are included (listed second).

In this section, we present the expected and observed yield in a number of control regions. The full set of selection criteria described in Chapter 5 is applied. In Tables 8 - 10, the yield of $t\bar{t}$ candidate events are presented separately by dilepton channel (ee , $\mu\mu$, and $e\mu$) for events with 0, 1 and 2 tagged jets. Select kinematic distributions are shown in Figures 29 - 36. Systematic uncertainties are assessed following the procedure used in Chapter 7.



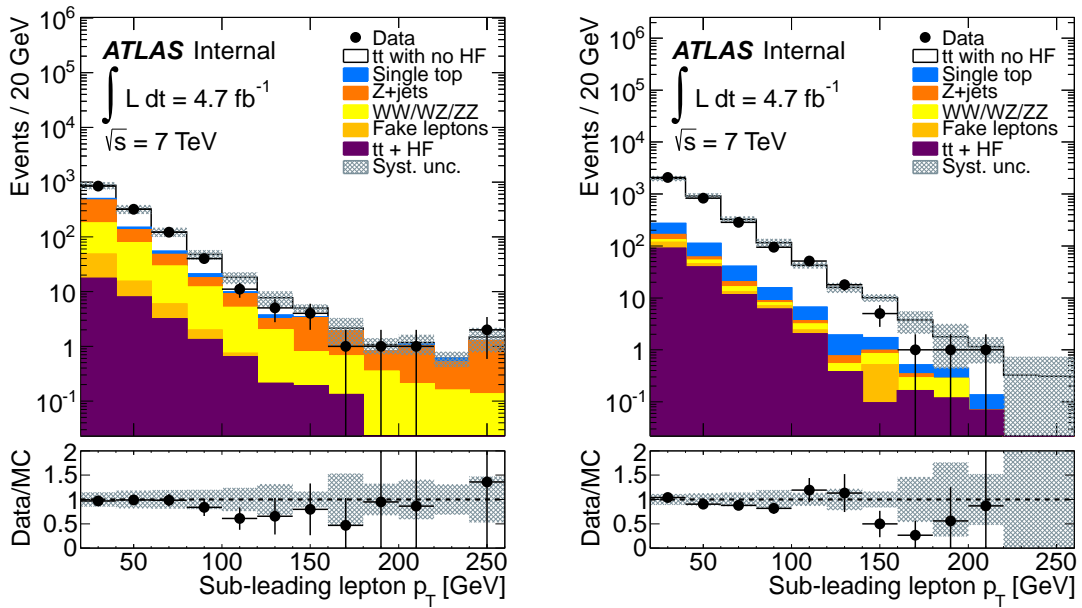
(a) 0 tags

(b) 1 tag



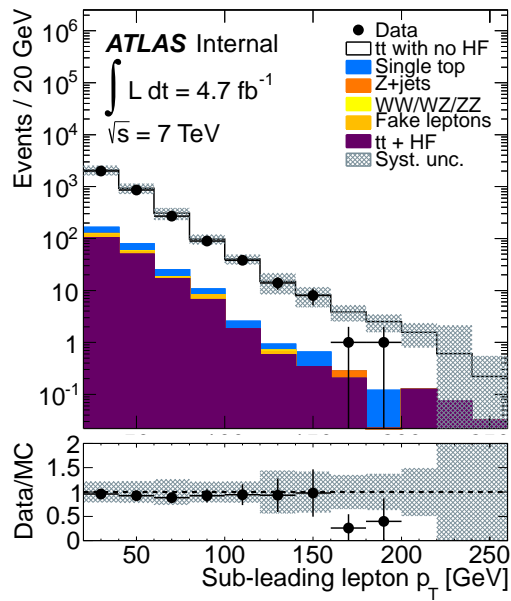
(c) 2 tags

Figure 29: Leading lepton p_T observed using the nominal dilepton $t\bar{t}$ event selection and 0 (a), 1 (b), or 2 (c) tagged jets. Statistical uncertainties are included on the data, while systematic error bands are included on the total prediction.



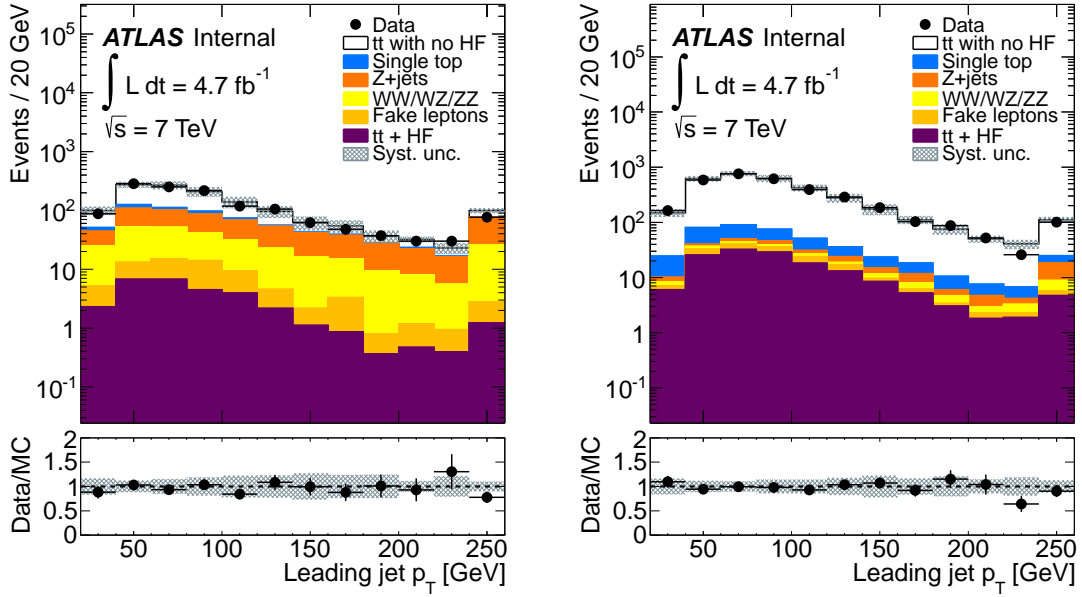
(a) 0 tags

(b) 1 tag



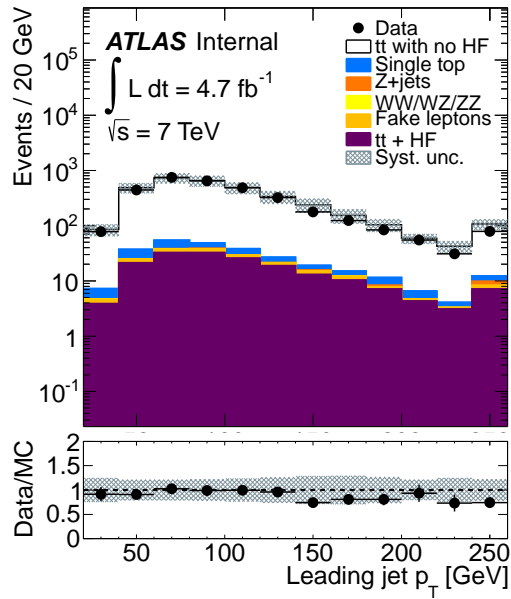
(c) 2 tags

Figure 30: Sub-leading lepton p_T observed using the nominal dilepton $t\bar{t}$ event selection and 0 (a), 1 (b), or 2 (c) tagged jets. Statistical uncertainties are included on the data, while systematic error bands are included on the total prediction.



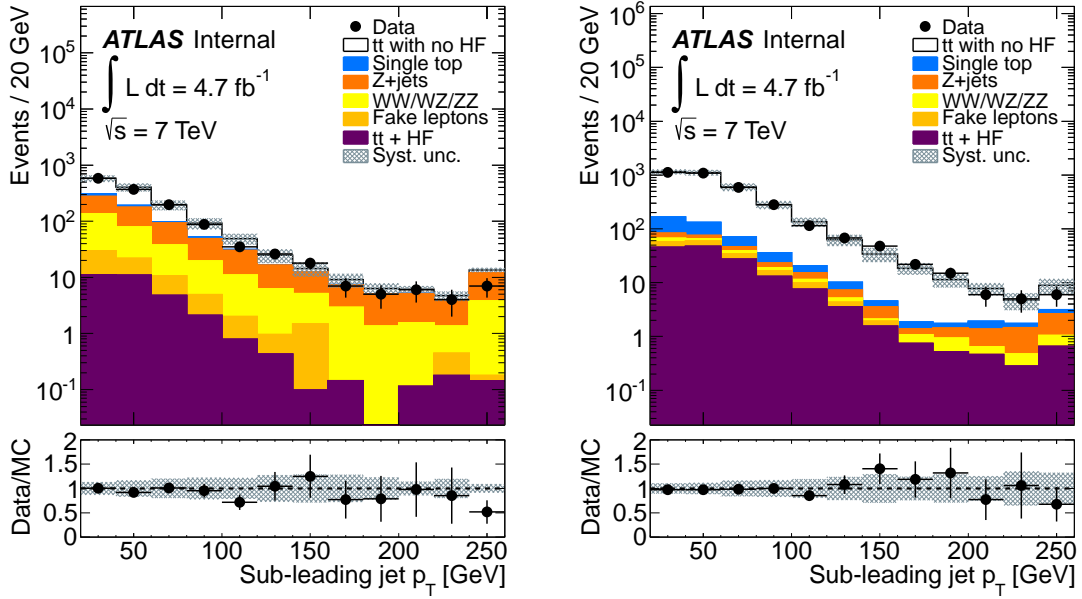
(a) 0 tags

(b) 1 tag



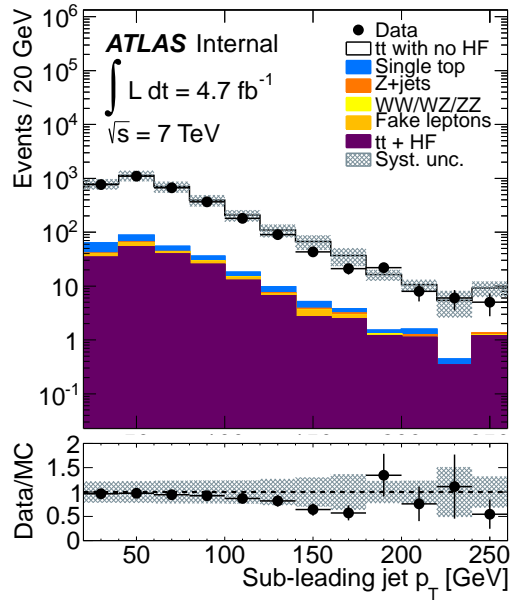
(c) 2 tags

Figure 31: Leading jet p_T observed using the nominal dilepton $t\bar{t}$ event selection and 0 (a), 1 (b), or 2 (c) tagged jets. Statistical uncertainties are included on the data, while systematic error bands are included on the total prediction.



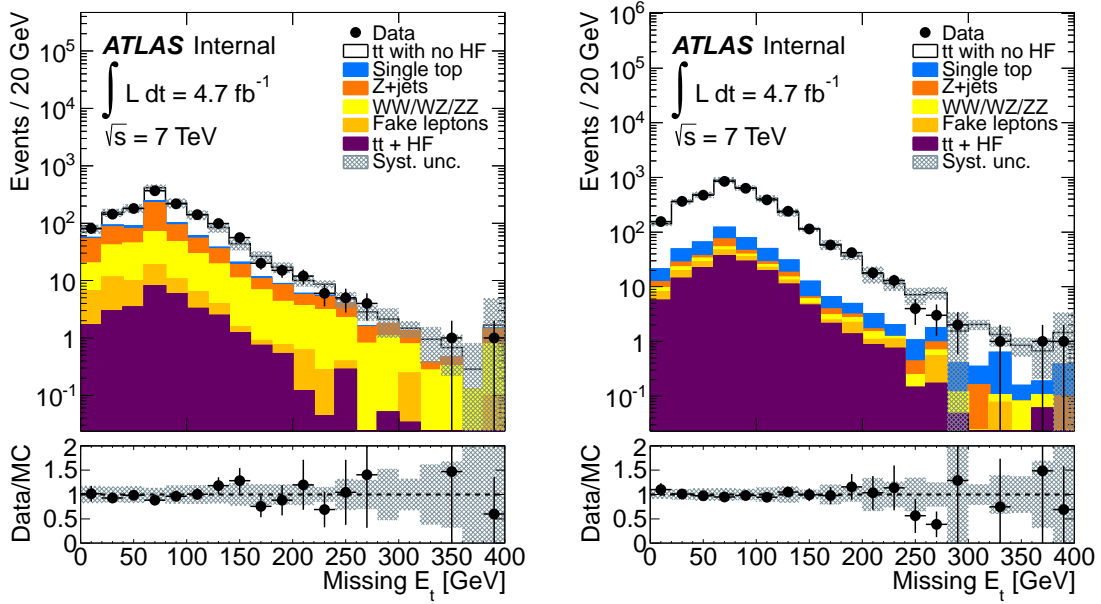
(a) 0 tags

(b) 1 tag



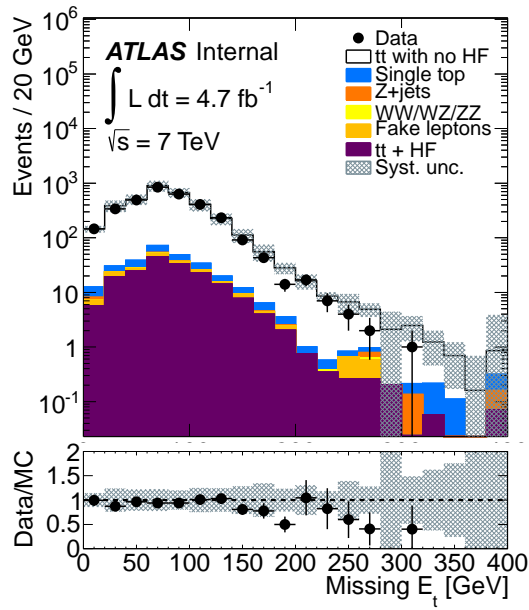
(c) 2 tags

Figure 32: Sub-leading jet p_T observed using the nominal dilepton $t\bar{t}$ event selection and 0 (a), 1 (b), or 2 (c) tagged jets. Statistical uncertainties are included on the data, while systematic error bands are included on the total prediction.



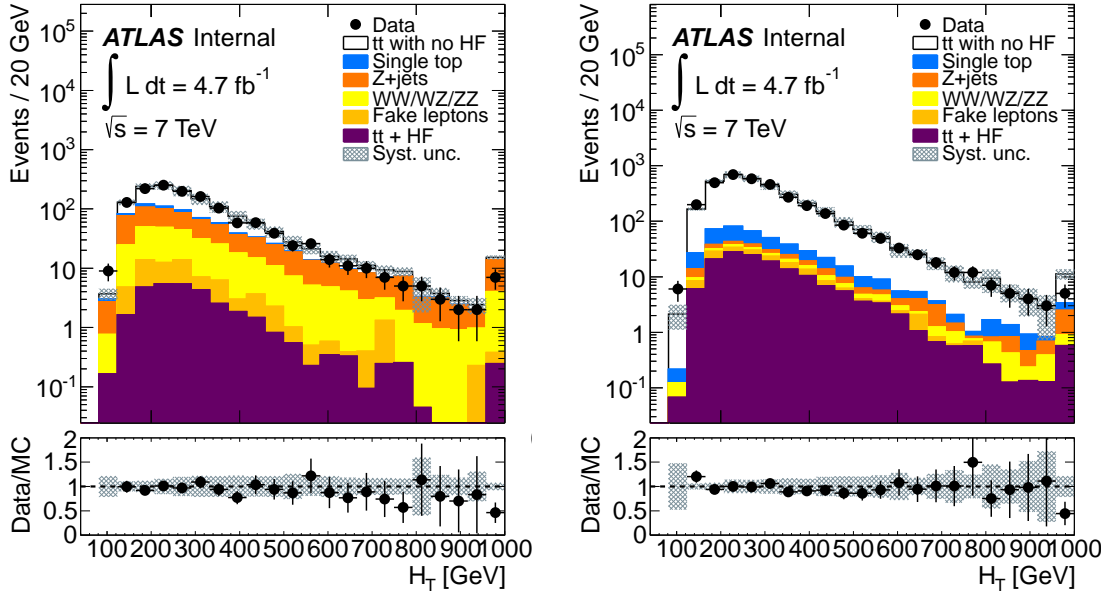
(a) 0 tags

(b) 1 tag



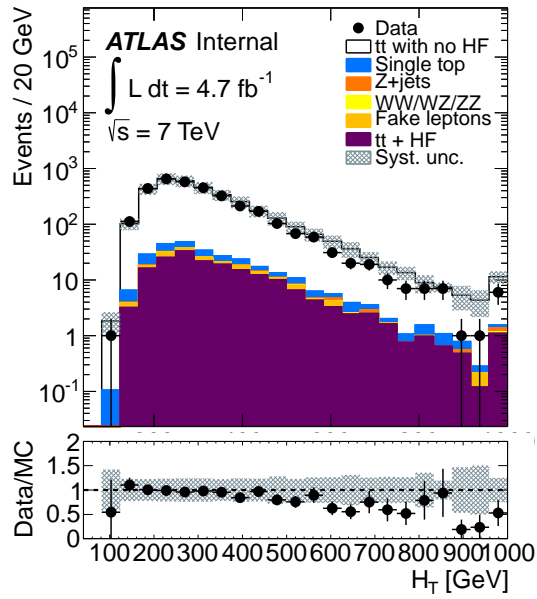
(c) 2 tags

Figure 33: E_T^{miss} observed using the nominal dilepton $t\bar{t}$ event selection and 0 (a), 1 (b), or 2 (c) tagged jets. Statistical uncertainties are included on the data, while systematic error bands are included on the total prediction.



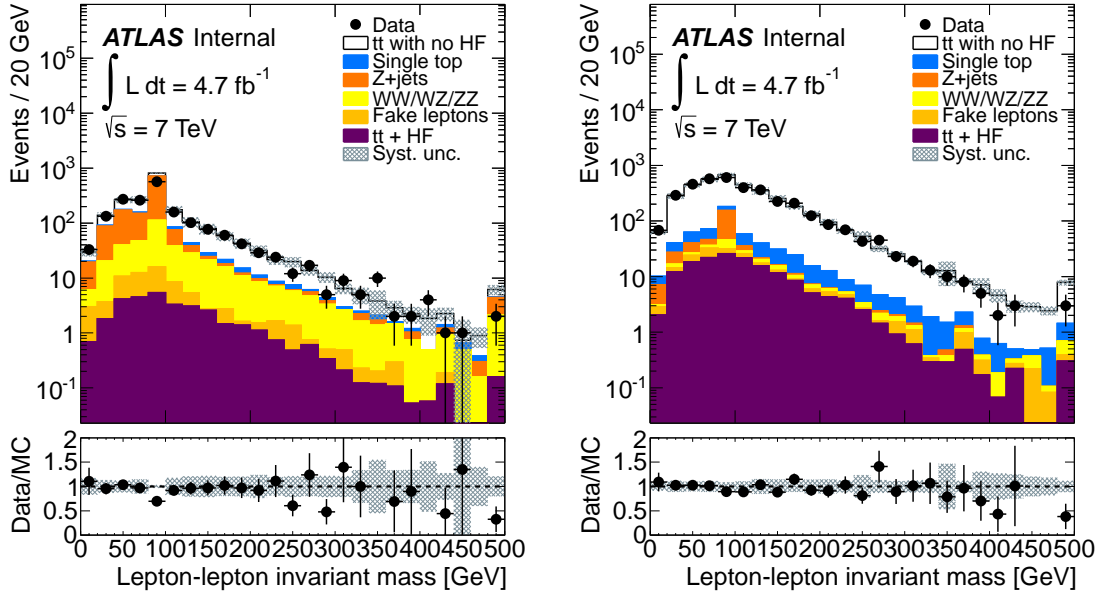
(a) 0 tags

(b) 1 tag



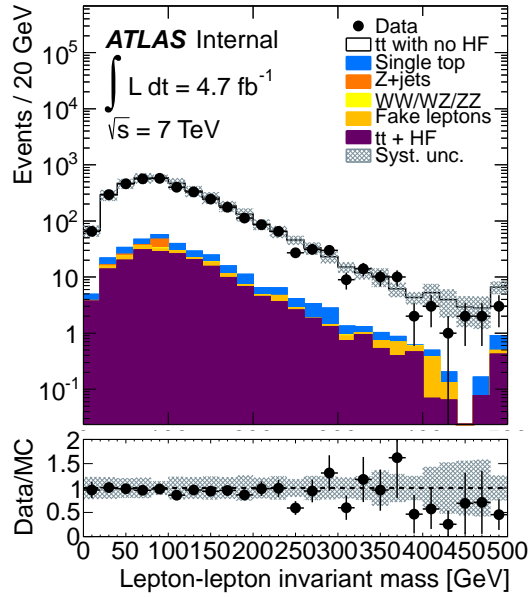
(c) 2 tags

Figure 34: H_T observed using the nominal dilepton $t\bar{t}$ event selection and 0 (a), 1 (b), or 2 (c) tagged jets. Statistical uncertainties are included on the data, while systematic error bands are included on the total prediction.



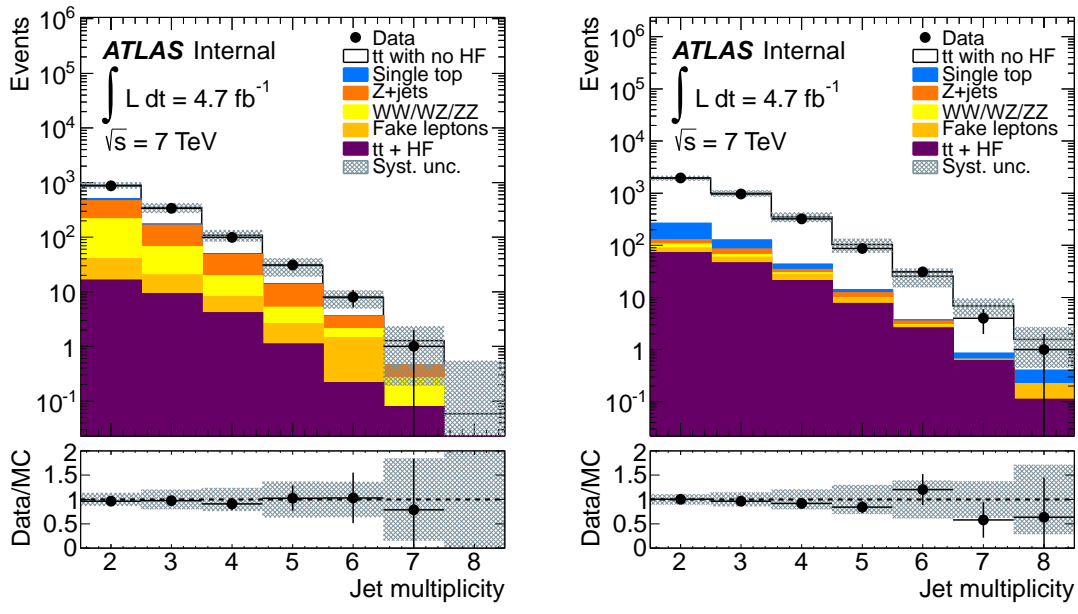
(a) 0 tags

(b) 1 tag



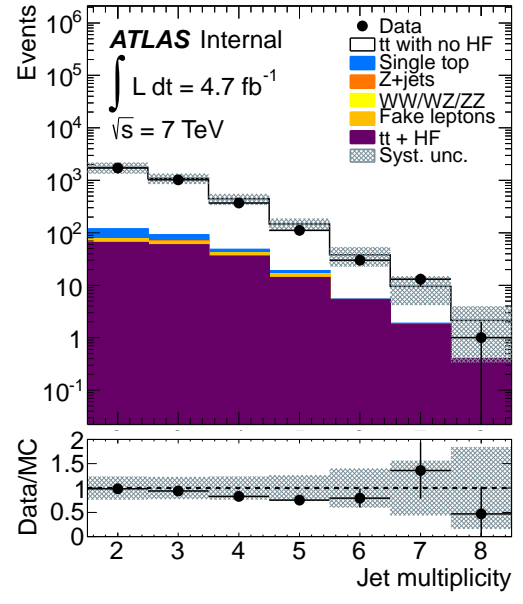
(c) 2 tags

Figure 35: Lepton-lepton invariant mass observed using the nominal dilepton $t\bar{t}$ event selection and 0 (a), 1 (b), or 2 (c) tagged jets. Statistical uncertainties are included on the data, while systematic error bands are included on the total prediction.



(a) 0 tags

(b) 1 tag



(c) 2 tags

Figure 36: Selected jet multiplicities observed using the nominal dilepton $t\bar{t}$ event selection and 0 (a), 1 (b), or 2 (c) tagged jets. Statistical uncertainties are included on the data, while systematic error bands are included on the total prediction.

Process	ee yield	$\mu\mu$ yield	$e\mu$ yield
$t\bar{t}$ + HF	16.8 ± 1.1	47.9 ± 1.8	115.1 ± 2.9
$t\bar{t}$ + LF	288 ± 6.4	802.9 ± 11	2115.6 ± 17.8
Single top	5.3 ± 0.8	18 ± 1.4	46.6 ± 2.2
Z + jets	0.2 ± 0.1	2 ± 0.5	2.3 ± 0.8
WW,WZ,ZZ	0.1 ± 0	0.3 ± 0.1	0.7 ± 0.1
RSS fakes	5 ± 2.6	2.7 ± 1.9	18 ± 5
Total expectation	$315.8 \pm 7.1 \pm 87.8$	$874 \pm 11.4 \pm 209$	$2298.6 \pm 18.9 \pm 568.2$
Data	302	782	2189

Table 10: Event yield expected in 4.7 fb^{-1} in the oppositely-charged dilepton sample with two b -tagged jets. Uncertainties on individual components are statistical only. For the final estimate, systematics are included (listed second).

8.3 Systematics in OS control regions

Source	% yield (2 tag)	% yield (1 tag)	% yield (0 tag)
jer	0.7	0.0	1.4
jes up	2.4	2.4	4.7
jes down	2.4	2.4	4.7
el sf up	2.0	2.0	2.0
el sf down	2.0	2.0	2.0
mu sf up	1.9	1.9	1.8
mu sf down	1.9	1.8	1.8
b eff up	12.9	6.2	12.6
b eff down	12.1	4.6	14.2
c eff up	0.0	0.0	0.3
c eff down	0.0	0.0	0.3
l eff up	0.2	0.0	0.7
l eff down	0.2	0.0	0.8
JVF scale factor up	0.8	1.0	1.1
JVF scale factor down	1.0	1.0	1.0
E_T^{miss} cellout, soft jet up	0.1	0.0	0.1
E_T^{miss} cellout, soft jet down	0.0	0.1	0.0
HF enriched RSS	0.0	0.0	0.0
LF enriched RSS	0.7	0.7	1.1
Conversion enriched RSS	0.1	0.1	0.4
Showering	9.1	3.3	2.5
Generator (Powheg + Herwig)	13.6	9.1	2.2
ISR/FSR (Acer)	12.6	1.4	8.9
PDF (LO)	3.3	3.5	2.2
Total	24.5	11.9	17.5

Table 11: A summary of systematic uncertainties affecting the predicted yield of events of $t\bar{t}$ candidate events with 0, 1, and 2 tags.

In this section, we present the systematic uncertainties associated with the expected yield in the 0, 1, and 2 b -tagged jet control regions. An explanation of the components used in this calculation are given in Chapter 7. A detailed breakdown of the systematic uncertainty on the yield in these control regions can be found in Table 11. The dominant uncertainties are associated with the b -tagging efficiency and the modeling of the top quark decay process. It is observed that the uncertainty for the b -tagging efficiency and the showering systematic are relatively large for the 0 and 2- b -tag bins, while it is smaller in the 1 b -tag bin. This effect is understood as a result of movement into and out of each bin. For the 0 (2) b -tag

bins, jets can only leave (enter) these bins. For the 1 b -tag bin, jets are allowed to both enter and leave, so the final uncertainty is greatly reduced.

8.4 SS control regions

Process	ee yield	$\mu\mu$ yield	$e\mu$ yield
$t\bar{t}$ + HF	0 ± 0	0 ± 0	0 ± 0
$t\bar{t}$ + LF	0.2 ± 0.1	0 ± 0	0.2 ± 0.1
Single top	0 ± 0	0 ± 0	0 ± 0
Z + jets	0.2 ± 0.2	0.2 ± 0.1	0.4 ± 0.2
WW,WZ,ZZ	4.5 ± 0.4	7.1 ± 0.5	30.5 ± 1.2
MC fakes	1.6 ± 0.4	1.8 ± 0.5	13.4 ± 1.8
Total expectation	$6.7 \pm 0.6 \pm 0.4$	$9.2 \pm 0.8 \pm 0.4$	$45.2 \pm 2.3 \pm 2$
Data	4	6	66

Table 12: Event yield expected in 4.7 fb^{-1} in the same-sign dilepton sample with zero b -tagged jets. Uncertainties on individual components are statistical only. For the final estimate, systematics are included (listed second).

Process	ee yield	$\mu\mu$ yield	$e\mu$ yield
$t\bar{t}$ + HF	0 ± 0	0 ± 0	0.1 ± 0
$t\bar{t}$ + LF	0.6 ± 0.2	0 ± 0	1.1 ± 0.4
Single top	0.1 ± 0.1	0 ± 0	0.1 ± 0.1
Z + jets	0 ± 0	0 ± 0	0 ± 0
WW,WZ,ZZ	0.5 ± 0.1	0.6 ± 0.1	3.9 ± 0.4
MC fakes	1.3 ± 0.3	3.6 ± 0.7	14 ± 1.7
Total expectation	$2.6 \pm 0.4 \pm 0.6$	$8.9 \pm 4.7 \pm 0.8$	$19.4 \pm 1.9 \pm 1.1$
Data	2	5	26

Table 13: Event yield expected in 4.7 fb^{-1} in the same-sign dilepton sample with one b -tagged jet. Uncertainties on individual components are statistical only. For the final estimate, systematics are included (listed second).

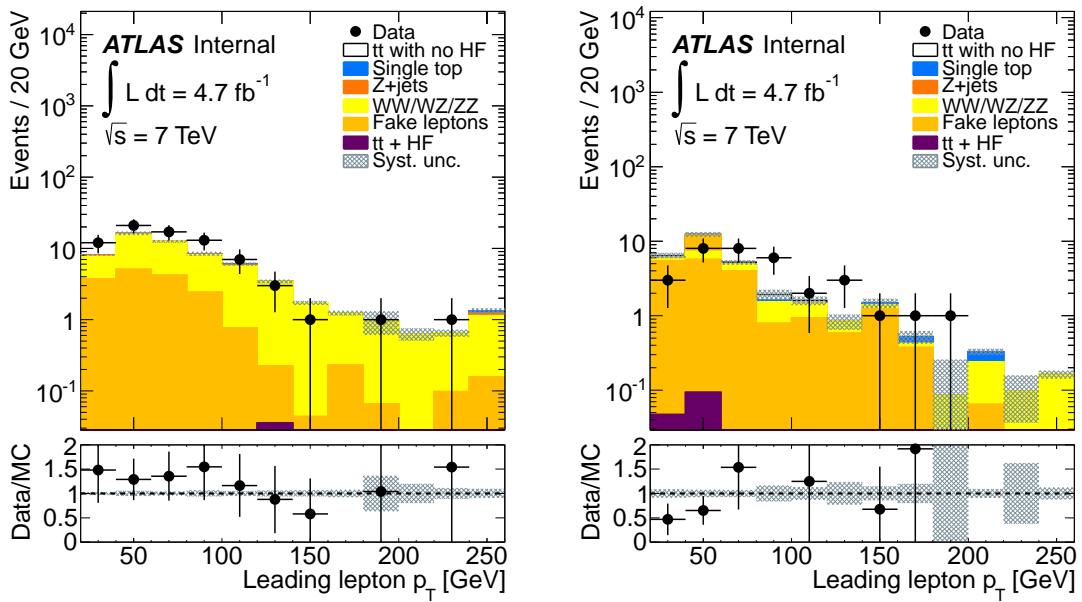
In this section, we present the expected and observed yield in a number of same-sign $t\bar{t}$ control regions. The full set of selection criteria described in Chapter 5 is applied, but the requirement of oppositely charged leptons is inverted. Events containing a pair of same-sign

Process	ee yield	$\mu\mu$ yield	$e\mu$ yield
$t\bar{t}$ + HF	0 ± 0	0 ± 0	0 ± 0
$t\bar{t}$ + LF	0.4 ± 0.1	0 ± 0	1.8 ± 0.5
Single top	0 ± 0	0 ± 0	0 ± 0
Z + jets	0 ± 0	0 ± 0	0 ± 0
WW, WZ, ZZ	0 ± 0	0 ± 0	0.1 ± 0
MC fakes	0.7 ± 0.3	0.7 ± 0.3	7 ± 1
Total expectation	$1.3 \pm 0.4 \pm 0.2$	$1.4 \pm 0.7 \pm 0.6$	$9.2 \pm 1.1 \pm 1.1$
Data	4	2	14

Table 14: Event yield expected in 4.7 fb^{-1} in the same-sign dilepton sample with two b -tagged jets. Uncertainties on individual components are statistical only. For the final estimate, systematics are included (listed second).

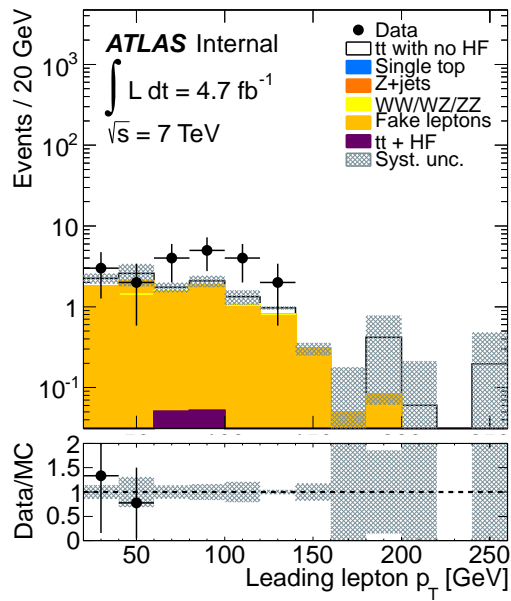
(SS) leptons is generally en-riched in di-boson events (for the 0 tag bin) or fakes (for bins with 1 and 2 tags). As a reminder, the background from fake leptons is modeled using the Monte Carlo, and it is not generally expected that this is well modeled. In Tables 12 - 14, the yield of $t\bar{t}$ candidate events are presented separately by dilepton channel (ee , $\mu\mu$, and $e\mu$) for events with 0, 1 and 2 b -tagged jets. Select kinematic distributions are shown in Figures 37 - 44. Systematic uncertainties are assessed following the procedure used in Chapter 7.

Since the RSS method is designed only to estimate fakes for events with an oppositely-charged pair of leptons, the Monte Carlo must be trusted to model fakes in the same-sign region. It is not expected that the Monte Carlo can accurately model processes involving fake leptons, so the agreement is not expected to be exact, given the large fraction of fake events passing the same-sign selection. These events are included for the sake of completeness.



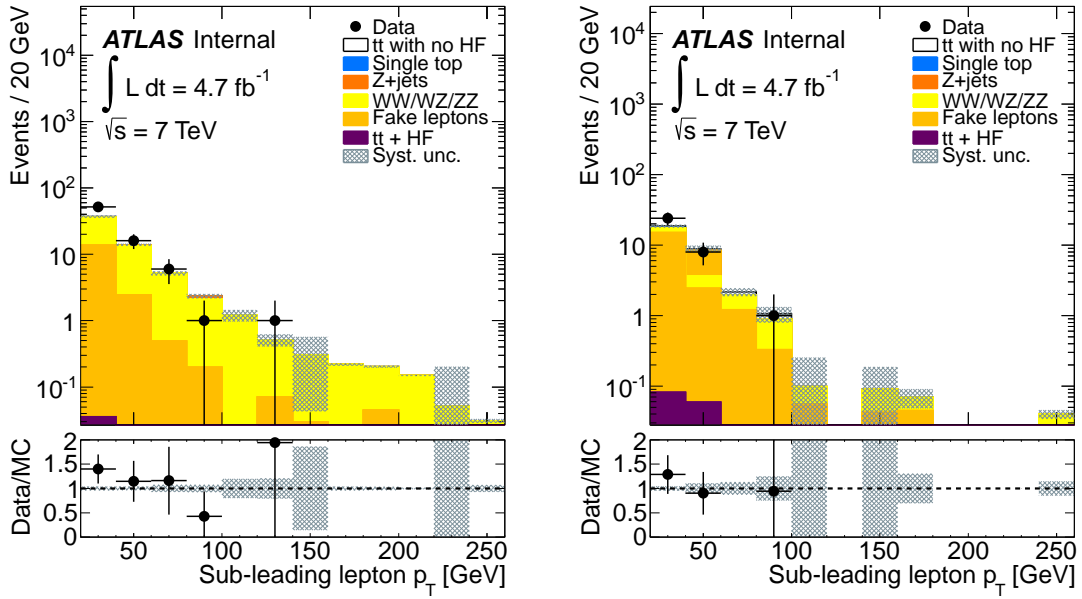
(a) 0 tags

(b) 1 tag



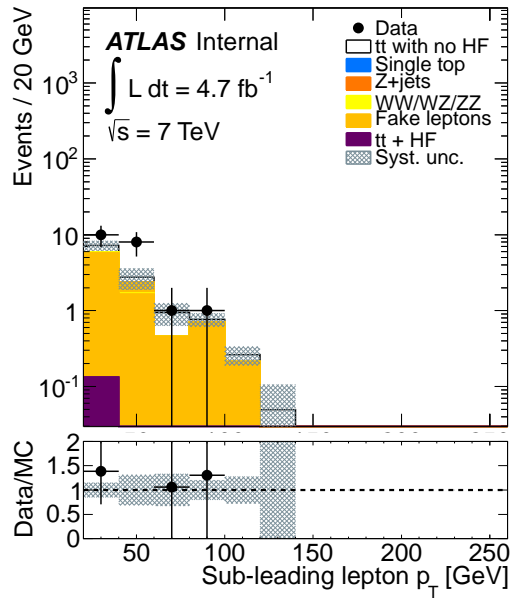
(c) 2 tags

Figure 37: Leading lepton p_T observed using the same-sign dilepton $t\bar{t}$ event selection and 0 (a), 1 (b), or 2 (c) tagged jets. Statistical uncertainties are included on the data, while systematic error bands are included on the total prediction.



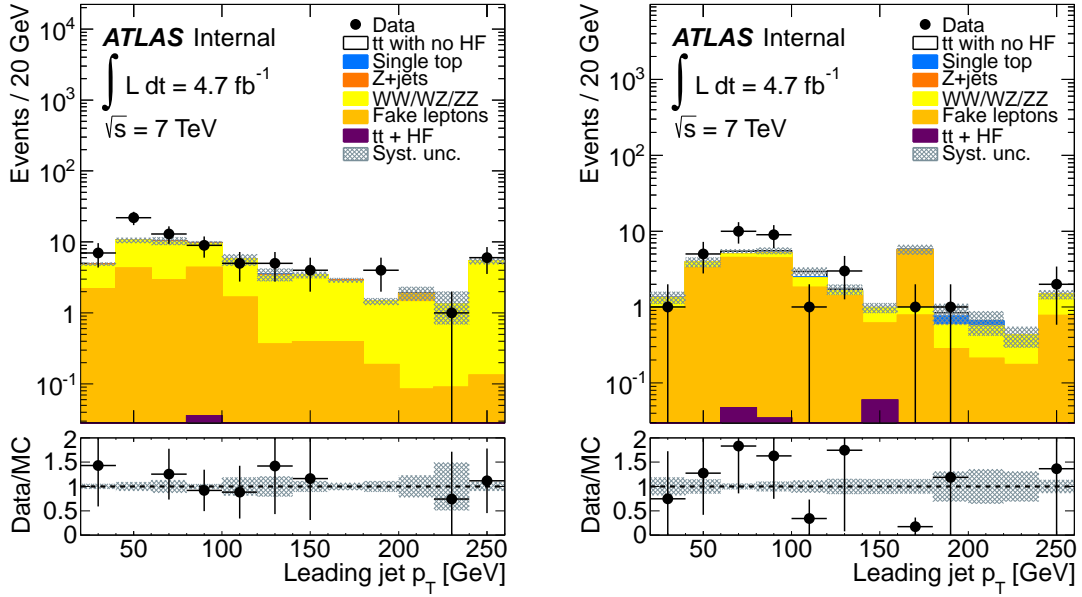
(a) 0 tags

(b) 1 tag



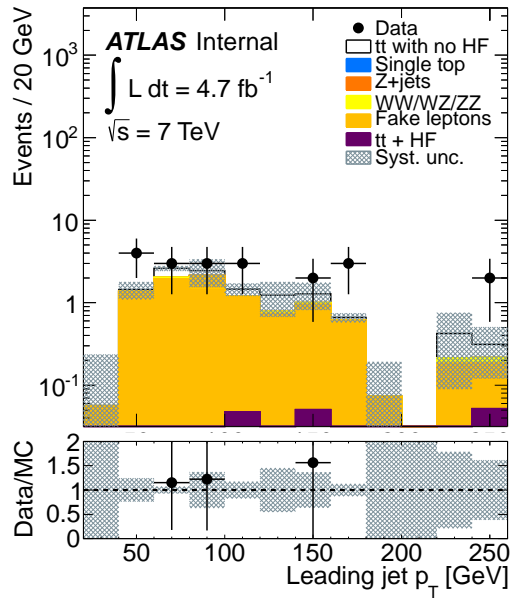
(c) 2 tags

Figure 38: Sub-leading lepton p_T observed using the same-sign dilepton $t\bar{t}$ event selection and 0 (a), 1 (b), or 2 (c) tagged jets. Statistical uncertainties are included on the data, while systematic error bands are included on the total prediction.



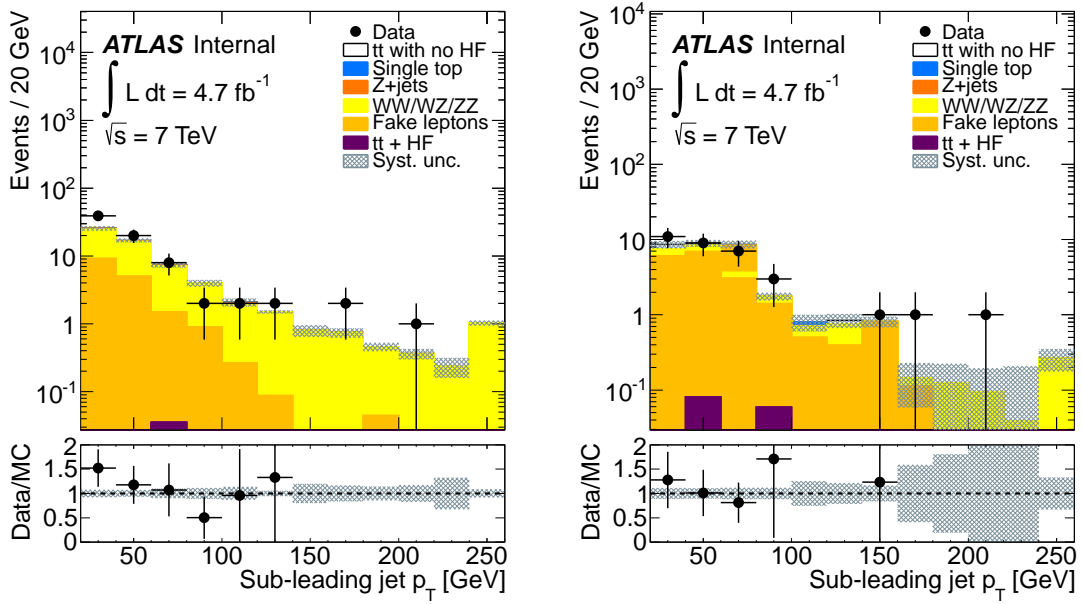
(a) 0 tags

(b) 1 tag



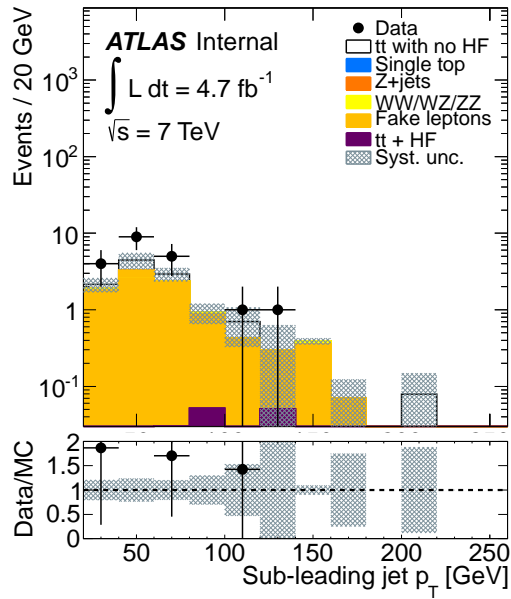
(c) 2 tags

Figure 39: Leading jet p_T observed using the same-sign dilepton $t\bar{t}$ event selection and 0 (a), 1 (b), or 2 (c) tagged jets. Statistical uncertainties are included on the data, while systematic error bands are included on the total prediction.



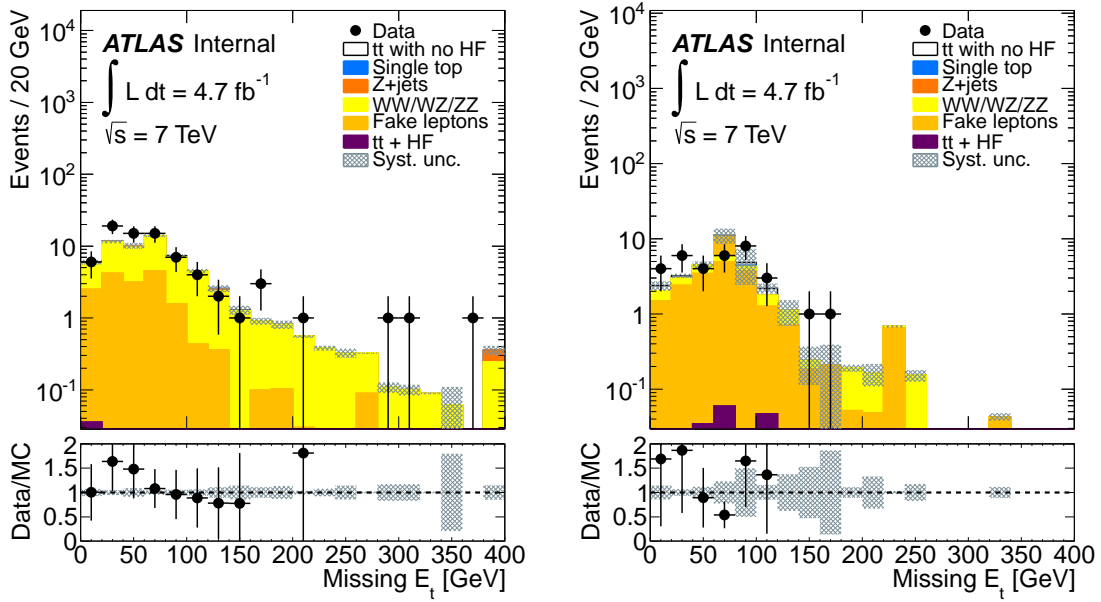
(a) 0 tags

(b) 1 tag



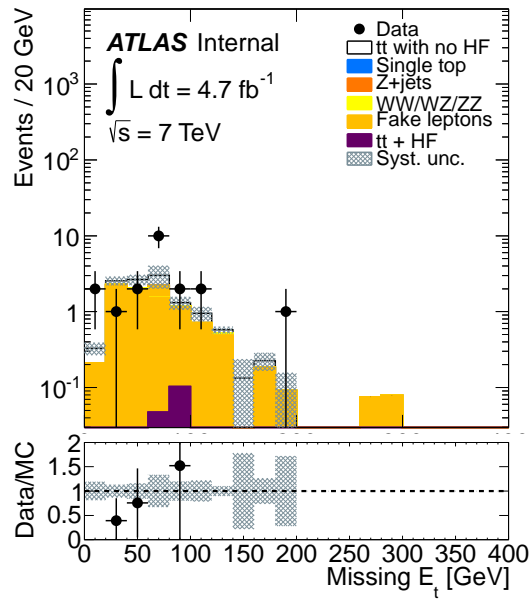
(c) 2 tags

Figure 40: Sub-leading jet p_T observed using the same-sign dilepton $t\bar{t}$ event selection and 0 (a), 1 (b), or 2 (c) tagged jets. Statistical uncertainties are included on the data, while systematic error bands are included on the total prediction.



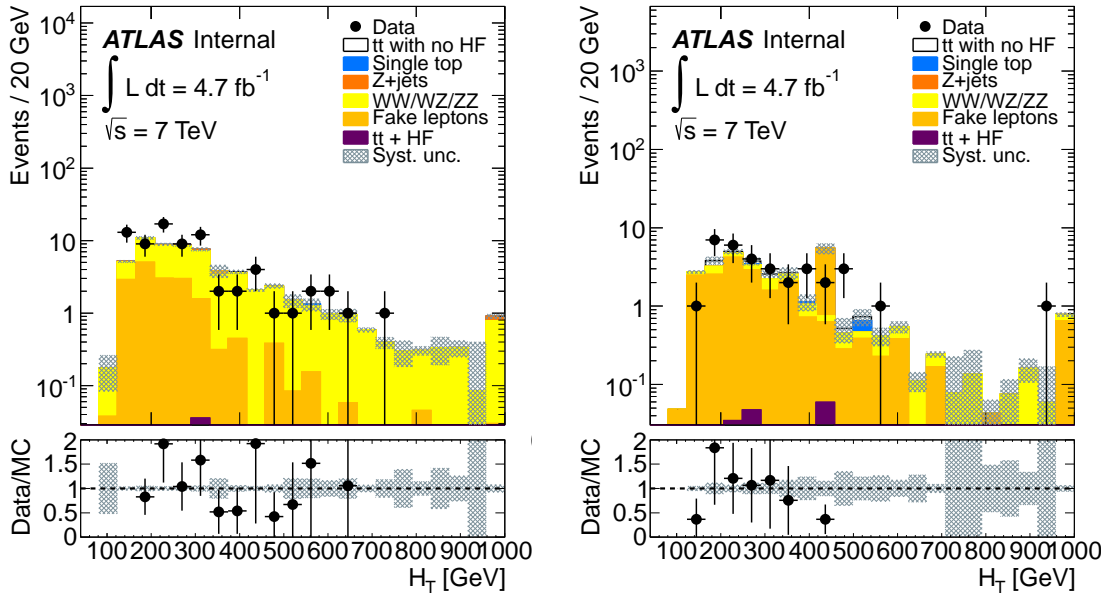
(a) 0 tags

(b) 1 tag



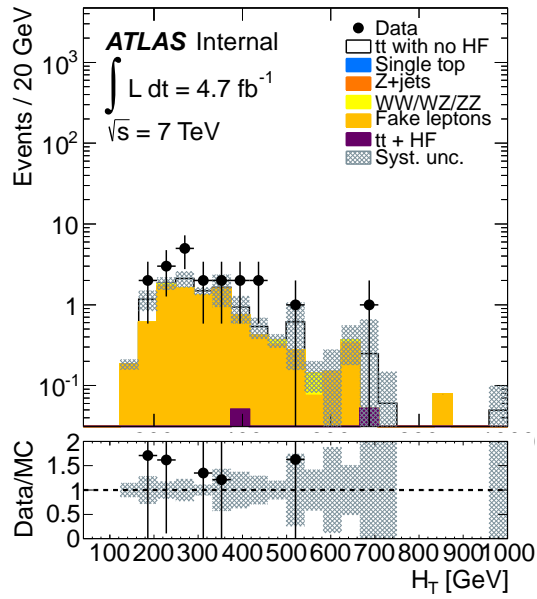
(c) 2 tags

Figure 41: E_T^{miss} observed using the same-sign dilepton $t\bar{t}$ event selection and 0 (a), 1 (b), or 2 (c) tagged jets. Statistical uncertainties are included on the data, while systematic error bands are included on the total prediction.



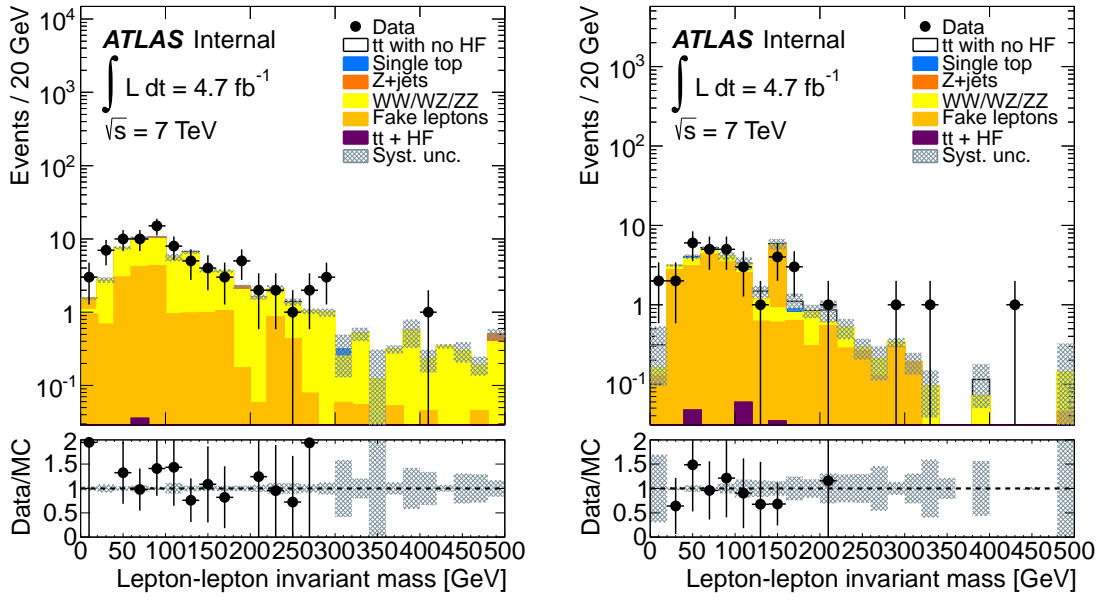
(a) 0 tags

(b) 1 tag



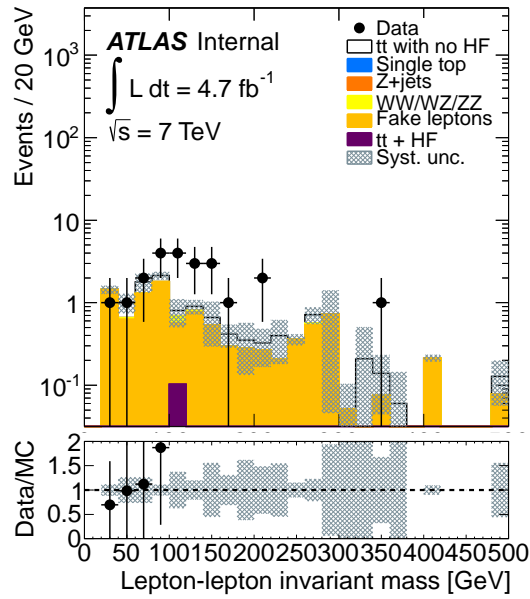
(c) 2 tags

Figure 42: H_T observed using the same-sign dilepton $t\bar{t}$ event selection and 0 (a), 1 (b), or 2 (c) tagged jets. Statistical uncertainties are included on the data, while systematic error bands are included on the total prediction.



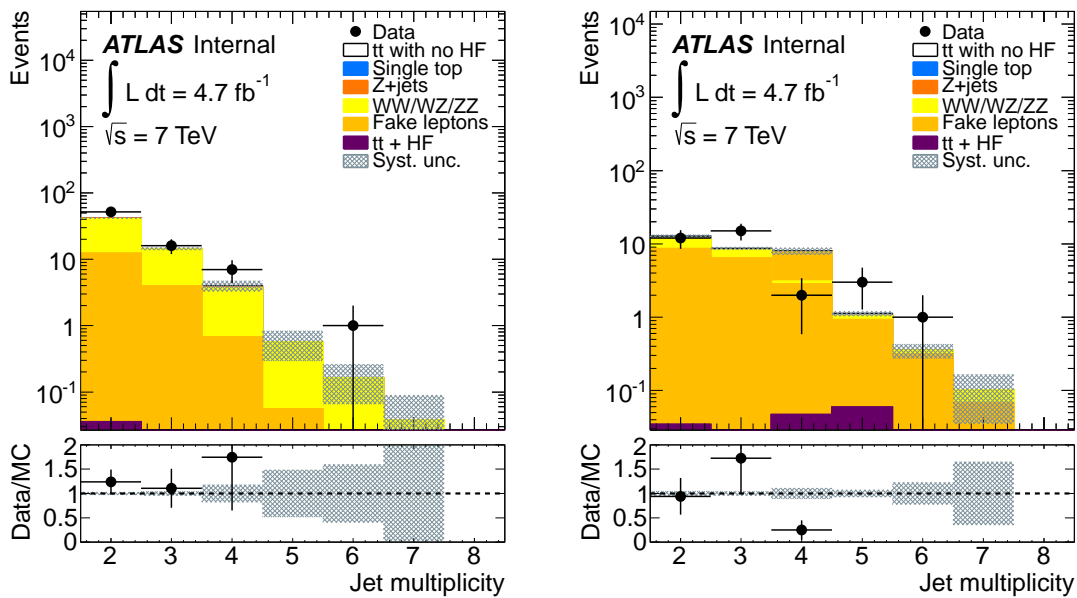
(a) 0 tags

(b) 1 tag



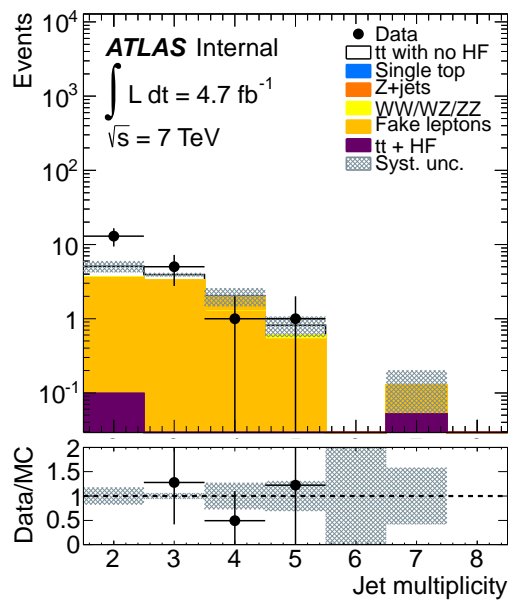
(c) 2 tags

Figure 43: Lepton-lepton invariant mass observed using the same-sign dilepton $t\bar{t}$ event selection and 0 (a), 1 (b), or 2 (c) tagged jets. Statistical uncertainties are included on the data, while systematic error bands are included on the total prediction.



(a) 0 tags

(b) 1 tag



(c) 2 tags

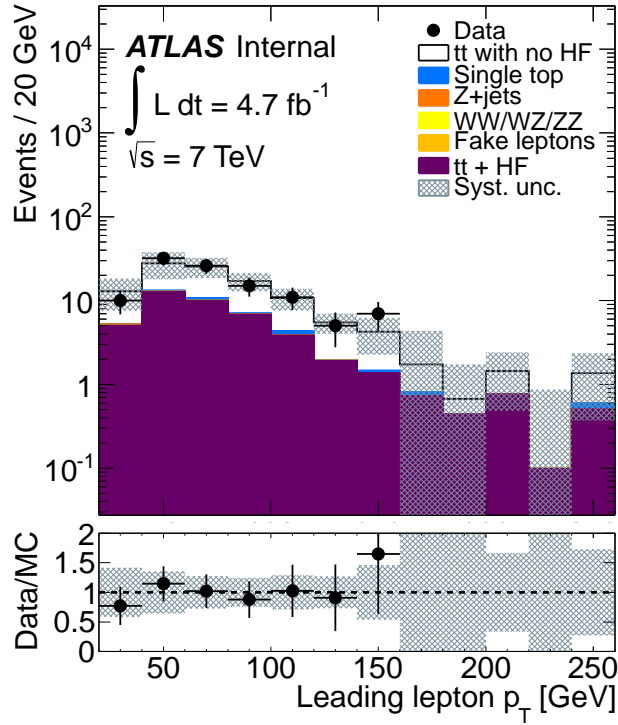
Figure 44: Selected jet multiplicities observed using the same-sign dilepton $t\bar{t}$ event selection and 0 (a), 1 (b), or 2 (c) tagged jets. Statistical uncertainties are included on the data, while systematic error bands are included on the total prediction.

8.5 Signal region

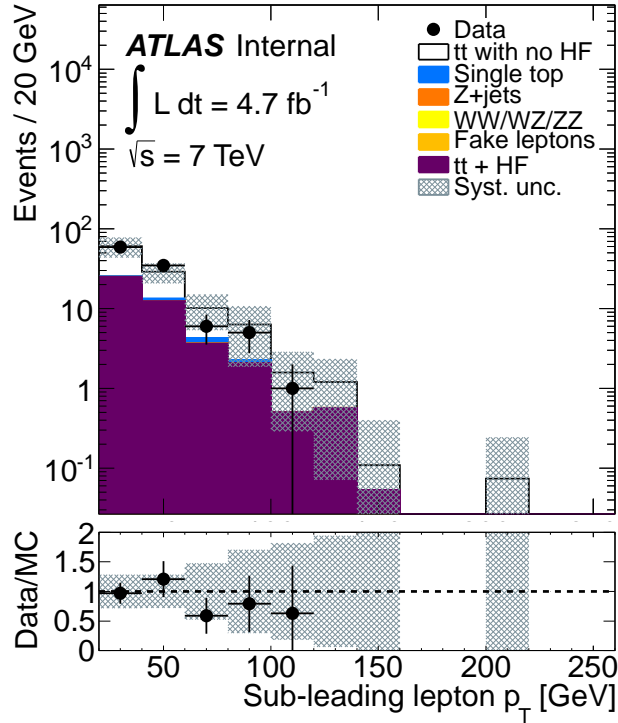
Process	ee yield	$\mu\mu$ yield	$e\mu$ yield
$t\bar{t}$ + HF	0 ± 0	0 ± 0	0 ± 0
$t\bar{t}$ + LF	0 ± 0	0 ± 0	0 ± 0
Single top	0 ± 0	0 ± 0	0 ± 0
Z + jets	0 ± 0	0 ± 0	0 ± 0
WW,WZ,ZZ	0 ± 0	0 ± 0	0 ± 0
MC fakes	0 ± 0	0 ± 0	0.1 ± 0.1
Total expectation	$0 \pm 0 \pm 0$	$0 \pm 0 \pm 0$	$0.1 \pm 0.1 \pm 0.2$
Data	0	0	0

Table 15: Event yield expected in 4.7 fb^{-1} in same-sign dilepton events with three or more b -tagged jets. Uncertainties on individual components are statistical only. For the final estimate, systematics are included (listed second).

In this section, we present the predicted and observed yield for events in the signal region used to measure $t\bar{t}$ + HF. As first described in Chapter 5, the signal region for $t\bar{t}$ + HF is defined as those events passing the baseline $t\bar{t}$ dilepton selection with the additional requirement of three or more tagged jets. As shown in Table 15, no same-sign events are observed in events with three or more tagged jets, so the total fake prediction for the signal region is 0. The predicted yield of events is presented in Table 16, and select kinematic distributions are shown in Figures 45 - 48.

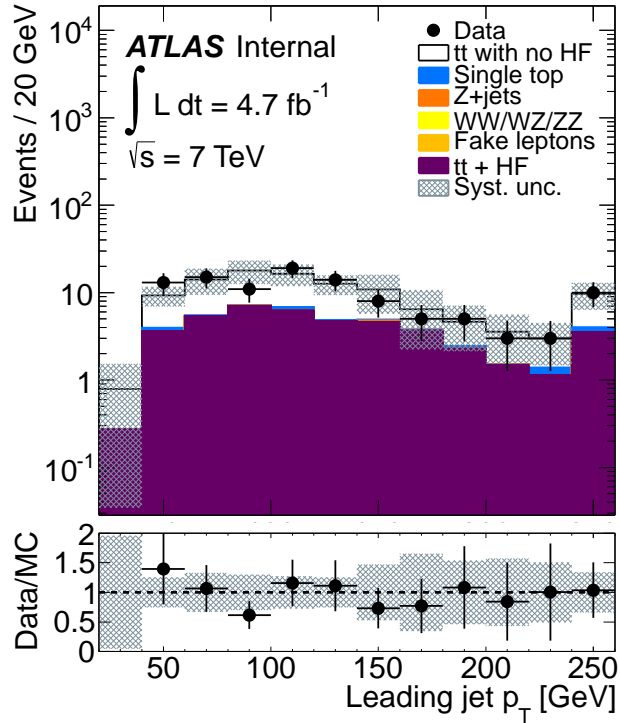


(a) Leading lepton p_T

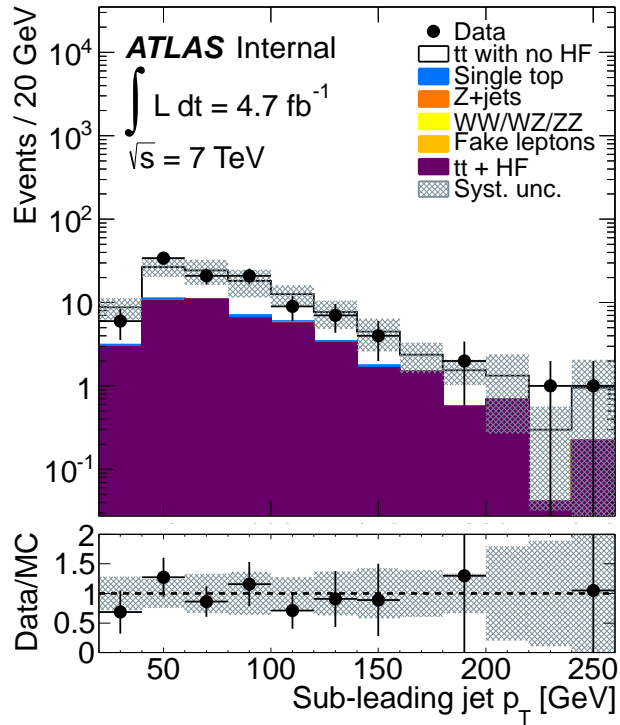


(b) Sub-leading lepton p_T

Figure 45: Leading (a) and sub-leading (b) lepton p_T observed using the dilepton $t\bar{t}$ event selection and 3 or more tagged jets.

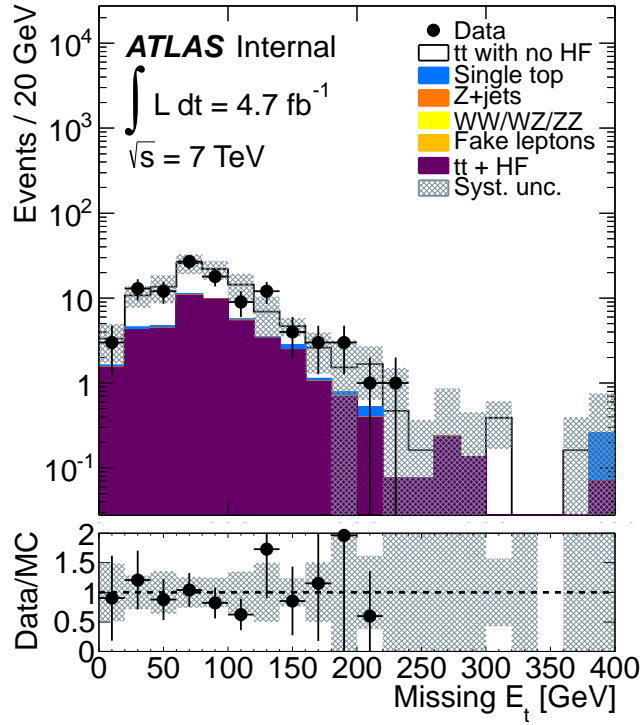


(a) Leading jet p_T

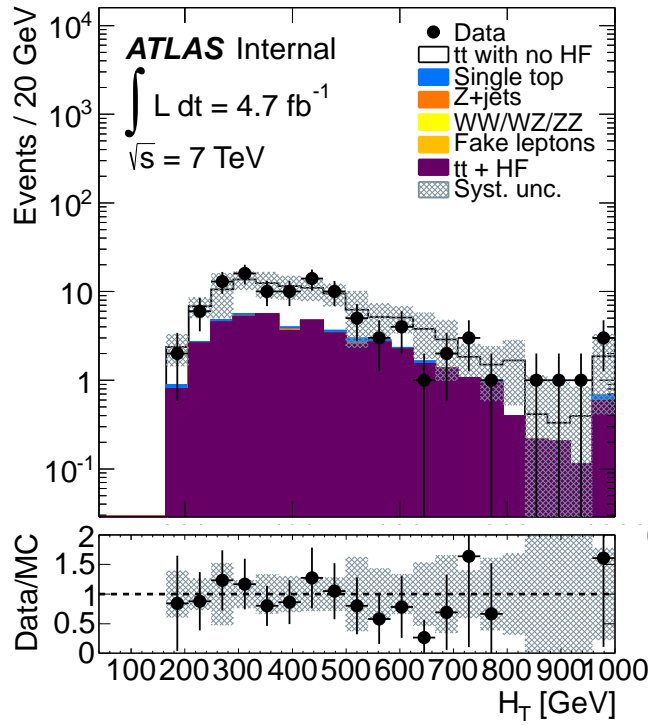


(b) Sub-leading jet p_T

Figure 46: Leading (a) and sub-leading (b) jet p_T observed using the dilepton $t\bar{t}$ event selection and 3 or more tagged jets.

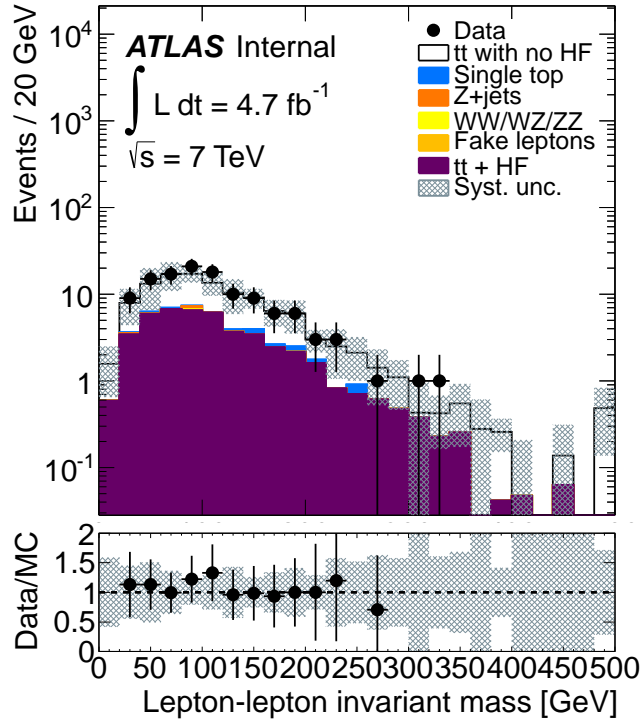


(a) E_T^{miss}

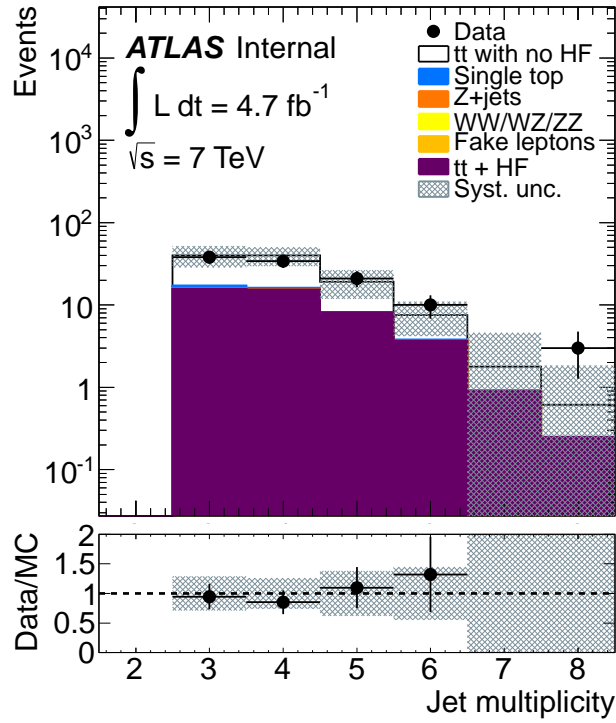


(b) H_T

Figure 47: E_T^{miss} (a) and H_T (b) observed using the dilepton $t\bar{t}$ event selection and 3 or more tagged jets.



(a) $M_{\ell\ell}$



(b) N_{jets}

Figure 48: Lepton-lepton invariant mass (a) and selected jet multiplicity (b) observed using the dilepton $t\bar{t}$ event selection and 3 or more tagged jets.

Process	ee yield	$\mu\mu$ yield	$e\mu$ yield
$t\bar{t}$ + HF	4.6 ± 0.6	10.6 ± 0.9	28.8 ± 1.4
$t\bar{t}$ + LF	6.6 ± 0.9	15.3 ± 1.4	40.7 ± 2.4
Single top	0.3 ± 0.2	0.3 ± 0.2	1.5 ± 0.4
Z + jets	0.1 ± 0.1	0 ± 0	0 ± 0
WW,WZ,ZZ	0 ± 0	0 ± 0	0 ± 0
RSS fakes	0 ± 1.7	0 ± 1.5	0 ± 1.6
Total expectation	$11.7 \pm 1.7 \pm 4.3$	$26.4 \pm 2 \pm 8.2$	$71.1 \pm 3 \pm 25.9$
Data	11	24	71

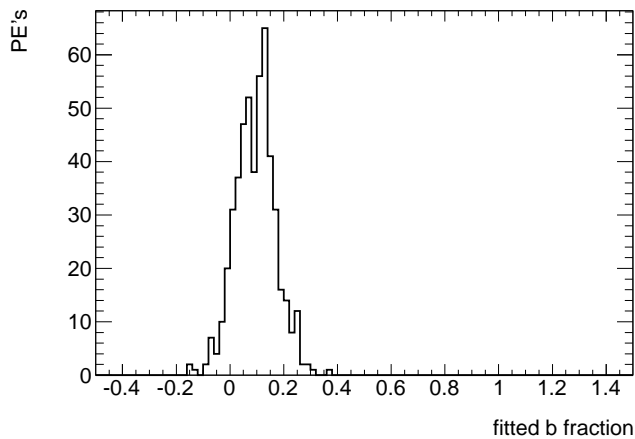
Table 16: Event yield expected in 4.7 fb^{-1} in opposite-sign dilepton events with three or more b -tagged jets. Uncertainties on individual components are statistical only. For the final estimate, systematics are included (listed second).

8.6 Fit results

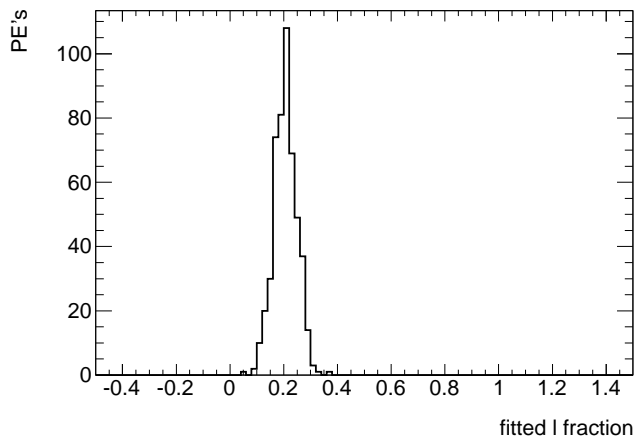
Fit parameter	Average fit value	Average fit error
b_e	0.09 ± 0.07	0.07 ± 0.00
light	0.20 ± 0.04	0.04 ± 0.00

Table 17: The expected fit results for the fraction of b_e and light-flavor jets. Using Monte Carlo, 500 pseudo-experiments are performed, each assuming an integrated luminosity of 4.7 fb^{-1} .

In this section, we present the expected fit results for the flavor composition of tagged jets in our signal region. 500 pseudo-experiments are drawn from the Monte Carlo, and the fitter is used to extract the fraction of b_e and light jets. In each pseudo-experiment, we assume an integrated luminosity of 4.7 fb^{-1} . The distribution of output fit values is shown in Figure 49, and the output fit errors are shown in Figure 50. A summary is found in Table 17.

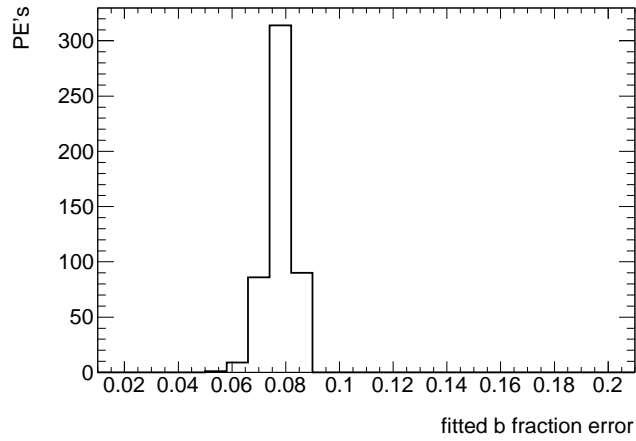


(a) Fraction of b_e jets

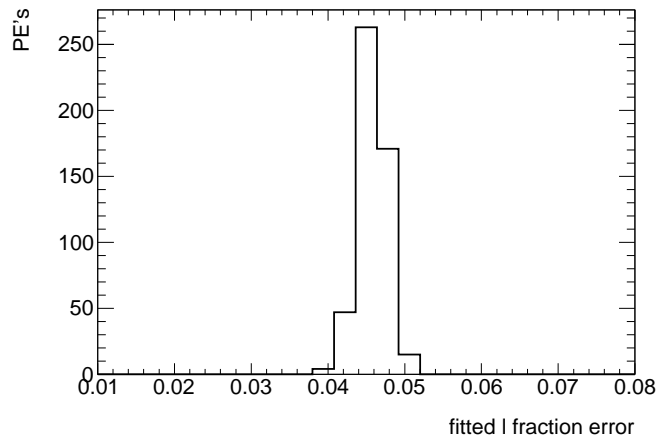


(b) Fraction of light jets

Figure 49: The expected fit value, derived from pseudo-experiments, for the fraction of extra b (a) and light (b) jets in our signal region. The input b_e fraction is 0.094, and the input light fraction is 0.204. The fit is normalized to 4.7 fb^{-1} .



(a) Fraction of b_e jets



(b) Fraction of light jets

Figure 50: The expected error, derived from pseudo-experiments, for the fraction of extra b (a) and light (b) jets in our signal region. The fit is normalized to 4.7 fb^{-1} .

9 Results

In this chapter, we present the fit result using 4.7 fb^{-1} of data, and the calculation of $\sigma_{\text{fid}}(t\bar{t} + \text{HF})$ and $\sigma_{\text{fid}}(t\bar{t} + \text{j})$. These fiducial cross-sections are used to calculate the ratio R_{HF} which is the primary analysis goal for this thesis.

The fit performed using the full 2011 data set is presented in Section 9.1. The fitted fraction of light jets in the signal region is used to calculate $\sigma_{\text{fid}}(t\bar{t} + \text{HF})$. As described in Chapter 7, we use the fit result for the fraction of additional b -jets to assess the systematic uncertainty on the flavor composition of events in the true fiducial volume. The details of this calculation are given in Section 9.2.

Finally, a discussion of the results are presented, as well as thoughts on how the result may be used to inform future measurements.

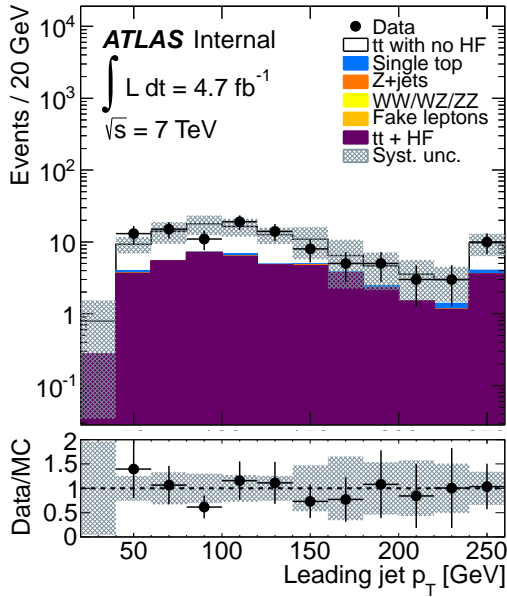
9.1 Signal region fit

As described in Chapter 5, the signal region for this analysis is defined by events passing the dilepton $t\bar{t}$ selection criteria with the additional requirement of at least three b -tagged jets. All good quality data from the 2011 run period are included in this analysis, leading to a total integrated luminosity of 4.7 fb^{-1} . Using MC and the RSS method, we expect 109.2 ± 4.1 (stat) ± 32.8 (syst.) events, which is in good agreement with the observed number of 106 events, as detailed in Section 8.5. In the 109.2 events we expect 335 b -tagged jets, 105.0 ± 3.5 (stat) 3-tagged events and 4.9 ± 0.6 (stat) 4-tagged events. In the 106 events we observe a total of 325 b tags, 99 3-tagged events and 7 4-tagged events, both in good agreement with predictions. Jet p_{T} and vertex mass distributions for jets in the signal region are compared

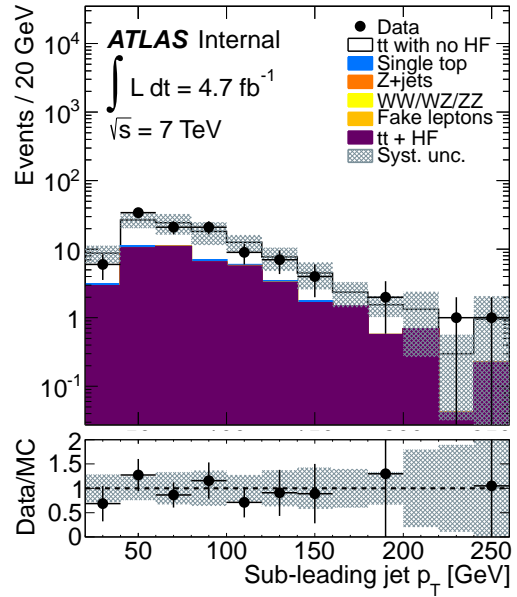
in Figures 51 and 52.

A fit to the vertex mass distribution of the b -tagged jets in this region is performed to extract the flavor composition of these jets. As described in Chapter 6, we fix the normalization for the b_t template to be twice the number of events to reduce the number of floating parameters in the fit. This means 212 of the observed 325 b -tags are assumed to come from $t \rightarrow Wb$ process, in agreement with the Monte Carlo prediction. We use the Monte Carlo to constrain the number of b -tags from background events to be 8.1 ± 1.3 (stat). Thus the background-subtracted number of extra b -tags is 104.9 ± 1.3 (stat).

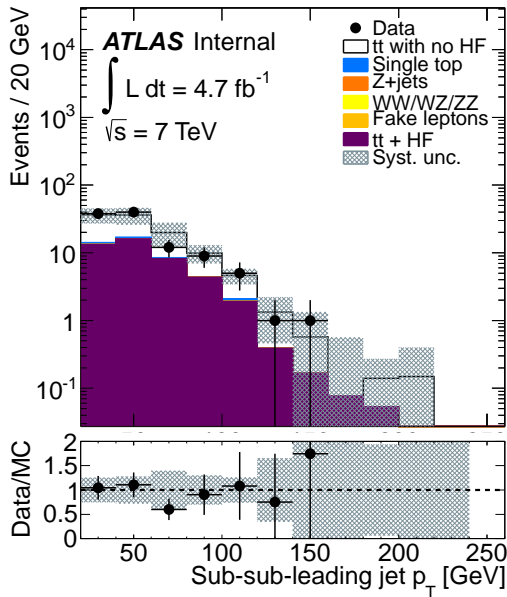
The simultaneous fit result for the three b -tag quality bins is shown in Figure 53. The extracted values for the fraction of b_e and light jets are shown in Table 18, and compared with the expected results from Monte Carlo pseudo-experiments. The fitted fraction of light b -tags implies an observation 78.7 ± 13.5 (stat) b -tagged HF jets (of the 104.9 extra b -tags). Using the fitted fraction of b_e , we interpret 85.0 ± 23.1 of the 78.7 HF jets as coming from c .



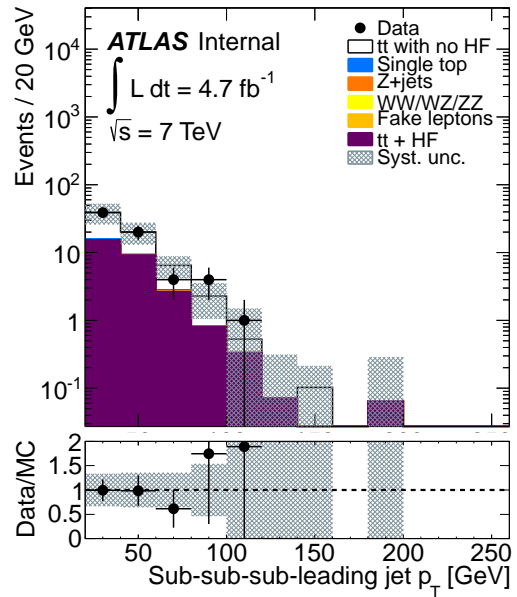
(a) Leading jet



(b) Sub-leading jet

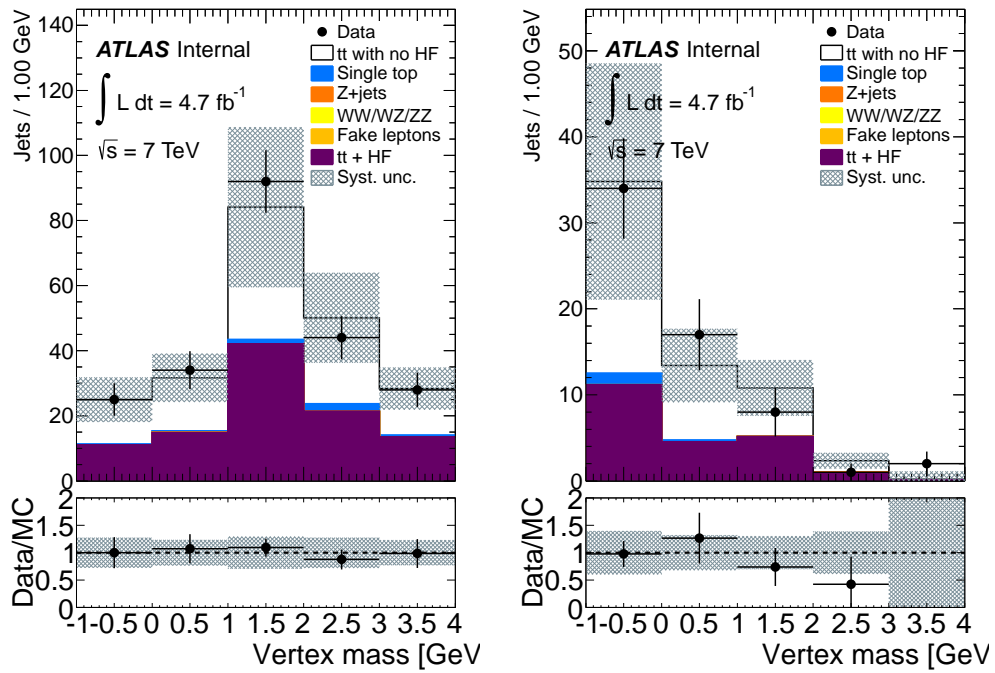


(c) Sub-sub leading jet



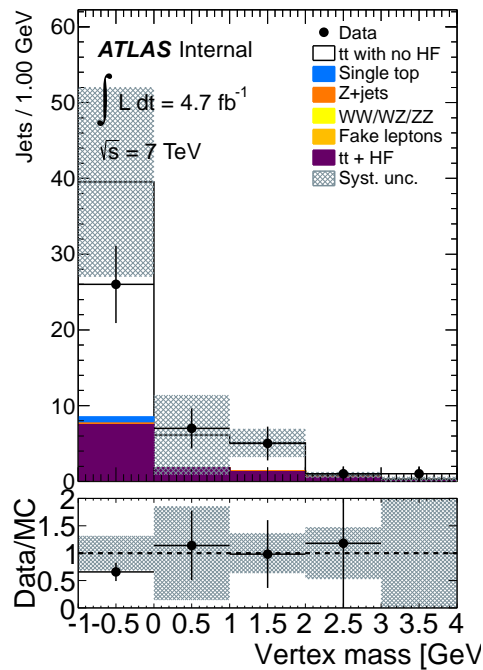
(d) Sub-sub-sub leading jet

Figure 51: Transverse momentum of the leading (a), sub-leading (b), sub-sub-leading (c), and sub-sub-sub-leading (d) jets.



(a) High quality tags

(b) Medium quality tags



(c) Low quality tags

Figure 52: Comparison of data and MC for the vertex mass of b -tagged jets in the signal region. Jets tagged above the 60% efficiency point (a), jets tagged between the 60 and 70% efficiency points (b), and jets tagged between the 70 and 75% efficiency points (c) are shown separately.

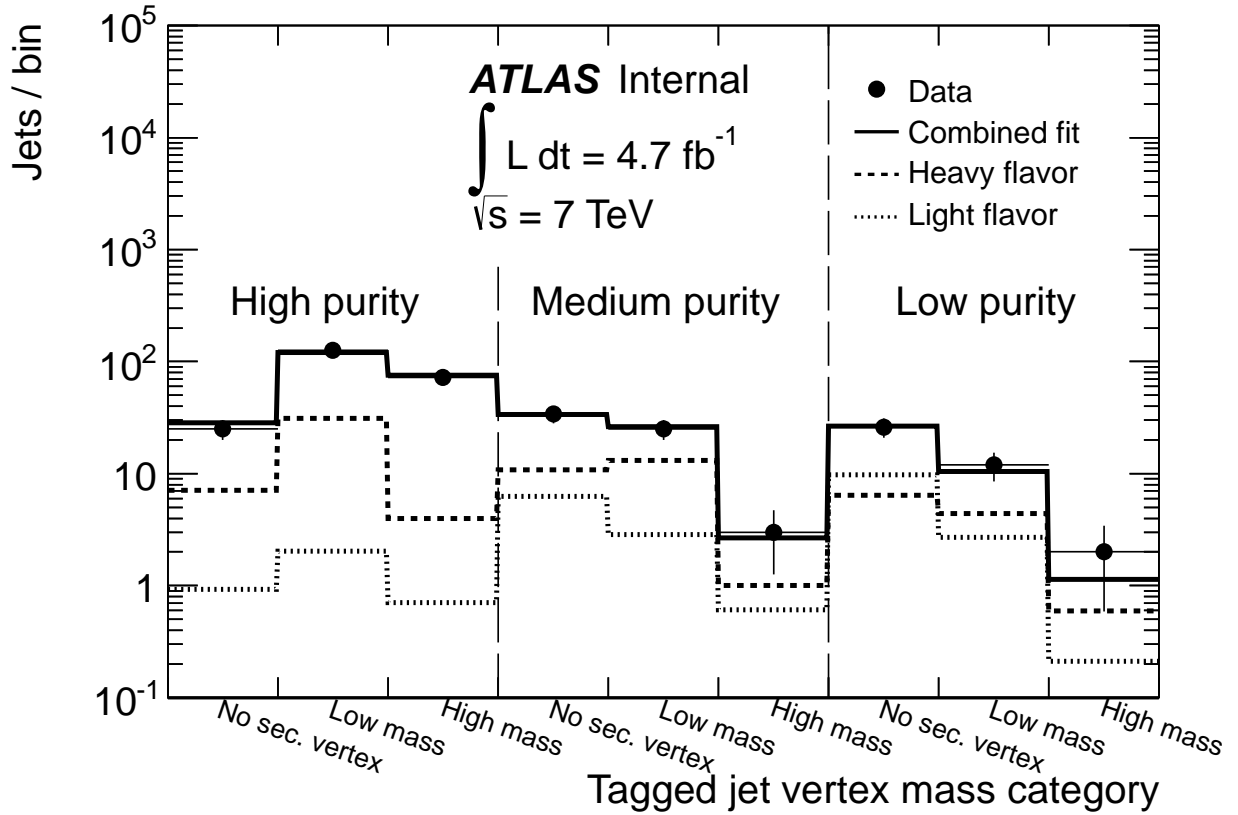


Figure 53: The best fit result for the measurement of R_{HF} is shown. Data and the best fit template are shown, with separate contributions from extra heavy ($b_e + c$) flavor and light flavor jets. The fit result is shown simultaneously for all three bins of MV1 weight. The first MV1 bin (‘High quality’) corresponds to jets b -tagged above the 60% efficiency point. The second MV1 bin (‘Medium quality’) contain jets between the 60% and 70% efficiency points. The third MV1 bin (‘Low quality’) contain jets b -tagged between the 70% and 75% efficiency points.

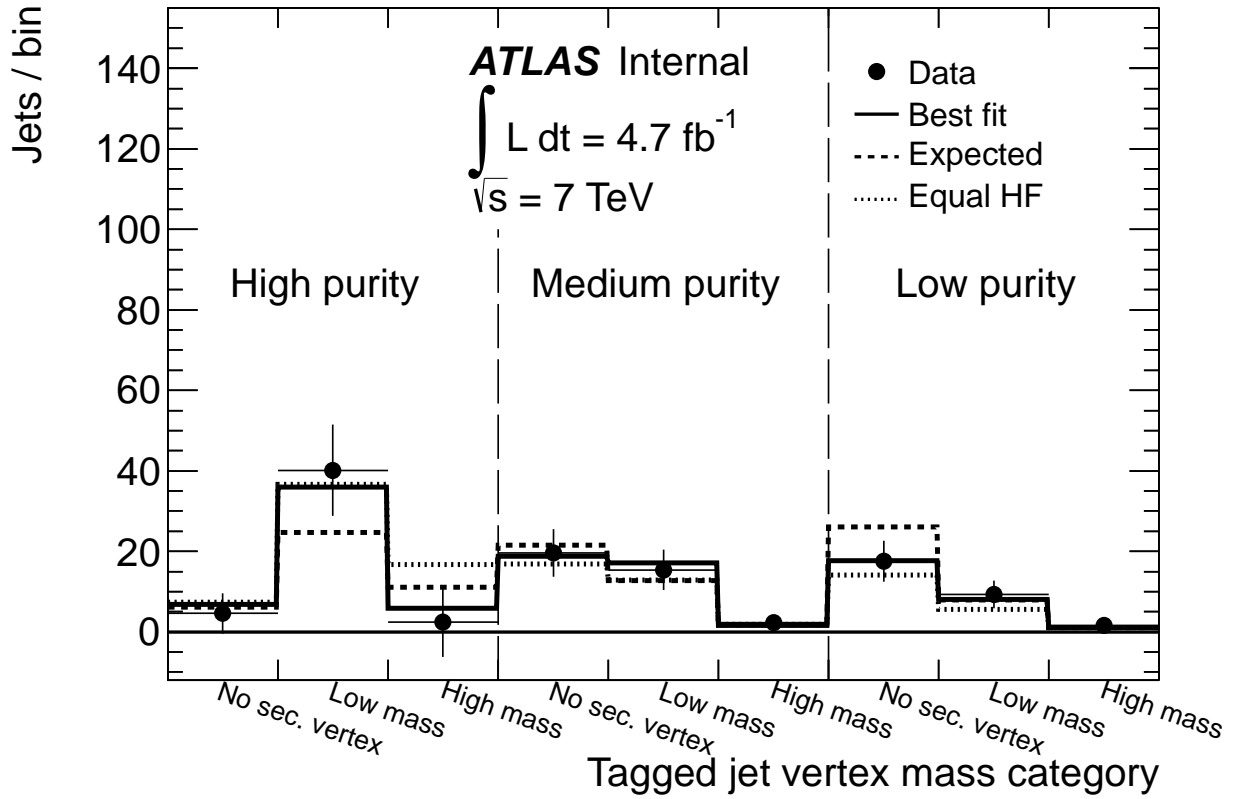


Figure 54: Combined fit templates are compared for three different combinations of fit parameters: the values preferred by data (‘Best fit’), the values expected from MC pseudo-experiments (‘Expected’), and values consistent with the MC expectation for the fraction of b_e jets in the HF sample but with the observed value for the total HF fraction (‘Equal HF’). The expected contribution for b_t is subtracted to highlight the relevant piece of the fit result.

Parameter	Fit result	Expectation from PE's
b_e	$(-1.8 \pm 7.1) \%$	$(9 \pm 7) \%$
Light	$(8.0 \pm 4.2) \%$	$(20 \pm 4) \%$

Table 18: Fitted value for the fraction of b -tagged b_e and light jets in the signal region, using 4.7 fb^{-1} of data. Expectation from pseudo-experiments (= PE's) are included for reference.

A natural question to ask is why the fitted fraction of c -jets is so much higher than expected. To investigate this, we compare the data with a weighted sum of templates, assuming different b_e , c , and light fractions. In Figure 54, the same fit result is shown, with the expected contribution from b_t subtracted off. Two other possible fit templates are shown. In the first, the fraction of b_e and light jets are taken directly from the Monte Carlo. In the second, the fraction of light jets is taken from the best fit result, but the fraction of b_e jets is changed such that the fit can be interpreted as predicting equal numbers of b_e and c -jets. As can be seen, these two hypotheses are clearly disfavored by the data, indicating the best fit result does indeed offer the best explanation for what is observed.

For the measurement of $\sigma_{\text{fid}}(t\bar{t} + \text{j})$, the quantity measured in the data is the yield of $t\bar{t}$ candidate events with at least three jets, at least two of which are b -tagged. There are three principle backgrounds to consider: events with a fake lepton, events which do not contain a $t\bar{t}$ pair, and events with a $t\bar{t}$ pair with b -tagged jets from light flavor jets. In the data, 1656 events are observed with at least three jets, and at least two b -tagged jets. The total background estimate is found to be 112.1 ± 3.9 (stat.), leading a background subtracted yield of 1543.9 ± 3.9 (stat.).

9.2 Acceptance calculation

As described in Section 7.9, an important piece of the calculation of systematic uncertainty for this analysis is related to the fraction of generated $t\bar{t} + \text{HF}$ events which contain extra b jets ($f_{b/\text{HF}}$). Using reconstruction efficiencies for $t\bar{t} + b$ and $t\bar{t} + c$ events measured in the Monte Carlo, we can convert the number of observed $t\bar{t} + b$ and $t\bar{t} + c$ events into the number of produced $t\bar{t} + b$ and $t\bar{t} + c$ events. The number of $t\bar{t} + b$ events can be measured using the fitted value for the fraction of b_e jets, and the number of c jets is taken as the difference between the total number of HF b -tags and the fitted number of b_e jets.

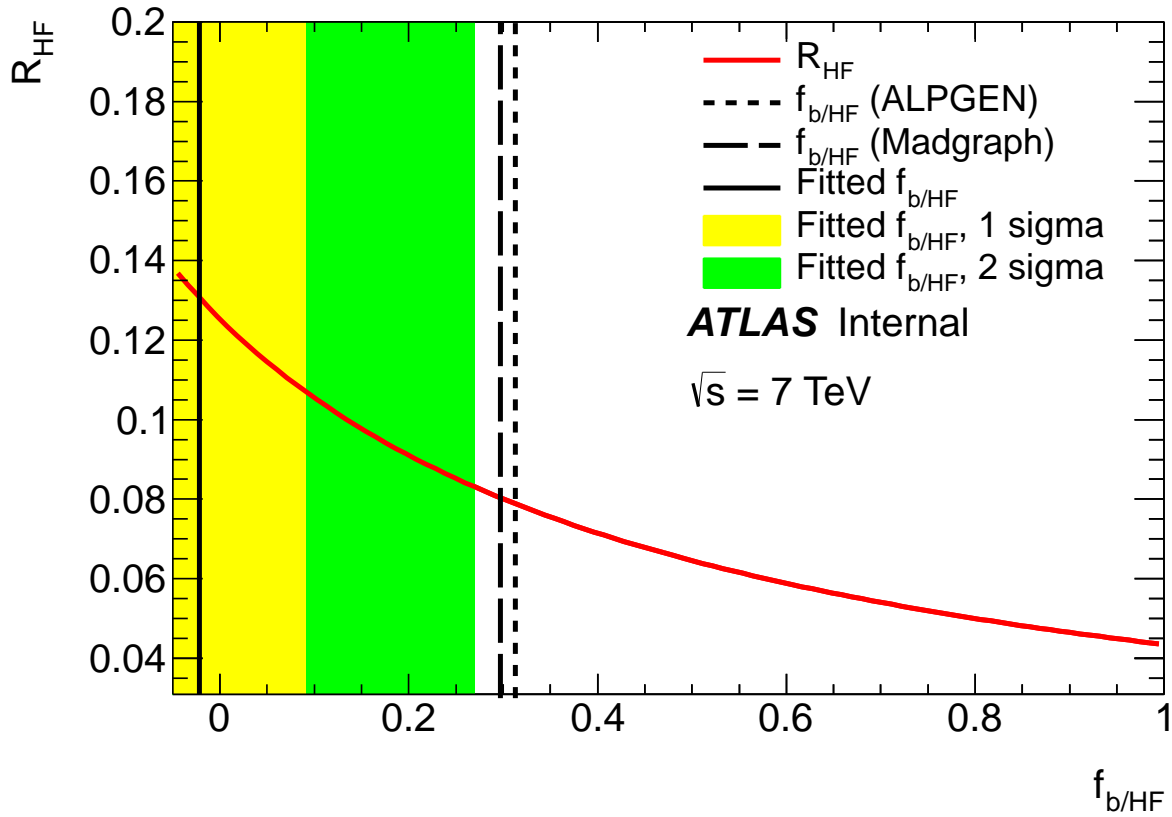


Figure 55: The extracted value of R_{HF} as a function of the fraction of extra HF b -tags that are due to b -quarks in the fiducial volume (referred to as ' $f_{b/HF}$ '). The value of $f_{b/HF}$ predicted by ALPGEN and MADGRAPH are indicated for reference. Also shown is the fit result for the $f_{b/HF}$ (solid vertical black line) and 1 sigma (yellow) and 2 sigma (green) bands. The fit result for $f_{b/HF}$ is consistent with the simulated values on the order of 2.1-2.2 sigma.

In Figure 55, the value of R_{HF} is plotted as a function of $f_{b/HF}$, assuming only changes in the fiducial acceptance factor used in the calculation of $\sigma_{\text{fid}}(t\bar{t} + \text{HF})$. The value of $f_{b/HF}$ as predicted in two Monte Carlo generators is compared to the fitted value. Using the statistical uncertainty on the fit result, it is observed that the fitted value for $f_{b/HF}$ is consistent with the predicted values on the order of 2.1-2.2 sigma. Given this relatively poor statistical significance, it is decided that the most appropriate course of action is to quote R_{HF} using the value of $f_{b/HF}$ from the Monte Carlo. We do, however, quote an asymmetric systematic uncertainty on R_{HF} that covers at one sigma the variation in R_{HF} when the fitted value for $f_{b/HF}$ is used in place of the value measured in the Monte Carlo.

9.3 Fiducial cross-sections

As described in chapter 6, the measurement of R_{HF} is accomplished in two steps. In the first, we compute the fiducial cross-section for $t\bar{t} + \text{HF}$ using the fitted number of extra HF jets in events with three or more b -tagged jets. Next, the fiducial cross-section for $t\bar{t}$ is computed using the number of events with three or more jets and two or more b -tags. For the measurement of $\sigma_{\text{fid}}(t\bar{t} + \text{HF})$, the contribution from background events is explicitly handled by the fit. For the measurement of $\sigma_{\text{fid}}(t\bar{t} + j)$, there is a small contribution to the observed number of events coming from background sources. Monte Carlo is used to subtract this background. A summary of these quantities is shown in Table 19.

Systematic uncertainties on the measurement of R_{HF} are summarized in Table 20. The final measurement of R_{HF} is compared with the value predicted by Monte Carlo in Table 21. The measurement of $\sigma_{\text{fid}}(t\bar{t} + \text{HF})$ is found to be 0.24 ± 0.04 (stat.) pb, compared

Process	Measured quantity	Fiducial acceptance factor	Fiducial cross-section (pb)
$t\bar{t} + \text{HF}$	78.7 ± 13.6 (extra HF jets)	0.070 ± 0.004	0.24 ± 0.04
$t\bar{t} + \text{jet}$	1543.9 ± 3.9 (events)	0.108 ± 0.001	3.03 ± 0.08

Table 19: A summary of the measured quantities and fiducial acceptance factors used to calculate the fiducial cross-sections. For $\sigma_{\text{fid}}(t\bar{t} + \text{HF})$, the measured quantity is a fitted number of extra HF jets in events with three or more b -tagged jets. For $\sigma_{\text{fid}}(t\bar{t} + \text{j})$, the measured quantity is an event yield for events with three or more jets, at least two of which are b -tagged, after background-subtraction.

to a prediction from ALPGEN and HERWIG of 0.14 pb. $\sigma_{\text{fid}}(t\bar{t} + \text{j})$ is measured to be 3.04 ± 0.08 (stat.), compared to a prediction of 3.37 pb from ALPGEN and HERWIG. Using these cross-sections, the value for R_{HF} is found to be 7.9 ± 1.4 (stat.) $^{+5.5}_{-2.1}$ (syst.)%, as compared with the prediction from Monte Carlo of 4.1 ± 1.3 (syst.) %. Taking into account all uncertainties, the measured value for R_{HF} is consistent with the prediction at the level of 1.3 times the total uncertainty.

Source	% (full calculation)	% (acceptance calculation)
Jet energy resolution	2.6	2.7
Jet energy scale	9	2.9
e reconstruction	0.2	0.2
μ reconstruction	0.0	0.1
Tagging efficiency for b jets	3.2	2.6
Tagging efficiency for c jets	21.4	5.7
Tagging efficiency for light jets	8.4	0.2
Jet vertex fraction identification	1.3	0.0
RSS	3.4	0.0
E_T^{miss} reconstruction	0.9	0.5
Parton shower modeling	2.7	8.6
Generator variation	5.7	2.3
Initial and final state radiation	2.5	2.3
PDF uncertainties	2.4	0.6
Top template composition	1.5	–
Top template shape	5.4	–
Top template normalization	1.0	–
Extra b template shape	3.3	–
Fiducial flavor composition	+64.6 –0.0	+64.6 –0.0
Total systematic	+70.0 –27.2	+65.7 –12.0

Table 20: A breakdown of systematic errors on the measured value of R_{HF} is shown. All variations are calculated by consistently propagating variations through the fit and acceptance calculation. The systematic associated with the acceptance calculation by itself is included for a reference.

Quantity	MC expectation	Fitted value
$\sigma(t\bar{t} + \text{HF})$	0.14 ± 0.02 (stat) pb	0.24 ± 0.04 (stat) pb
$\sigma(t\bar{t} + \text{j})$	3.37 ± 0.09 (stat) pb	3.03 ± 0.08 (stat) pb
R_{HF}	(4.1 ± 1.3) %	$(7.9 \pm 1.4$ (stat.) $^{+5.5}_{-2.1}$ (sys.))%

Table 21: The final value for the ratio of fiducial cross-sections is presented, with full systematic uncertainties. The prediction for this ratio from Monte Carlo is shown as a point of comparison. The value for $\sigma_{\text{fid}}(t\bar{t} + \text{HF})$ and $\sigma_{\text{fid}}(t\bar{t} + \text{j})$ are included.

9.4 Conclusions

As described in Section 9.3, we extract the ratio of fiducial cross-sections for the production of $t\bar{t}$ events. Using a fit to the vertex mass of b -tagged jets in $t\bar{t}$ candidate events with three or more b -tagged jets, we find the fraction of light flavor b -tagged jets is $8.0 \pm 4.2\%$, compared to the predicted value of $20 \pm 4\%$. Using this fit result, we extract $\sigma_{\text{fid}}(t\bar{t} + \text{HF})$ to be 0.24 ± 0.04 pb (stat). Using a similar selection, we measure the fiducial cross-section for $t\bar{t}$ events with at least one extra jet to be 3.03 ± 0.08 (stat) pb. This leads to a value for the ratio of cross-sections, R_{HF} , of 7.9 ± 1.4 (stat.) $^{+5.5}_{-2.1}$ (syst.)%, compared with a leading-order prediction from Monte Carlo of 4.1 ± 1.3 (syst.)%. Once all uncertainties are taken into account, the measured value for R_{HF} is consistent with the prediction at the level of 1.3 times the total uncertainty.

Taken together, these two results show that the modeling of extra heavy-flavor content in $t\bar{t}$ events is essentially correct. The total production rate of extra heavy-flavor appears to be under-estimated in the Monte Carlo, but only by a small amount. The more significant mis-modeling appears to be in the relative rate of $t\bar{t} + b$ as compared to $t\bar{t} + c$. A number of similar studies conducted at ATLAS (looking for the associated production of $W + b$ [57]) and CMS (measuring $t\bar{t} + b\bar{b}$ [58]) are in agreement with our findings.

As described in Chapter 2, the $t\bar{t} + b\bar{b}$ final state is of particular importance for studies involving the Higgs boson ($t\bar{t} + H, H \rightarrow b\bar{b}$) and for a number of searches for physics beyond the Standard Model. It is hoped that the study presented in this thesis (or more likely an update to this study using statistics from the 8 TeV run of the LHC in 2012) can be used to better understand the backgrounds to these studies. Based on our findings, it appears that

data-driven methods for estimating the $t\bar{t} + b + X$ background would be advisable, unless new Monte Carlo is generated which better models this process.

References

- [1] A. Bredenstein, A. Denner, S. Dittmaier, and S. Pozzorini, *NLO QCD corrections to $pp \rightarrow t \text{ anti-}t b \text{ anti-}b + X$ at the LHC*, Phys.Rev.Lett. **103** (2009) 012002, arXiv:0905.0110 [hep-ph].
- [2] S. Dittmaier, P. Uwer, and S. Weinzierl, *NLO QCD corrections to $t \text{ anti-}t + \text{jet}$ production at hadron colliders*, Phys.Rev.Lett. **98** (2007) 262002, arXiv:hep-ph/0703120 [HEP-PH].
- [3] ATLAS Collaboration Collaboration, G. Aad et al., *Observation of a new particle in the search for the Standard Model Higgs boson with the ATLAS detector at the LHC*, Phys.Lett. **B716** (2012) 1–29, arXiv:1207.7214 [hep-ex].
- [4] CMS Collaboration Collaboration, S. Chatrchyan et al., *Observation of a new boson at a mass of 125 GeV with the CMS experiment at the LHC*, Phys.Lett. **B716** (2012) 30–61, arXiv:1207.7235 [hep-ex].
- [5] M. Li, X.-D. Li, S. Wang, and Y. Wang, *Dark Energy: a Brief Review*, arXiv:1209.0922 [astro-ph.CO].
- [6] K. Garrett and G. Duda, *Dark Matter: A Primer*, Adv.Astron. **2011** (2011) 968283, arXiv:1006.2483 [hep-ph].
- [7] M. D. J. Taylor, C. Zaafiratos, *Modern Physics for Scientists and Engineers*, 2004. ISBN 0-13-805715-X.
- [8] J. D. Jackson, *Classical Electrodynamics*, 1999. ISBN 0-471-30932-X.

- [9] D. S. M. Peskin, *An Introduction to Quantum Field Theory*, 1995. ISBN 978-0-201-50397-5.
- [10] S. Weinberg, *A Model of Leptons*, Phys. Rev. Lett. **19** (Nov, 1967) 1264–1266.
<http://link.aps.org/doi/10.1103/PhysRevLett.19.1264>.
- [11] J. Goldstone, A. Salam, and S. Weinberg, *Broken Symmetries*, Phys. Rev. **127** (Aug, 1962) 965–970. <http://link.aps.org/doi/10.1103/PhysRev.127.965>.
- [12] S. Glashow, J. Iliopoulos, and L. Maiani, *Weak Interactions with Lepton-Hadron Symmetry*, Phys.Rev. **D2** (1970) 1285–1292.
- [13] A. Masiero, S. Vempati, and O. Vives, *Flavour physics and grand unification*, arXiv:0711.2903 [hep-ph].
- [14] G. Esposito, *An Introduction to quantum gravity*, arXiv:1108.3269 [hep-th].
- [15] J. Polchinski, *What is string theory?*, arXiv:hep-th/9411028 [hep-th].
- [16] K. Huang, *Statistical Mechanics*, 1987. ISBN 0-471-81518-7.
- [17] V. I. Yukalov, *Basics of Bose-Einstein condensation*, Physics of Particles and Nuclei **42** (May, 2011) 460–513, arXiv:1105.4992 [cond-mat.stat-mech].
- [18] S. Weinberg, *The Quantum Theory of Fields, Volume 1: Foundations*, 2008. ISBN 978-0-521-67053-1.
- [19] S. Petcov, *The Solar neutrino problem and solar neutrino oscillations in vacuum and in matter*, Lect.Notes Phys. **512** (1998) 281–328, arXiv:hep-ph/9806466 [hep-ph].

- [20] T. Schwetz, M. Tortola, and J. W. Valle, *Three-flavour neutrino oscillation update*, New J.Phys. **10** (2008) 113011, [arXiv:0808.2016](#) [hep-ph].
- [21] A. M. F. Halzen, *Quarks and Leptons: An Introductory Course in Modern Particle Physics*, 1984. ISBN 0-471-88741-2.
- [22] J. Beringer et al., *Particle data group*, Phys. Rev. **D86** (2012) .
- [23] ATLAS Collaboration, G. Aad et al., *Measurement of the cross-section for b^- jets produced in association with a Z boson at $\sqrt{s} = 7$ TeV with the ATLAS detector*, Phys.Lett. **B706** (2012) 295–313, [arXiv:1109.1403](#) [hep-ex].
- [24] H. Georgi, L. Kaplan, D. Morin, and A. Schenk, *Effects of top quark compositeness*, Phys. Rev. D **51** (1995) 3888–3894.
- [25] A. Pomarol and J. Serra, *Top quark compositeness: Feasibility and implications*, Phys. Rev. D **78** (2008) 074026.
- [26] B. Lillie, J. Shu, and T. M. Tait, *Top compositeness at the Tevatron and LHC*, JHEP **0804** 087.
- [27] K. Kumar, T. M. Tait, and R. Vega-Morales, *Manifestations of top compositeness at colliders*, JHEP **0905** 022.
- [28] M. Guchait, F. Mahmoudi, and K. Sridhar, *Associated production of a Kaluza-Klein excitation of a gluon with a t anti- t pair at the LHC*, Phys. Lett. **B666** (2008) 347–351.

- [29] C. Degrande, J.-M. Gerard, C. Grojean, F. Maltoni, and G. Servant, *Non-resonant New Physics in Top Pair Production at Hadron Colliders*, JHEP **1103** (2011) 125.
- [30] *The ATLAS Experiment at the CERN Large Hadron Collider*, Journal of Instrumentation **3** (2008) no. 08, S08003.
<http://stacks.iop.org/1748-0221/3/i=08/a=S08003>.
- [31] *The CMS electromagnetic calorimeter project: Technical Design Report*. Technical Design Report CMS. CERN, Geneva, 1997.
- [32] M. L. Mangano et al., *ALPGEN, a generator for hard multiparton processes in hadronic collisions*, JHEP **0307** (2003) 001.
- [33] G. Corcella et al., *HERWIG 6: An Event generator for hadron emission reactions with interfering gluons (including supersymmetric processes)*, JHEP **0101** (2001) 010.
- [34] J. M. Butterworth, J. R. Forshaw, and M. H. Seymour, *Multiparton interactions in photoproduction at HERA*, Z. Phys. **C72** (1996) 637–646.
- [35] J. Alwall, S. Hoche, F. Krauss, N. Lavesson, L. Lonnblad, et al., *Comparative study of various algorithms for the merging of parton showers and matrix elements in hadronic collisions*, Eur.Phys.J. **C53** (2008) 473–500, [arXiv:0706.2569](https://arxiv.org/abs/0706.2569) [hep-ph].
- [36] F. Maltoni and T. Stelzer, *MadEvent: Automatic event generation with MadGraph*, JHEP **0302** (2003) 027.

- [37] The ATLAS Collaboration, *Electron performance measurements with the ATLAS detector using the 2010 LHC proton-proton collision data*, Eur. Phys. J. C **72** (Oct, 2011) 1909. 45 p. Submitted to Eur. Phys. J. C.
- [38] L. Cerrito, B. Cooper, A. J. Poll, V. Boisvert, T. Fonseca, R. Goncalo, and M. Rose, *Study of electron isolation in $Z \rightarrow ee$ and $t\bar{t}$ decays*, . ATL-COM-PHYS-2009-605.
- [39] *Determination of the muon reconstruction efficiency in ATLAS at the Z resonance in proton-proton collisions at $\sqrt{s}=7$ TeV*, Tech. Rep. ATLAS-CONF-2011-008, CERN, Geneva, Feb, 2011.
- [40] Matteo Cacciari and Gavin P. Salam and Gregory Soyez, *The anti- k jet clustering algorithm*, Journal of High Energy Physics **2008** (2008) no. 04, 063.
<http://stacks.iop.org/1126-6708/2008/i=04/a=063>.
- [41] *Commissioning of the ATLAS high-performance b-tagging algorithms in the 7 TeV collision data*, Tech. Rep. ATLAS-CONF-2011-102, CERN, Geneva, Jul, 2011.
- [42] *Selection of jets produced in proton-proton collisions with the ATLAS detector using 2011 data*, Tech. Rep. ATLAS-CONF-2012-020, CERN, Geneva, Mar, 2012.
- [43] W. Verkerke, D. Kirkby , *RooFit Users Manual v2.91*, .
http://root.cern.ch/download/doc/RooFit_Users_Manual_2.91-33.pdf.
- [44] *Measurement of the $t\bar{t}$ production cross-section in pp collisions at $\sqrt{s} = 7$ TeV using kinematic information of lepton+jets events*, Tech. Rep. ATLAS-CONF-2011-121, CERN, Geneva, Aug, 2011.

- [45] N. Benekos *et al.*, *Lepton Trigger and Identification for the first Top quark observation*, . ATL-COM-PHYS-2010-826.
- [46] N. Benekos *et al.*, *Lepton trigger and identification for the Winter 2011 top quark analyses*, . ATL-COM-PHYS-2011-123.
- [47] T. Sjöstrand, S. Mrenna, and P. Skands, *PYTHIA 6.4 physics and manual*, JHEP **05** (2006) 026.
- [48] ATLAS Collaboration, *Close-by Jet Effects on Jet Energy Scale Calibration in pp Collisions at $\sqrt{s} = 7$ TeV with the ATLAS Detector*, Tech. Rep. ATLAS-CONF-2011-062, CERN, Geneva, April, 2011. <https://atlas.web.cern.ch/Atlas/GROUPS/PHYSICS/CONFNOTES/ATLAS-CONF-2011-062/>.
- [49] *Light-quark and Gluon Jets in ATLAS*, Tech. Rep. ATLAS-CONF-2011-053, CERN, Geneva, Apr, 2011. <http://cdsweb.cern.ch/record/1342550/>.
- [50] G. Romeo, A. Schwartzman, R. Piegaiia, T. Carli, and R. Teuscher, *Jet Energy Resolution from In-situ Techniques with the ATLAS Detector Using Proton-Proton Collisions at a Center of Mass Energy $\sqrt{s} = 7$ TeV*, Tech. Rep. ATL-COM-PHYS-2011-240, CERN, Geneva, Mar, 2011.
- [51] D. W. Miller, A. Schwartzman, and D. Su, *Pile-up jet energy scale corrections using the jet-vertex fraction method*, Tech. Rep. ATL-COM-PHYS-2009-180, CERN, Geneva, Apr, 2009.
- [52] D. Stump *et al.*, *Inclusive jet production, parton distributions, and the search for new physics*, JHEP **0310** (2003) 046.

- [53] S. Alioli, P. Nason, C. Oleari, and E. Re, *A general framework for implementing NLO calculations in shower Monte Carlo programs: the POWHEG BOX*, JHEP **1006** (2010) 043.
- [54] B. P. Kersevan and E. Richter-Was, *The Monte Carlo event generator AcerMC version 2.0 with interfaces to PYTHIA 6.2 and HERWIG 6.5*, arXiv:hep-ph/0405247.
- [55] P. Z. Skands, *Tuning Monte Carlo Generators: The Perugia Tunes*, Phys. Rev. **D82** (2010) 074018.
- [56] S. Frixione and B. R. Webber, *Matching NLO QCD computations and parton shower simulations*, JHEP **06** (2002) 029.
- [57] G. Aad et al., *Measurement of the cross-section for W boson production in association with b-jets in pp collisions at $\sqrt{s} = 7$ TeV with the ATLAS detector*, Tech. Rep. arXiv:1302.2929. CERN-PH-EP-2012-357, CERN, Geneva, Feb, 2013. Submitted to JHEP.
- [58] *First Measurement of the cross section ratio $t\bar{t}b\bar{b}/t\bar{t}j\bar{j}$ in pp collisions at $\sqrt{s} = 7$ TeV*, Tech. Rep. CMS-PAS-TOP-12-024, CERN, Geneva, July, 2012.

Appendix

A Data and Monte Carlo samples

In this section, we present details of the Monte Carlo and data samples used in the analysis. Monte Carlo samples are described primarily by the process they model (e.g. $Z \rightarrow ee + \text{jets}$). The effective cross-section for each sample is given, along with the ATLAS-specific run number. For the data, we use the ATLAS-standard labels which break the data up into run periods. Typically, detector and beam conditions vary only slightly within a given period, while the variation between periods can potentially be large. The start and end dates of each period are given, along with the total integrated luminosity and the peak number of interactions per bunch crossing ($\langle \mu \rangle$).

A.1 Data

The data used in this analysis were collected by ATLAS during the 2011 run. During this run, the center of mass energy for the colliding proton beams was 7 TeV, and bunches in the beam were separated in time by 50 ns. The instantaneous luminosity, however, changed a great deal over the course of the run: from approximately $1 \times 10^{30} \text{ cm}^{-2} \text{ s}^{-1}$ at the beginning to $4 \times 10^{33} \text{ cm}^{-2} \text{ s}^{-1}$ at the end. By convention, ATLAS groups its runs into periods, with runs in a given period having more or less similar run conditions. The duration, total integrated luminosity, and peak number of interactions per bunch crossing for each run period are given in Table 22. The total luminosity reported in this table reflects the total amount of data collected by ATLAS during this time, not the amount of data which passed the GRL used

in this analysis. After the application of the GRL, the usable data set corresponded to an integrated luminosity of 4.7 fb^{-1} .

Data period	Run duration	Total integrated luminosity (pb^{-1})	Peak $\langle \mu \rangle$
Period B	March 21 - 24	17.0	8.5
Period D	April 14 - 29	178.8	7.3
Period E	April 30 - May 3	50.2	7.6
Period F	May 15 - 25	152.2	8.1
Period G	May 27 - June 14	560.8	8.0
Period H	June 16 - 28	278.3	6.9
Period I	July 13 - 29	399.2	9.1
Period J	July 30 - August 4	232.9	9.8
Period K	August 4 - 22	660.2	11.3
Period L	September 7 - October 5	1568.8	15.8
Period M	October 6 - October 30	1121.8	32.1

Table 22: Details of each data-taking period from the 2011 run. The start and end dates for each period, the total integrated luminosity recorded by ATLAS during the period, and the peak number of interactions per bunch-crossing are given. The total recorded luminosity does not take into the GRL used in this analysis, so the amount of data used from each period will be slightly different.

A.2 Monte Carlo

A number of Monte Carlo samples were used in the this analysis to model various physical processes, as described in detail in Chapter 4. Here, we present the sample name, generator, and total cross-section for each sample. An ATLAS-specific dataset ID number is also given for reference. Samples used to model the $t\bar{t}$ decay are given in Table 23, while samples used to model other SM backgrounds are given in Tables 26 - 30. Additional $t\bar{t}$ samples used to study systematic uncertainties are listed in Tables 24 and 25. For an explanation of how these samples were used and which systematic uncertainties were evaluated, see Chapter 7.

Sample name	Generator	Dataset ID	Cross-section (pb)
$t\bar{t} + b\bar{b}$	ALPGEN	116108	1.43
$t\bar{t} + c\bar{c}$	ALPGEN	116109	2.98
$t\bar{t}$ dilepton + 0 partons	ALPGEN	105980	5.84
$t\bar{t}$ dilepton + 1 partons	ALPGEN	105981	5.75
$t\bar{t}$ dilepton + 2 partons	ALPGEN	105982	3.53
$t\bar{t}$ dilepton + 3 partons	ALPGEN	117897	1.59
$t\bar{t}$ dilepton + 4 partons	ALPGEN	117898	0.56
$t\bar{t}$ dilepton + 5 partons	ALPGEN	117899	0.22
$t\bar{t}$ semi-leptonic + 0 partons	ALPGEN	105970	24.31
$t\bar{t}$ semi-leptonic + 1 partons	ALPGEN	105971	23.96
$t\bar{t}$ semi-leptonic + 2 partons	ALPGEN	105972	14.86
$t\bar{t}$ semi-leptonic + 3 partons	ALPGEN	117887	6.63
$t\bar{t}$ semi-leptonic + 4 partons	ALPGEN	117888	2.35
$t\bar{t}$ semi-leptonic + 5 partons	ALPGEN	117889	0.88
$t\bar{t} + W$	MADGRAPH + PYTHIA	119353	0.12444
$t\bar{t} + Wj$	MADGRAPH + PYTHIA	119354	0.083471
$t\bar{t} + Z$	MADGRAPH + PYTHIA	119355	0.095579
$t\bar{t} + Zj$	MADGRAPH + PYTHIA	119356	0.081596
$t\bar{t} + H$ ($t\bar{t} \rightarrow l\bar{l}$, $H \rightarrow b\bar{b}$)	MADGRAPH + PYTHIA	146477	0.0499

Table 23: $t\bar{t}$ MC samples used in the analysis.

Sample name	Generator	Dataset ID	Cross-section (pb)
$t\bar{t}$, non-all-hadronic	MC@NLO	105200	90.545
$t\bar{t}$, non-all-hadronic	POWHEG + PYTHIA	105861	90.55
$t\bar{t}$, non-all-hadronic	POWHEG + HERWIG	105860	90.56
$t\bar{t} \rightarrow l\bar{l} + 0$ parton	ALPGEN + PYTHIA	117113	5.823
$t\bar{t} \rightarrow l\bar{l} + 1$ parton	ALPGEN + PYTHIA	117114	5.640
$t\bar{t} \rightarrow l\bar{l} + 2$ parton	ALPGEN + PYTHIA	117115	3.583
$t\bar{t} \rightarrow l\bar{l} + 3$ parton	ALPGEN + PYTHIA	117116	1.629
$t\bar{t} \rightarrow l\bar{l} + 4$ parton	ALPGEN + PYTHIA	117117	0.590
$t\bar{t} \rightarrow l\bar{l} + 5$ parton	ALPGEN + PYTHIA	117118	0.244
$t\bar{t} \rightarrow lq + 0$ parton	ALPGEN + PYTHIA	117083	24.308
$t\bar{t} \rightarrow lq + 1$ parton	ALPGEN + PYTHIA	117084	23.565
$t\bar{t} \rightarrow lq + 2$ parton	ALPGEN + PYTHIA	117085	14.882
$t\bar{t} \rightarrow lq + 3$ parton	ALPGEN + PYTHIA	117086	6.772
$t\bar{t} \rightarrow lq + 4$ parton	ALPGEN + PYTHIA	117087	2.441
$t\bar{t} \rightarrow lq + 5$ parton	ALPGEN + PYTHIA	117088	1.083

Table 24: $t\bar{t}$ Monte Carlo samples used to evaluate generator & showering systematics.

Sample name	Generator	Dataset ID	Cross-section (pb)
$t\bar{t} \rightarrow ll + 0$ parton	ALPGEN + PYTHIA, kt fac = 2.0	117133	5.823
$t\bar{t} \rightarrow ll + 1$ parton	ALPGEN + PYTHIA, kt fac = 2.0	117134	5.640
$t\bar{t} \rightarrow ll + 2$ parton	ALPGEN + PYTHIA, kt fac = 2.0	117135	3.583
$t\bar{t} \rightarrow ll + 3$ parton	ALPGEN + PYTHIA, kt fac = 2.0	117136	1.629
$t\bar{t} \rightarrow ll + 4$ parton	ALPGEN + PYTHIA, kt fac = 2.0	117137	0.590
$t\bar{t} \rightarrow lq + 0$ parton	ALPGEN + PYTHIA, kt fac = 2.0	117183	24.308
$t\bar{t} \rightarrow lq + 1$ parton	ALPGEN + PYTHIA, kt fac = 2.0	117184	23.565
$t\bar{t} \rightarrow lq + 2$ parton	ALPGEN + PYTHIA, kt fac = 2.0	117185	14.882
$t\bar{t} \rightarrow lq + 3$ parton	ALPGEN + PYTHIA, kt fac = 2.0	117186	6.772
$t\bar{t} \rightarrow lq + 4$ parton	ALPGEN + PYTHIA, kt fac = 2.0	117187	2.441
$t\bar{t} \rightarrow ll + 0$ parton	ALPGEN + PYTHIA, kt fac = 0.5	117123	5.823
$t\bar{t} \rightarrow ll + 1$ parton	ALPGEN + PYTHIA, kt fac = 0.5	117124	5.640
$t\bar{t} \rightarrow ll + 2$ parton	ALPGEN + PYTHIA, kt fac = 0.5	117125	3.583
$t\bar{t} \rightarrow ll + 3$ parton	ALPGEN + PYTHIA, kt fac = 0.5	117126	1.629
$t\bar{t} \rightarrow ll + 4$ parton	ALPGEN + PYTHIA, kt fac = 0.5	117127	0.590
$t\bar{t} \rightarrow lq + 0$ parton	ALPGEN + PYTHIA, kt fac = 0.5	117093	24.308
$t\bar{t} \rightarrow lq + 1$ parton	ALPGEN + PYTHIA, kt fac = 0.5	117094	23.565
$t\bar{t} \rightarrow lq + 2$ parton	ALPGEN + PYTHIA, kt fac = 0.5	117095	14.882
$t\bar{t} \rightarrow lq + 3$ parton	ALPGEN + PYTHIA, kt fac = 0.5	117096	6.772
$t\bar{t} \rightarrow lq + 4$ parton	ALPGEN + PYTHIA, kt fac = 0.5	117097	2.441
$t\bar{t} + \text{More PS (non-all-hadronic)}$	ACERMC	117209	90.59
$t\bar{t} + \text{Less PS (non-all-hadronic)}$	ACERMC	117210	90.59

Table 25: $t\bar{t}$ Monte Carlo samples used to evaluate ISR / FSR systematics.

Sample name	Generator	Dataset ID	Cross-section (pb)
$W \rightarrow e \nu + 0$ parton	ALPGEN	107680	8305.2
$W \rightarrow e \nu + 1$ parton	ALPGEN	107681	1565.12
$W \rightarrow e \nu + 2$ parton	ALPGEN	107682	453.948
$W \rightarrow e \nu + 3$ parton	ALPGEN	107683	121.716
$W \rightarrow e \nu + 4$ parton	ALPGEN	107684	31.044
$W \rightarrow e \nu + 5$ parton	ALPGEN	107685	8.4
$W \rightarrow \mu \nu + 0$ parton	ALPGEN	107690	8303.52
$W \rightarrow \mu \nu + 1$ parton	ALPGEN	107691	1565.05
$W \rightarrow \mu \nu + 2$ parton	ALPGEN	107692	453.396
$W \rightarrow \mu \nu + 3$ parton	ALPGEN	107693	122.256
$W \rightarrow \mu \nu + 4$ parton	ALPGEN	107694	30.9
$W \rightarrow \mu \nu + 5$ parton	ALPGEN	107695	8.304
$W \rightarrow \tau \nu + 0$ parton	ALPGEN	107700	8302.32
$W \rightarrow \tau \nu + 1$ parton	ALPGEN	107701	1563.84
$W \rightarrow \tau \nu + 2$ parton	ALPGEN	107702	453.816
$W \rightarrow \tau \nu + 3$ parton	ALPGEN	107703	121.812
$W \rightarrow \tau \nu + 4$ parton	ALPGEN	107704	30.678
$W \rightarrow \tau \nu + 5$ parton	ALPGEN	107705	8.304
$Wb\bar{b} + 0$ parton	ALPGEN	106280	3.3072
$Wb\bar{b} + 1$ parton	ALPGEN	106281	2.6756
$Wb\bar{b} + 2$ parton	ALPGEN	106282	1.3673
$Wb\bar{b} + 3$ parton	ALPGEN	106283	0.6569

Table 26: W +jets MC samples used in the analysis.

Sample name	Generator	Dataset ID	Cross-section (pb)
$Z \rightarrow ee + 0$ parton	ALPGEN	107650	835.4
$Z \rightarrow ee + 1$ parton	ALPGEN	107651	167.675
$Z \rightarrow ee + 2$ parton	ALPGEN	107652	50.4125
$Z \rightarrow ee + 3$ parton	ALPGEN	107653	13.9875
$Z \rightarrow ee + 4$ parton	ALPGEN	107654	3.6
$Z \rightarrow ee + 5$ parton	ALPGEN	107655	1.0375
$Z \rightarrow \mu\mu + 0$ parton	ALPGEN	107660	835.85
$Z \rightarrow \mu\mu + 1$ parton	ALPGEN	107661	167.675
$Z \rightarrow \mu\mu + 2$ parton	ALPGEN	107662	50.4125
$Z \rightarrow \mu\mu + 3$ parton	ALPGEN	107663	13.9875
$Z \rightarrow \mu\mu + 4$ parton	ALPGEN	107664	3.4375
$Z \rightarrow \mu\mu + 5$ parton	ALPGEN	107665	0.9625
$Z \rightarrow \tau\tau + 0$ parton	ALPGEN	107670	835.5
$Z \rightarrow \tau\tau + 1$ parton	ALPGEN	107671	168.512
$Z \rightarrow \tau\tau + 2$ parton	ALPGEN	107672	50.45
$Z \rightarrow \tau\tau + 3$ parton	ALPGEN	107673	14.0625
$Z \rightarrow \tau\tau + 4$ parton	ALPGEN	107674	3.4875
$Z \rightarrow \tau\tau + 5$ parton	ALPGEN	107675	0.9625

Table 27: Z +jets MC samples used in the analysis.

Sample name	Generator	Dataset ID	Cross-section (pb)
$Z \rightarrow ee + b\bar{b} + 0$ parton	ALPGEN	109300	6.31
$Z \rightarrow ee + b\bar{b} + 1$ parton	ALPGEN	109301	2.44
$Z \rightarrow ee + b\bar{b} + 2$ parton	ALPGEN	109302	0.845
$Z \rightarrow ee + b\bar{b} + 3$ parton	ALPGEN	109303	0.381
$Z \rightarrow \mu\mu + b\bar{b} + 0$ parton	ALPGEN	109305	6.34
$Z \rightarrow \mu\mu + b\bar{b} + 1$ parton	ALPGEN	109306	2.45
$Z \rightarrow \mu\mu + b\bar{b} + 2$ parton	ALPGEN	109307	0.845
$Z \rightarrow \mu\mu + b\bar{b} + 3$ parton	ALPGEN	109308	0.378
$Z \rightarrow \tau\tau + b\bar{b} + 0$ parton	ALPGEN	109310	6.37
$Z \rightarrow \tau\tau + b\bar{b} + 1$ parton	ALPGEN	109311	2.42
$Z \rightarrow \tau\tau + b\bar{b} + 2$ parton	ALPGEN	109312	0.865
$Z \rightarrow \tau\tau + b\bar{b} + 3$ parton	ALPGEN	109313	0.381

Table 28: $Z+b\bar{b}$ MC samples used in the analysis.

Sample name	Generator	Dataset ID	Cross-section (pb)
$Z \rightarrow ee + 0$ parton, Mll 10-40	ALPGEN	116260	3819
$Z \rightarrow ee + 1$ parton, Mll 10-40	ALPGEN	116251	106.15
$Z \rightarrow ee + 2$ parton, Mll 10-40	ALPGEN	116252	51.75
$Z \rightarrow ee + 3$ parton, Mll 10-40	ALPGEN	116253	10.475
$Z \rightarrow ee + 4$ parton, Mll 10-40	ALPGEN	116254	2.3125
$Z \rightarrow ee + 5$ parton, Mll 10-40	ALPGEN	116255	0.575
$Z \rightarrow \mu\mu + 0$ parton, Mll 10-40	ALPGEN	116260	3818.625
$Z \rightarrow \mu\mu + 1$ parton, Mll 10-40	ALPGEN	116261	106.0875
$Z \rightarrow \mu\mu + 2$ parton, Mll 10-40	ALPGEN	116262	51.8125
$Z \rightarrow \mu\mu + 3$ parton, Mll 10-40	ALPGEN	116263	10.475
$Z \rightarrow \mu\mu + 4$ parton, Mll 10-40	ALPGEN	116264	2.3125
$Z \rightarrow \mu\mu + 5$ parton, Mll 10-40	ALPGEN	116265	0.575
$Z \rightarrow \tau\tau + 0$ parton, Mll 10-40	ALPGEN	116270	3818.875
$Z \rightarrow \tau\tau + 1$ parton, Mll 10-40	ALPGEN	116271	106.1625
$Z \rightarrow \tau\tau + 2$ parton, Mll 10-40	ALPGEN	116272	51.83755
$Z \rightarrow \tau\tau + 3$ parton, Mll 10-40	ALPGEN	116273	10.45
$Z \rightarrow \tau\tau + 4$ parton, Mll 10-40	ALPGEN	116274	2.3125
$Z \rightarrow \tau\tau + 5$ parton, Mll 10-40	ALPGEN	116275	0.575

Table 29: Low mass Z +jets MC samples used in the analysis.

Sample name	Generator	Dataset ID	Cross-section (pb)
Single top, tchan ($e\nu$)	AcerMC	117360	7.12
Single top, tchan ($\mu\nu$)	AcerMC	117361	7.12
Single top, tchan ($\tau\nu$)	AcerMC	117362	7.12
Single top, schan ($e\nu$)	MC@NLO	108343	0.47
Single top, schan ($\mu\nu$)	MC@NLO	108344	0.47
Single top, schan ($\tau\nu$)	MC@NLO	108345	0.47
Single top, Wt	MC@NLO	108346	14.59
$WW \rightarrow ll + 0$ partons	ALPGEN	107100	2.6397
$WW \rightarrow ll + 1$ partons	ALPGEN	107101	1.25521
$WW \rightarrow ll + 2$ partons	ALPGEN	107102	0.572922
$WW \rightarrow ll + 3$ partons	ALPGEN	107103	0.221508
$WZ \rightarrow ll + 0$ partons	ALPGEN	107104	0.859904
$WZ \rightarrow ll + 1$ partons	ALPGEN	107105	0.529664
$WZ \rightarrow ll + 2$ partons	ALPGEN	107106	0.287872
$WZ \rightarrow ll + 3$ partons	ALPGEN	107107	0.1216
$ZZ \rightarrow ll + 0$ partons	ALPGEN	107108	0.66118
$ZZ \rightarrow ll + 1$ partons	ALPGEN	107109	0.30446
$ZZ \rightarrow ll + 2$ partons	ALPGEN	107110	0.11518
$ZZ \rightarrow ll + 3$ partons	ALPGEN	107111	0.04082

Table 30: Single top & diboson MC samples used in the analysis.